

Charge symmetry breaking in $\vec{n}\text{-}\vec{p}$ scattering at 183 MeV

S. E. Vigdor,^(1,2) W. W. Jacobs,⁽¹⁾ L. D. Knutson,⁽³⁾ J. Sowinski,⁽¹⁾ C. Bloch,⁽¹⁾ P. L. Jolivet,⁽⁴⁾
S. W. Wissink,⁽¹⁾ R. C. Byrd,⁽⁵⁾ and C. Whiddon⁽¹⁾

⁽¹⁾Indiana University Cyclotron Facility and Department of Physics, Bloomington, Indiana 47405

⁽²⁾Laboratoire National Saturne, 91191 Gif-sur-Yvette, France

⁽³⁾Department of Physics, University of Wisconsin, Madison, Wisconsin 53706

⁽⁴⁾Department of Physics, Hope College, Holland, Michigan 49423

⁽⁵⁾P-2 Division, Los Alamos National Laboratory, Los Alamos, New Mexico 87545

(Received 31 January 1992)

We report the results of a precise test of charge symmetry in the scattering of polarized neutrons from polarized protons at a laboratory bombarding energy of 183 MeV. The observable sensitive to charge symmetry is the difference between the analyzing powers associated with the neutron spin [$A_n(\theta)$] and with the proton spin [$A_p(\theta)$]. Systematic errors and experimental ambiguities in the measurement of this difference are extensively discussed. Our result for $\Delta A \equiv A_n - A_p$, averaged over the angular range $82.2^\circ \leq \theta_{c.m.} \leq 116.1^\circ$, is $(33.1 \pm 5.9 \pm 4.3) \times 10^{-4}$. With the statistical and systematic errors added in quadrature, this value is 3.4 standard deviations larger than the effect expected from pure photon exchange (the electromagnetic spin-orbit interaction) between the neutron and proton, and thus represents clear evidence of charge symmetry breaking in the strong interaction. We also extract information about the angular dependence of $\Delta A(\theta)$, within limitations imposed by uncertainties in the measured beam and target polarizations. Both the angle-averaged value and the angular dependence measured for ΔA are in excellent agreement with predictions from meson-exchange theory, when these include both the effect of the n - p mass difference on one-pion exchange and the isospin mixing of ρ^0 and ω^0 mesons. In particular, the Bonn nucleon-nucleon (NN) potential model accounts for the present results utilizing ρNN and ωNN coupling constant values deduced previously for this potential from fits to more conventional NN scattering data.

PACS number(s): 13.75.Cs, 21.30.+y, 11.30.Hv, 24.70.+s

I. INTRODUCTION

In this paper we present the results of an experiment that addresses one of the most basic and longstanding questions in nuclear physics: Does the strong interaction exactly preserve isospin symmetry? From the contemporary theoretical viewpoint, some isospin violation is to be expected, even though the underlying color force among quarks is assumed in quantum chromodynamics (QCD) to be independent of the quark flavor, and hence of isospin. The expected violation arises through mass-dependent terms that must be added to the QCD Lagrangian to take into account the nonzero masses of the quarks [1]. The spontaneous-symmetry-breaking mechanism that generates the quark masses appears, in particular, to have resulted in *different* masses for the u and d quarks. The ratio of their "current" masses inferred [2] from quark-model fits to hadron mass splittings and decay rates is $m_u/m_d \simeq 1/2$, suggesting a sizable isospin [SU(2)] symmetry violation at the quark level. In quark-model calculations [1,2] this mass difference ($\Delta m_{ud} \sim$ a few MeV) is predominantly responsible [2] (with smaller contributions from photon exchange among quarks) for the observed n - p mass difference and the observed [3,4] mixing of ρ^0 and ω^0 mesons. These effects should also produce small (because Δm_{ud} is small compared to the nucleon mass) isospin-violating nuclear forces, for which we have searched in our experiment.

In discussing the implications of isospin symmetry for nuclear systems, it is traditional to distinguish between the strong form ("charge independence") and the more restricted form ("charge symmetry"). Charge independence refers to invariance under *arbitrary* rotations in isospin space. There is clear evidence for its violation in the 1S_0 scattering lengths deduced from low-energy nucleon-nucleon (NN) scattering [2]:

$$\frac{1}{2}(a_{pp}^{\text{corr}} + a_{nn}^{\text{corr}}) - a_{np} \simeq 5.7 \pm 0.3 \text{ fm} ,$$

where the pp and nn values have been corrected for electromagnetic contributions to the scattering and for purely kinematic effects of the n - p mass difference. Furthermore, this violation is understood quantitatively [5] to arise primarily from the influence on one- and two-pion exchange of the mass difference (Δm_π) between the neutral and charged pions. The effects of Δm_π presumably originate in the electromagnetic interaction among quarks; they cannot be attributed to Δm_{ud} , because u (\bar{u}) and d (\bar{d}) appear with equal probability in quark-model wave functions for *each* of the three pions.

In order to probe isospin violations beyond those associated with Δm_π , one can test the more limited implications of *charge symmetry*: invariance under 180° rotations (about the "2" axis) in isospin space that interchange particles with their isospin mirror particles (e.g., $n \leftrightarrow p$, $u \leftrightarrow d$, $\pi^+ \leftrightarrow \pi^-$). Most tests of charge symmetry (CS) have compared mirror systems with total isospin

component $T_3 \neq 0$. Among such tests, the ones most widely accepted [2] as suggesting charge symmetry breaking (CSB) in the strong interaction involve comparison of the nn and pp scattering lengths, and of the binding energies of mirror nuclei (the so-called Nolen-Schiffer anomaly [6]), especially of ${}^3\text{H}$ vs ${}^3\text{He}$. In these cases, however, $\approx 90\%$ of the raw differences observed between mirror systems can be attributed to purely electromagnetic interactions between nucleons. The residual inferred strong-interaction CSB is thus a hostage to any small inaccuracies in the theoretical subtraction of the dominant electromagnetic “background.” In the case of the scattering lengths, there is an additional ambiguity associated with extracting the nn parameter from final-state interaction studies in different systems [2,7].

The experiment presented here belongs to a different class of CS tests, namely, ones that examine *self-conjugate* ($T_3=0$) systems. Such systems represent eigenstates of the CS operator, with eigenvalue $+1$ or -1 according to whether the total isospin of the system is even or odd [8]. CS prohibits mixing of the even and odd eigenstates, e.g., of $T=0$ and $T=1$ states of the n - p system, even though charge *independence* is violated. This presents the opportunity to test CS in the n - p system, where the Coulomb force between nucleons is absent and the electromagnetic “background” is thus much reduced with respect to expected strong-interaction “signals.”

Isospin-mixing in the n - p system, if it is caused by forces that conserve angular momentum and parity, can occur only between certain pairs of angular momentum states: 1P_1 - 3P_1 , 3D_2 - 1D_2 , 1F_3 - 3F_3 , etc. The form of potentials that can cause such mixing (changing the channel spin as well as the isospin), while obeying other symmetry principles, is quite restricted. They can have angular momentum and isospin dependence of one of the two following types [8]:

$$V_a^{\text{CSB}} = V_a(r)[\tau_3(1) - \tau_3(2)][\sigma(1) - \sigma(2)] \cdot \mathbf{L}, \quad (1)$$

$$V_b^{\text{CSB}} = V_b(r)[\tau(1) \times \tau(2)]_3[\sigma(1) \times \sigma(2)] \cdot \mathbf{L}, \quad (2)$$

where τ represents the isospin vector and σ the Pauli spin matrices for the individual nucleons (labeled 1 and 2), and \mathbf{L} is their relative orbital angular momentum. For example, the spin-orbit interaction between the neutron magnetic moment and the proton current can be written in the form of V_a^{CSB} , and represents the dominant *electromagnetic* source of n - p isospin mixing. Our experiment represents a search for strong-interaction potentials of the above types, which have been classified by Henley and Miller [8] as class IV NN interactions. Class IV interactions vanish for the nn and pp systems, which are sensitive rather to class III CSB potentials, with isospin dependence of the form $[\tau_3(1) + \tau_3(2)]$. In this sense, the present experiment complements searches for nn vs pp scattering length differences.

Isospin mixing would be manifested in n - p scattering by different sensitivities of the scattering amplitude to neutron and to proton spin projections. The particular CS implication we have tested is illustrated schematically in Fig. 1. The diagram on the left represents (in the c.m. frame) an experiment in which polarized neutrons are

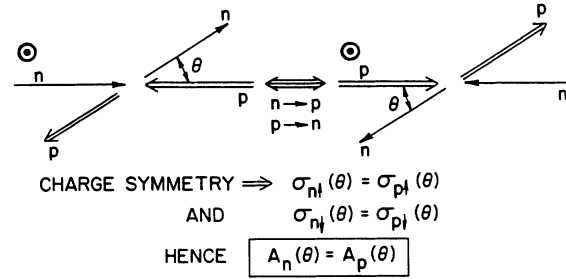


FIG. 1. Schematic illustration of the implication of charge symmetry for the analyzing power observables in n - p elastic scattering. The scattering diagram on the left is transformed into the one on the right solely by the action of the charge symmetry operator.

scattered toward the left at angle θ from unpolarized protons. The CS operator (which acts only on the isospin, and not at all on the spatial or spin state of the system) transforms this process into the right-hand diagram, representing an analogous scattering experiment, but this time with unpolarized neutrons incident on polarized protons. The equivalence of these two diagrams if CS is preserved implies the equality of the neutron and proton analyzing powers:

$$\text{CS} \Rightarrow \Delta A(\theta) \equiv A_n(\theta) - A_p(\theta) = 0 \quad \text{for all } \theta. \quad (3)$$

We present here the results of a measurement of $\Delta A(\theta)$ for n - p scattering at a bombarding energy $E_n = 183$ MeV. Previous reports of this work have appeared in Refs. [9] and [10].

One other measurement of ΔA , performed at $E_n = 477$ MeV, has been published previously [11]. The present work complements and extends that of Ref. [11] in several important ways. First, it represents an independent experiment, carried out with numerous differences in technique, which has achieved considerably better statistical and systematic precision. Second, the bombarding energy difference is significant: at 183 MeV, we attain (for reasons to be explained later) much greater sensitivity to the interesting CSB contribution from the Δm_{ud} -induced mixing of ρ^0 and ω^0 mesons. Finally, whereas Ref. [11] presented a measurement of ΔA at a single angle, we report results on its angular dependence as well, allowing a more complete test of theoretical predictions.

The remainder of this paper is organized as follows. In Sec. II we discuss the basic principles and the most important features of our measurement. We describe the technical details of the experimental apparatus in Sec. III, with emphasis on features relevant to our discussion of systematic errors later in the paper. Data analysis procedures used to isolate free n - p scattering events and to extract various polarization observables for them are presented in Sec. IV. Results for ΔA and for several related quantities are reported in Sec. V and systematic errors in the results are assessed in Sec. VI. Comparison to theoretical predictions of CSB is made in Sec. VII, and our conclusions are summarized in Sec. VIII. The paper is structured so that the casual reader can skip Secs. III, IV, and VI without losing too much continuity; in these

three sections, we will sometimes refer to a more in-depth report [12] for technical descriptions beyond the scope of the present paper.

II. BASIC PRINCIPLES OF THE MEASUREMENT

The aim of the experiment is the precise determination of possible differences between the n - p elastic scattering analyzing powers associated with the neutron spin [$A_n(\theta)$] and with the proton spin [$A_p(\theta)$]. A measurement of this difference to a precision of at least ± 0.001 is needed to provide a meaningful test of theoretical predictions [13–18] of strong-interaction CSB in the n - p system. These predictions (to be discussed further in Sec. VII) are illustrated by the broken curves in Fig. 2, which include the contribution (ΔA_γ) from the electromagnetic spin-orbit interaction in addition to those from various meson-exchange effects thought [1,2] to originate primarily from Δm_{ud} .

In addition to suggesting the order of magnitude of the expected effects, the calculations in Fig. 2 indicate the importance of experimental information on the angular dependence of $\Delta A(\theta)$. There are basically two different angular distribution shapes for the calculated contributions: those arising from the effect of the n - p mass difference on one-pion (ΔA_π) and single- ρ (ΔA_ρ) exchange have shapes characteristic of isospin vector product potentials of the form V_b^{CSB} given in Eq. (2); the vector-meson mixing contribution ($\Delta A_{\rho-\omega}$) and ΔA_γ have shapes typical of the isospin vector difference potentials V_a^{CSB} of Eq. (1). (The deviation of ΔA_γ from $\Delta A_{\rho-\omega}$ at forward angles reflects the influence of high partial waves for the electromagnetic interaction.) This shape difference is largely independent of the details of the cal-

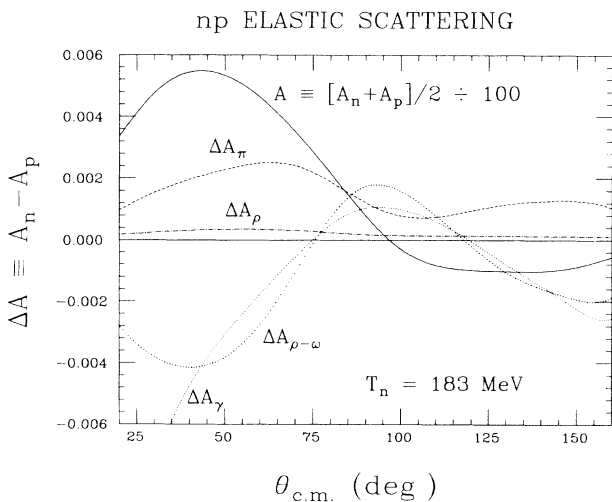


FIG. 2. CSB contributions to $A_n(\theta) - A_p(\theta)$ from various meson exchange processes, as calculated by Holzenkamp, Holinde, and Thomas [15] employing the Bonn potential. The electromagnetic spin-orbit contribution arising from one-photon exchange (ΔA_γ) is also indicated. The 183 MeV “SM89” phase shifts of Ref. [19] were used for the charge-symmetry-conserving amplitudes, as well as to calculate the average analyzing power $A(\theta)$, shown plotted at $\frac{1}{100}$ th scale.

culations; it arises from an intrinsic difference between V_a^{CSB} and V_b^{CSB} terms in the relative signs of even versus odd partial-wave contributions [14]. Thus, measurements of the angular dependence can elucidate the relative importance of the two types of class IV NN potentials.

The apparatus we have used to measure ΔA as a function of angle is illustrated schematically in Fig. 3. Detailed descriptions of the various components will be given in Sec. III. The polarized neutron beam, shown incident from the left in Fig. 3, was produced via the charge-exchange reaction ${}^2\text{H}(\vec{p}, \vec{n})2p$, induced by 200-MeV polarized protons on a 20-cm-thick liquid deuterium target. Approximately 2×10^6 neutrons per second, with a typical vertical polarization of 0.57, a mean bombarding energy $\simeq 183$ MeV, and an energy spread (FWHM) $\simeq 15$ MeV, impinged on the secondary target. For most runs, this was a polarized proton target (PPT) of the “spin refrigerator” design [20]. The PPT had an effective hydrogen thickness of 55 mg/cm² and a typical proton polarization of 0.42. In-beam veto scintillators were used to select only those events that were initiated by neutral particles (V1 in Fig. 3) and did not originate in the downstream wall of the PPT dewar (V2). (Protons produced in reactions in the upstream dewar wall were stopped by obstructions in the PPT dewar before reaching the detectors.) The neutron beam flux and polarization were monitored continuously by an in-beam plastic scintillator (FM) and by a downstream in-beam polarimeter (not pictured in Fig. 3).

Neutrons and protons from scattering events in the target were detected in coincidence by left-right symmetric, large-area detector arrays comprising plastic and (segmented) liquid scintillators and multiwire proportional

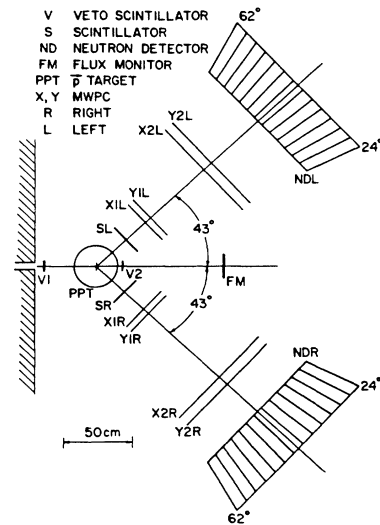


FIG. 3. Schematic top view of the experimental setup indicating the left-right symmetric CSB detector arrays with polarized neutrons incident from the left. A valid event, as defined by the electronics, has no signal in the veto scintillators V1, V2, or in the flux monitor FM, but causes coincident signals in a start scintillator (SL or SR) and at least three of the four wire chambers (MWPC) on the same arm, and in at least one cell of the liquid scintillator neutron detector (NDR or NDL) on the conjugate arm.

chambers. The arrays spanned a large angular range ($24^\circ \leq \theta_{\text{lab}} \leq 62^\circ$), over which both the neutrons and protons from free-scattering events have lab energies $\gtrsim 40$ MeV, facilitating their detection. This allowed us to collect data simultaneously for all c.m. angles between 60° and 120° , a range over which the predicted ΔA_γ remains generally smaller in magnitude than the sum of the expected strong-interaction CSB effects (see Fig. 2). In this region, the coincident neutrons and protons cover the same laboratory angle ranges, so that we made each detector arm sensitive to *both* n and p . In order to extract $\Delta A(\theta)$, we measured the yield of $n_L p_R$ (neutron emerges to the left and proton to the right of the beam direction) vs $n_R p_L$ free-scattering events as a function of the beam and target spin states and of the scattering angle.

The most important demand placed on the detector performance was that it permit clean identification of *free* n - p scattering events. In particular, we had to discriminate effectively against quasifree scattering of neutrons from the *unpolarized* protons bound inside contaminant nuclei in the PPT material (which contained 9 times as many bound as free protons). The discrimination exploited the distinction between an n - p angular correlation that is sharply defined for free-scattering kinematics, but smeared for quasifree scattering by the Fermi motion of the bound protons. We therefore measured the emission angles of both the scattered neutron and the recoil proton, to reconstruct their opening angle and coplanarity with typical FWHM resolutions of 4.0° and 6.0° , respectively. Energy loss and time-of-flight information provided by the scintillators also aided in this discrimination. Resolution limitations, however, still allowed a non-negligible fraction of the quasifree events to survive free-scattering cuts, leaving a background of several percent that had to be accurately subtracted. To measure the (beam) spin dependence of this background independently, we devoted $\sim 15\%$ of the data acquisition time to bombardment of a “dummy” target, constructed to simulate the nonhydrogenic content of the PPT as closely as possible. The PPT and dummy-target runs were interspersed throughout the experiment.

The procedures followed during data acquisition were chosen to minimize systematic errors in the ΔA measurement. To suppress problems that might arise from time drifts in the properties of the beam, the target, or the detection system, we measured $A_n(\theta)$ and $A_p(\theta)$ with the beam and target *simultaneously* polarized (as opposed to the alternating measurements in the work of Ref. [11]). For the same reason, we reversed the spin orientations of both the beam (twice per minute) and the target (once per 10 minutes) relatively frequently. The PPT spin flip was accomplished by slowly (over ~ 40 seconds) rotating the weak (0.059 T) holding field through 180° . This procedure can introduce instrumental asymmetries associated with reversal of the field, rather than the spin, of the target. In order to cancel these, we furthermore reversed the *relative* orientation of the target spin with respect to the holding field twice per day, via the NMR process known as “adiabatic fast passage” (AFP) [21]. Thus, half of our total sample of 4.6×10^7 free \bar{n} - \bar{p} scattering events

were acquired with the PPT spin parallel to the field (we refer to this henceforth as NRM mode), and half with the spin and field antiparallel (AFP mode). Additional run procedures and auxiliary measurements used to reduce and monitor potential systematic errors from other sources are described in Sec. III E.

It is important to keep in mind that the data acquired determine the left-right *asymmetries* correlated with beam [$P_b A_n(\theta)$] or target [$P_t A_p(\theta)$] spin reversal, where P_b and P_t denote the respective polarizations. From these asymmetries, one could make a direct and unqualified comparison of the analyzing powers $A_n(\theta)$ and $A_p(\theta)$ to the desired level of precision *only if* one were able to measure the polarization ratio P_t/P_b independently to an accuracy better than 0.1%. The absence of techniques for suitably accurate polarization measurements places significant limitations on the features of $\Delta A(\theta)$ that can be experimentally determined. In particular, any contribution to $\Delta A(\theta)$ that happens to be proportional to the average analyzing power $A(\theta)$ ($\equiv [A_n(\theta) + A_p(\theta)]/2$) would yield *as its sole effect* an overall normalization difference between $A_n(\theta)$ [$= A(\theta) + \frac{1}{2}\Delta A(\theta)$] and $A_p(\theta)$ [$= A(\theta) - \frac{1}{2}\Delta A(\theta)$]. Such an effect would be indistinguishable experimentally from a small error in the measured value of P_t/P_b . Consequently, the best one can do without greatly improved beam and target polarization monitoring techniques is to measure $\Delta A(\theta)$ *to within a constant times* $A(\theta)$:

$$\Delta A_{\text{meas}}(\theta) = \Delta A_{\text{true}}(\theta) + c A(\theta), \quad (4)$$

where c depends on the error in P_t/P_b .

The ambiguity embodied in Eq. (4) has significant consequences. For example, at the bombarding energy ($E_n = 477$ MeV) of the previous measurement [11], it renders experiments insensitive to the ρ^0 - ω^0 mixing contribution $\Delta A_{\rho-\omega}(\theta)$ which, according to calculations [14–18], strongly resembles $A(\theta)$ in shape. This is not a significant problem at the energy of the present experiment, as can be seen by comparing the calculated ΔA curves in Fig. 2 to the phase-shift calculation [19] of $A(\theta)$ also shown. In particular, $\Delta A_{\rho-\omega}$ has a maximum in the middle of the range covered in our experiment, near the angle ($\theta_0^{\text{c.m.}} \simeq 96^\circ$) where $A(\theta)$ crosses zero. Nonetheless, one must exercise care in order to extract unambiguous information about ΔA , such as its value at θ_0 : Eq. (4) implies $\Delta A_{\text{meas}}(\theta_0) = \Delta A_{\text{true}}(\theta_0)$. In Ref. [11], attention was confined to this one angle. In the present work we have taken a more general approach, making measurements of the beam and target asymmetries over a broad range of angles *simultaneously*, to ensure at least that P_t/P_b is angle independent to the required accuracy. *Shape* differences between $P_b A_n(\theta)$ and $P_t A_p(\theta)$ then reflect some features of the angular dependence of $\Delta A(\theta)$, as discussed in more detail in Sec. V D. In particular, one can determine the *curvature* (but not the slope) of ΔA_{true} in the vicinity of θ_0 , where $A(\theta)$ varies essentially linearly with angle (i.e., $[d^2 A/d\theta^2]_{\theta_0} \approx 0$). This is an interesting quantity because, as seen in Fig. 2,

the curvature is predicted to have opposite sign for potentials of type V_a^{CSB} vs V_b^{CSB} .

III. DETAILS OF THE EXPERIMENT

A. Polarized neutron beam

1. Production and flux monitoring

The experiment was carried out at the Indiana University Cyclotron Facility (IUCF). A detailed layout of the experimental area is shown from an elevation view in Fig. 4. A 200-MeV polarized proton beam from the cyclotron was bent downward by 10° before it impinged on a 20-cm- (3.4 g/cm^2) thick liquid deuterium (LD_2) production target. Neutrons from the charge-exchange reaction ${}^2\text{H}(\vec{p}, \vec{n})2p$ that emerged horizontally (i.e., at $\theta_{\text{lab}}=10^\circ$) from the production target passed through a dipole “sweep” magnet (described further below) and a collimator constructed from lead and steel. The collimator, embedded in a ~ 2 -m-thick steel-reinforced concrete shielding wall, defined a neutron beam 5 cm wide \times 7 cm high at the location of the PPT, 4.2 m downstream from the LD_2 target. Typically, the primary proton beam current was 65 nA, resulting in a secondary beam containing 1.7×10^6 neutrons/s within the energy range (170–193 MeV) of interest for the experiment.

Protons not removed from the primary beam by the LD_2 target were focused into a Faraday cup below floor level, ~ 12 m downstream from the production target. The Faraday cup was split into electrically isolated quadrants and the relative currents were used in a steering feedback loop to keep the beam centered in the beam-dump vacuum pipe, thereby minimizing room background. A similar feedback loop, with a signal derived from the tails of the beam multiple-scattering distribution intercepted by slits downstream of the production target, kept the primary beam position at the LD_2 target stable typically to $\sim \pm 0.1$ mm. The resulting shifts in neutron beam position centroid at the PPT location were smaller by a factor of 2 to 3, since the PPT was considerably closer to the defining edges of the neutron collimator than was the LD_2 target. The neutron beam intensity profile was monitored continuously throughout the experiment, both by reconstruction of the event vertex for n - p coincidences from the PPT (or dummy target) and by

an in-beam “scanning” polarimeter (see Sec. III D 2) located ~ 3 m downstream of the PPT.

The neutron flux (integrated over beam area) was monitored by a fixed in-beam plastic scintillator (FM in Figs. 3 and 4) that intercepted the entire beam. By measuring the arrival time of events initiated in FM with respect to the cyclotron rf signal, we were able to determine the relative flux for the specific neutron bombarding energy range of interest. The ratio of FM yield to the integrated primary proton charge collected by the Faraday cup revealed occasional slow drifts (generally $< \pm 5\%$) which we attributed to changes in the density of the LD_2 target. However, the two independent beam integration techniques were in excellent agreement (to $\lesssim 0.5\%$) for the flux ratios (among different beam-target spin combinations, and between PPT vs dummy target runs) that are relevant to the determination of ΔA .

2. Beam polarization

The use of a vertical reaction plane (with vertical incident polarization) for the ${}^2\text{H}(\vec{p}, \vec{n})2p$ production reaction allowed us to take efficient advantage of the large value for the polarization transfer coefficient $D_{SS'} \approx -0.8$ at $\theta_n = 10^\circ$. The secondary \vec{n} beam thus had a large vertical polarization (of typical magnitude $P_n \approx 0.57$) opposite in sign to that of the incident protons ($P_p \approx 0.73$). The precession of the proton spin in the 10° bending magnet shown in Fig. 4 and the non-negligible value of the polarization transfer coefficient $D_{LS'} (\approx 0.1)$ for the ${}^2\text{H}(\vec{p}, \vec{n})2p$ reaction both served to make P_n sensitive to the magnitude and orientation of any horizontal polarization components present in the proton beam emerging from the cyclotron. Such components (of typical magnitude 0.1) can be introduced by vertical excursions of the circulating beam as it is accelerated through a machine resonance. We used this effect to our advantage to maximize P_n , by extracting the beam from only a single cyclotron turn and choosing the appropriate turn to optimize the orientation of the horizontal polarization component. Both vertical and horizontal proton polarizations were monitored continuously in a p - ${}^{12}\text{C}$ scattering polarimeter mounted between the cyclotron and the polarized neutron facility. During most of the production running, the magnitude and orientation of the proton beam polariza-

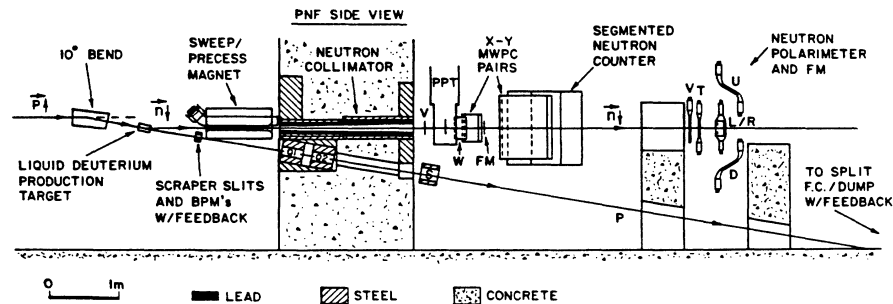


FIG. 4. Side view of the IUCF polarized neutron facility (PNF) and CSB detector arrays. Polarized protons from the cyclotron are bent 10° downwards and, after passing through a liquid deuterium (LD_2) production target, are focused into a Faraday cup below floor level. Feedback loops as indicated hold the beam position steady at the LD_2 target and dump locations. Neutrons from the production target are collimated and may subsequently scatter in the polarized proton target (PPT), CSB flux monitor (FM), or neutron polarimeter. The “sweep” magnet removes charged particles and also precesses horizontal neutron spin components (see text).

tion, and hence P_n , remained stable over time intervals of 1 to 3 days.

The secondary neutron beam also had appreciable horizontal polarization components, arising from small polarization transfer coefficients (most notably, $D_{SL} \approx 0.05$) and from the reaction polarization ($P_{\text{reac}} \approx 0.1$) characterizing ${}^2\text{H}(\bar{p}, \bar{n})2p$ at $\theta_n = 10^\circ$. The component associated with P_{reac} is unique, in that its orientation does *not* reverse when the primary proton beam spin is flipped. The horizontal neutron polarization components can cause small systematic errors in the ΔA measurement, especially if they occur in conjunction with horizontal components in the *target* polarization (see Sec. VID). We therefore used the sweep magnet (see Fig. 4) through which the neutrons passed to effectively cancel these beam spin components, by precessing them through $+90^\circ$ for half of the data acquisition time and -90° for the other half. With this technique, we estimate that the time-averaged horizontal beam polarization components were kept $\lesssim 0.01$ in magnitude.

The vertical polarization of the neutron beam was monitored continuously throughout the experiment via \bar{n} - p scattering asymmetries from the PPT itself and, independently, from an in-beam polarimeter (see Sec. IIID 2) downstream of the main experiment apparatus. These two determinations gave consistent results for P_n for all the PPT runs; only the in-beam polarimeter measurements were available to monitor P_n during dummy-target runs. In each case, the absolute value of P_n is tied to phase-shift calculations [19] of \bar{n} - p analyzing powers, and is subject to a normalization uncertainty we estimate to be $\pm 5\%$.

3. Beam energy distribution

The production reaction and target chosen yielded a neutron beam with relatively high polarization and flux, but also with a rather broad energy distribution. The three-body final state in ${}^2\text{H}(p, n)2p$ results in a continuous neutron energy (E_n) spectrum, characterized by a prominent high-energy peak associated with the 1S_0 resonant final-state interaction of the two outgoing low-energy protons [22]. The shape of the peak in the *observed* E_n spectrum is also strongly influenced by the energy loss of the incident protons in traversing the thick LD_2 production target ($\Delta E_{\text{LD}_2} \approx 15$ MeV for the entire target). Unfortunately, not only the neutron flux, but also the polarization P_n , depends sensitively on E_n , even within the peak region. The P_n variation, if ignored, can introduce a large systematic error in the ΔA measurement (see Secs. VB, VC, and VIF). For a proper analysis of the data, it was necessary to monitor and understand the E_n spectrum quantitatively.

Information on E_n for each detected event is available from the neutron arrival time (t_{rf}) at the secondary target, determined (after certain software corrections described in Sec. IV C 3) with respect to the cyclotron rf signal. The latter signal was stabilized in phase relative to the true emergence time of protons from the cyclotron. A typical t_{rf} spectrum is shown in Fig. 5(a); we are interested here only in events falling within the dominant

prompt peak. The mapping of t_{rf} into E_n values across this peak is complicated by the time resolution function, which is not known *a priori*. We have based the mapping on a model in which the major factors determining the shape of the t_{rf} peak are assumed to be the following: (1) an exponential falloff in the ${}^2\text{H}(p, n)$ cross section as the excitation energy E_{2p}^* of the outgoing $2p$ system increases from zero (in good accord with the dependence predicted for small production angles by a more sophisticated reaction model [22]); (2) a uniform proton bombarding energy (E_p) distribution for $E_p^{\text{cycl}} \geq E_p \geq (E_p^{\text{cycl}} - \Delta E_{\text{LD}_2})$, where

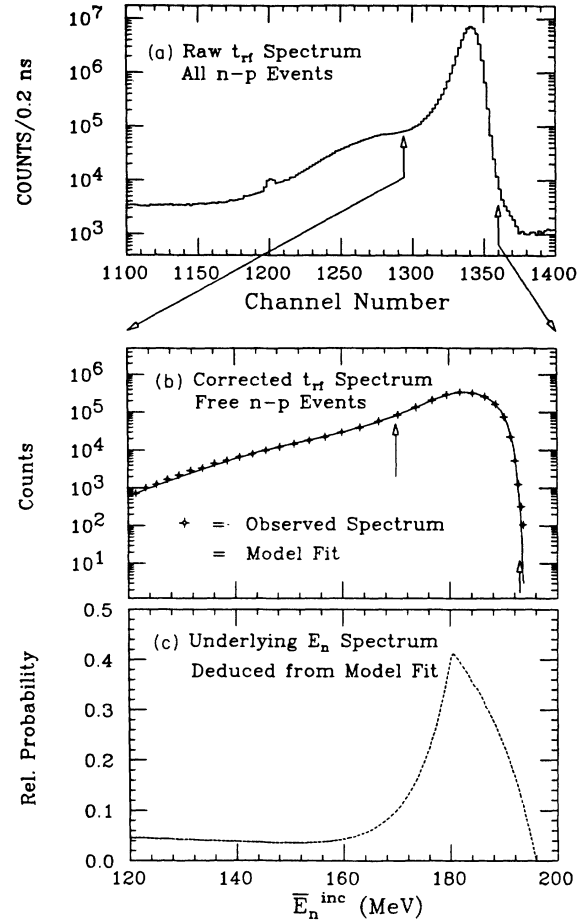


FIG. 5. Spectra related to the neutron beam energy distribution. Shown in (a) is the observed raw spectrum of flight time (t_{rf}) started by the arrival of a recoil proton at the “start” scintillator and stopped by the cyclotron rf signal. This spectrum, spanning a full range of 30 ns, exhibits the pronounced charge-exchange peak characteristic of the ${}^2\text{H}(p, n)$ production reaction. In (b) we plot free-scattering yields in the immediate vicinity of the charge-exchange peak [the region indicated by arrows in spectrum (a)] as a function of the neutron bombarding energy (\bar{E}_n^{inc}) deduced from t_{rf} . The connection between t_{rf} and \bar{E}_n^{inc} is made (see text) with the aid of a model of the underlying energy spectrum that includes adjustable parameters. The optimal solid curve fit to the observed yields in (b) corresponds to the underlying spectrum (after deconvolution of the time resolution function) shown in (c). The arrows in (b) indicate the bombarding energy range (170–193 MeV) included in the primary analysis of the experiment.

E_p^{cycl} is the measured beam energy out of the cyclotron; (3) a Gaussian t_{rf} resolution function. Other features of our energy spectrum model that have only minor influence in our analysis are described elsewhere [12].

The decay constant associated with the E_{2p}^* dependence, the t_{rf} resolution width, and an overall time offset are treated as the main adjustable parameters of the model [12], optimized to fit the observed t_{rf} spectra in the vicinity of the peak. The typical quality of the fit obtained (with reasonable parameter values, see Sec. VIF 1) is illustrated in Fig. 5(b). Here the rf spectrum for free n - p scattering events is plotted vs the mean E_n values (\bar{E}_n^{inc}) contributing to each t_{rf} bin, as deduced from the model fit. Small deviations of the fit from the data for $\bar{E}_n^{\text{inc}} < 150$ MeV and $\bar{E}_n^{\text{inc}} > 193$ MeV are not significant for the results presented in this paper.

As seen in Fig. 5(b), the mean neutron energy at the peak of the t_{rf} spectrum is given by the model, utilizing the *known* LD₂ target thickness and the independently measured values of E_p^{cycl} , to be typically 182.8 MeV. This is in excellent agreement with an independent measurement (183 ± 2 MeV) of this energy, calibrated [12] by comparing high-resolution t_{rf} spectra for ${}^2\text{H}(p, n)$ and ${}^7\text{Li}(p, n_{0,1}){}^7\text{Be}$ over long flight paths. This peak energy varied by up to 1 MeV among the production runs for the $\Delta A(\theta)$ measurement, as a result of changes in E_p^{cycl} (from 200.5 to 201.3 MeV) and in ΔE_{LD_2} (inferred from variations in the ratio of neutron flux monitor to proton beam integrator rates). However, these variations from run to run have little effect on our results for ΔA , since we measured the two analyzing powers, $A_n(\theta)$ and $A_p(\theta)$, *simultaneously*.

The peak shape in Fig. 5(b) is still strongly affected by the time-resolution smearing. When this is deconvoluted within our model, we find the *inferred* underlying E_n spectrum in Fig. 5(c). In particular, we infer a strongly asymmetric energy peak, with FWHM ≈ 15 MeV and a most probable energy (180.5 MeV) significantly displaced from the centroid energy. This peak shape agrees very closely with the energy distribution expected from folding the reaction model calculations of Ref. [22] with the proton beam energy spread introduced by traversal of the LD₂ target. The “cusp” at $E_n \approx 180.5$ MeV seen in Fig. 5(c) corresponds to the maximum E_n value allowed kinematically for ${}^2\text{H}(p, n)$ reactions induced at the downstream end of the LD₂ target. The most important contributions at higher E_n arise also from $E_{2p}^* \approx 0$, but are initiated at higher values of E_p (interaction points upstream in the LD₂). In contrast, to reach $E_n < 180.5$ MeV it is necessary for E_{2p}^* to exceed zero significantly, so we see an exponential falloff characteristic of the assumed E_{2p}^* dependence of the ${}^2\text{H}(p, n)$ cross section. The gentle rise in the deduced yield for $E_n \lesssim 150$ MeV reflects a knockout contribution we have included in our model [12].

4. Secondary \vec{p} beam

Some of the calibration measurements and systematic error tests for the experiment required the use of a second

dary proton beam of similar intensity and geometry to the \vec{n} beam. Such a beam, produced via elastic scattering on the production target, could be obtained simply by turning off the sweep magnet (see Fig. 4) normally energized for \vec{n} beam runs. The LD₂ production target was adequate for several uses of the secondary p beam. However, to study \vec{p} - \vec{p} scattering from the PPT we generally replaced the LD₂ with a 1.5 g/cm² solid ${}^{12}\text{C}$ target, which provided better secondary beam polarization (typically ≈ 0.4). The ${}^{12}\text{C}$ target was especially useful for auxiliary measurements (intended to provide sensitivity to possible *horizontal* components in the target polarization) where we bombarded the PPT with a secondary \vec{p} beam with large *sideways* polarization. To prepare this beam, we used a superconducting spin precession solenoid (located upstream of the beam line shown in Fig. 4) to produce a sideways-polarized primary \vec{p} beam. We were then able to take advantage of the large polarization transfer ($D_{NN}=1$, appropriate to the vertical reaction plane) for the ${}^{12}\text{C}(\vec{p}, \vec{p})$ production reaction to generate the sideways-polarized secondary beam. The \vec{p} - \vec{p} data acquired with the secondary \vec{p} beams will be reported in a future publication; in the present paper we will refer only to results of direct relevance to the assessment of systematic errors in the \vec{n} - \vec{p} $\Delta A(\theta)$ measurement.

B. Polarized proton target

The PPT was based on the “spin refrigerator” technique [20]. Its operation was very similar to that of the device described in Ref. [23], except for a significant difference in sample size. The target material was Yb-doped yttrium ethyl sulfate (YES): $\text{Y}(\text{C}_2\text{H}_5\text{SO}_4)_3 \cdot 9\text{H}_2\text{O}$. The Yb ions in this crystal have a strongly anisotropic g factor; they can be easily polarized at a temperature of ~ 0.5 K in a ~ 1.2 T polarizing field parallel to the crystal symmetry axis. This polarization can then be efficiently transferred to the surrounding free protons by rotating the crystal axis until it is nearly perpendicular to the external field direction. The transfer is effected by a level crossing in the combined spin system of the Yb ions and free protons, which occurs at the orientation where the Yb g factor becomes equal to that of a proton. In practice, the sample was polarized by continuous rotation about a vertical axis for 2 to 3 hours. At a typical rotational frequency of ~ 40 Hz in the 1.2 T polarizing field, we were able to maintain a target temperature of ~ 0.53 K, resulting in peak values of the proton polarization ≈ 0.5 . During data acquisition, the target was held stationary in a reduced magnetic field (0.059 T). Averaged over production running periods, the typical target polarization attained was $P_t \approx 0.42$.

The actual target sample used comprised a number of small pieces of single crystal (typical cross-sectional dimensions \sim a few cm \times 1 cm), all with common thickness (1.0 g/cm²) and crystal axis orientation, arranged on thin Kel-F (hydrogen-free) shelves in a Kel-F frame. The overall lateral dimensions of the YES sample (5 cm horizontally \times 7 cm vertically) were chosen to match the size of the neutron beam.

Several features of the “spin refrigerator” design were

especially well suited to the demands of this experiment. Its modest requirements [23] on cryogenics (a ^3He evaporation refrigerator was sufficient) and on polarizing field uniformity greatly reduced the cost in comparison with more conventional cryogenic PPT's, and facilitated the design of a compact superconducting magnet assembly installed inside the target dewar. The magnet had a sufficiently open coil geometry to accommodate the desired large horizontal and vertical acceptances of our detection system. The polarizing field (1.2 T parallel to the beam direction) was produced by a pair of saddle-shaped coils, while the much smaller and more uniform vertical holding field was generated by two split Helmholtz coil pairs. We were able to achieve long proton spin relaxation times (typically ~ 150 h for decay to $1/e$ of the starting value) at quite low holding fields ($B_{\text{hold}}=0.059$ T during data acquisition). This allowed us to limit the bending of deduced proton trajectories through the field (see Secs. IV C 1 and VI E), and also to flip the target spin relatively frequently (once every 10 min) via adiabatic rotation of \mathbf{B}_{hold} . The latter 180° rotation, utilizing both the vertical and longitudinal field coils, required ~ 40 s to complete. We also used adiabatic fast passage [21] (AFP) to reverse the relative orientations of \mathbf{P}_t and \mathbf{B}_{hold} twice per day; the AFP procedure resulted in a small decrease in target polarization (to about 0.9 of its starting value).

The target polarization was monitored periodically by NMR measurements and continuously via the target asymmetry $P_t A_p(\theta)$ measured for $\vec{n}\text{-}\vec{p}$ scattering. These two methods agreed well within their respective uncertainties. As in the case of the neutron beam polarization, the normalization uncertainty in $A_p(\theta)$ causes an estimated error of $\pm 5\%$ in the absolute value extracted for P_t . However, the normalization errors for the beam and target are strongly correlated, so that the ratio P_t/P_b is determined to $\lesssim \pm 2\%$ (see Sec. V B).

Special care was taken to minimize horizontal components in the holding field, and hence in the target polarization. At an early point during the production running, the horizontal field components were measured at the location of the YES crystals by replacing the target with a rotating Hall probe assembly. These components were then cancelled to an accuracy of $\pm 1 \times 10^{-4}$ T by adjusting the PPT dewar alignment and introducing small longitudinal correction fields produced by the polarizing field magnet. During data acquisition, these correction fields were reversed in direction and changed in magnitude, as appropriate, each time the holding field was flipped. Furthermore, the relative strengths of horizontal field components were monitored continuously with Hall probes mounted just outside the PPT dewar. These measurements indicate that the magnitude of horizontal components was kept $\lesssim 2 \times 10^{-4}$ T in \mathbf{B}_{hold} , and correspondingly $\lesssim 2 \times 10^{-3}$ (absolute) in \mathbf{P}_t , throughout the experiment. These conclusions are confirmed by scattering data discussed in Sec. VI D.

C. Dummy target

In order to subtract accurately those $A(\vec{n}, np)$ quasi-free scattering events that survive all of our free-

scattering kinematic cuts, it was essential to construct a dummy target that simulated the nonhydrogenic content of the YES target as closely as possible. The dummy target was a mixture of teflon (CF_2), yttrium oxide (Y_2O_3), sulfur, and carbon, all contained in a Kel-F frame identical (in composition and in all dimensions) to that which held the YES crystals. The number of atoms/cm² (and of atoms/cm³ as well) of each element (other than H) present in the YES sample was reproduced to within $\pm 2\%$ in the dummy target, except that much of the oxygen in YES was replaced by a combination of F and C, according to the recipe $3\text{O} \rightarrow 2\text{F} + 1\text{C}$. This recipe preserves both the total number of nonhydrogenic nuclei and the number of bound protons in YES. In order to allow for possible small cross-section differences for quasi-free scattering from the F-C combination vs O, we estimate that the effective nonhydrogenic target thickness of the YES was reproduced to within $\pm 4\%$ by the dummy target.

The dummy target was mounted inside two concentric cylinders, one of stainless steel and one of aluminum, to simulate effects of the inner and outer walls of the PPT dewar. The relative alignment of the dummy and polarized targets was checked optically while the PPT was at room temperature, allowing a vertical displacement between them (~ 3 mm) to compensate for the expected contraction of the PPT shaft upon cooling.

D. Detection apparatus

1. Main detector arrays

Coincident $n\text{-}p$ pairs from the PPT or dummy target were detected in two large arrays, positioned symmetrically to the left and right of the \vec{n} beam direction. Each detector arm, spanning the laboratory angle range from 24° to 62° , was sensitive to both neutrons and protons. The layout of one of the two symmetric detector arms is shown in Fig. 6. A thin plastic scintillator, labeled SR in the figure, provided timing and energy loss (ΔE) information for protons. SR and its counterpart SL on the left detector arm were wedge-shaped, with thickness varying from 0.63 cm at the forward-angle edge to 0.24 cm at the large-angle edge, in order to give a more uniform ΔE response for protons from free $n\text{-}p$ scattering. SR and SL were each followed by two pairs of $x\text{-}y$ multiwire proportional chambers (MWPC), with individual wire (LeCroy PCOS II) readout, used to measure the proton angle and to permit ray-tracing back to the point of origin of the event within the extended beam-target interaction area. The wire spacings used were 0.19, 0.25, 0.44, and 0.55 cm for chambers X1, Y1, X2, and Y2 (see Fig. 6), respectively.

At the back of each arm was a large-volume position-sensitive neutron detector. These detectors were constructed by segmenting large vats of (NE 235H mineral-oil based) liquid scintillator into 104 cells (13 columns \times 8 rows), optically separated from one another by 0.1-cm-thick highly polished aluminum walls. Each cell was 8 cm wide by 10 cm high at the front face, 40 cm deep, and tapered so that all four walls pointed toward the center of

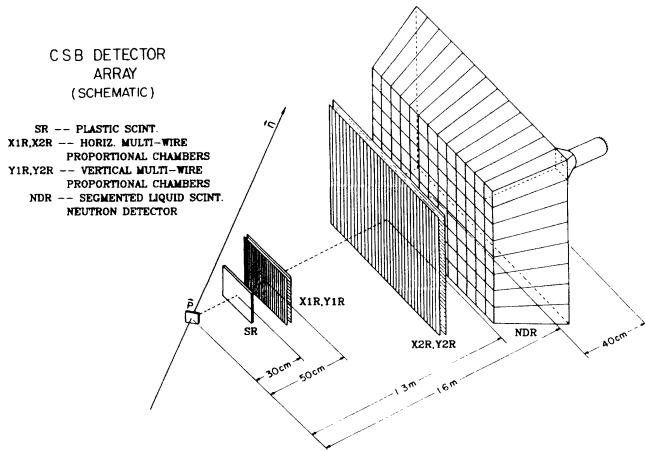


FIG. 6. Schematic illustration in perspective of the right arm of the left-right symmetric detector assembly depicted in Fig. 3. Included are the wedge-shaped plastic “start” scintillator SR, two x - y pairs of multiwire proportional chambers (X1R, Y1R and X2R, Y2R), and the segmented liquid scintillator neutron detector NDR. The active areas of the detectors shown are drawn to scale.

the target (see Fig. 6). Individual photomultiplier tubes (RCA4518 or equivalent) were mounted at the rear of 96 of the cells on each neutron detector; the remaining eight cells (at the most forward angles, top and bottom rows) fell outside the azimuthal angle acceptance defined for n - p free scattering events by the conjugate proton detector. With this system, the neutron detectors provided discretized position information analogous to that from the MWPC’s; we chose this scheme over the slightly better spatial resolution available from the relative timing of signals in phototubes at either end of a scintillator, in order to avoid potential problems from drifts in timing, and hence in the critical position information, over long periods of time. The front wall of the neutron detector was 0.48-cm-thick aluminum, and could be penetrated by protons from free-scattering events at $\theta_p^{\text{lab}} \lesssim 51^\circ$. The detection of protons as well as neutrons in the liquid scintillator was very useful for angle and pulse height calibrations (see Sec. III E 2).

The light collection efficiency within a neutron detector cell was roughly uniform ($\lesssim 10\%$ variations) over the front 25 cm of the cell depth, but for tracks closer to the photomultiplier, there were significant (factor of 2 or more) variations with the distance of the track from the central axis of the cell. Hardware pulse-height thresholds were set typically at a level corresponding to the light collected from a 20 MeV proton (or, equivalently, an 8–10 MeV electron) that stopped near the front face of the cell. With these thresholds the detection efficiency for neutrons from free scattering was typically 20–25%, as determined both from Monte Carlo simulations of the detector response and from comparison of observed and expected yields. For an appreciable fraction of the detected events, a neutron would scatter *twice*, in separate liquid scintillator cells, sometimes surpassing the threshold in both cells. For such events, we attempted in the analysis to distinguish the cell of initial entry by

means of the arrival times of the two signals. The time difference between two cells fired by a single particle could be measured with a FWHM resolution of ~ 0.6 ns (as determined with cosmic rays). In contrast, the significant flight path uncertainty arising from the 40 cm depth of each cell limited the resolution for the neutron time (t_n) with respect to the proton start signal in SL or SR to ~ 2 ns.

The angle information provided by the detector arrays for both n and p was critical in discriminating against quasifree scattering background. Comparable angle resolution (FWHM \sim a few degrees) was obtained for both protons and neutrons, dominated in the latter case by the finite cell size and in the former by multiple scattering in the target and surrounding material. The opening angle (θ_{open}) between the proton and neutron tracks was then determined with a typical FWHM resolution $\approx 4.0^\circ$, and the coplanarity (ϕ_{open}) with FWHM $\approx 6^\circ$. The coordinates (x and y , transverse to the beam direction) of the event origin on the target were each deduced from the proton ray tracing with a spatial resolution that was ~ 0.5 cm for the forward proton angles, but that deteriorated to $\gtrsim 1.0$ cm for $\theta_p^{\text{lab}} \gtrsim 50^\circ$. In addition to the event origin, angle, and t_n information, we extracted a crude ($\sim 10\%$) determination of the proton momentum for each event from the combination of its ΔE in SL or SR and, where available, its energy deposition (E_p^{liq}) in and flight time (t_p^{liq}) to the liquid scintillator.

Special precautions were taken to minimize the sensitivity of the many photomultiplier tubes used in the experiment to fields produced by the (unclamped) PPT holding field magnet. These procedures provided an additional level of suppression (over and above the averaging of NRM and AFP modes described in Sec. II) of instrumental target asymmetries introduced by the holding field reversal. The SL and SR scintillator phototubes were shielded extensively with mu-metal and thick soft-iron cylinders, and were rotated about their axes to minimize empirically their field sensitivity. Space restrictions precluded similarly extensive magnetic shielding of the neutron detector phototubes. Instead, we wound compensation coils around channels that formed part of the support stand for each detector arm. The current in these compensation coils was reversed each time \mathbf{B}_{hold} was reversed, thereby reducing the relevant field shifts at the n -detector phototubes by more than an order of magnitude, to $< \pm 5 \times 10^{-6}$ T. The gain and field sensitivity of the various phototubes were monitored continuously throughout the experiment via the energy deposition for protons from n - p free-scattering events. These data indicated a non-negligible field-dependent gain shift ($\approx \pm 0.4\%$) only for the start scintillator (SR) on the beam right side; this effect was subsequently corrected in the data replay software.

Additional monitoring of the phototube responses was provided by an optical pulsing system incorporating an externally triggered (400 kW peak power) nitrogen laser, a wavelength shifter and beam expander, and optical fibers leading to the phototubes. With a movable slit in front of the array of fibers, we changed the set of cells illuminated with each trigger, so that every phototube was

pulsed at least twice per minute. The optical pulsing system provided independent measurements of phototube gain stability and electronic dead time, and was very useful in setting up electronic timing without beam.

2. Neutron beam polarimeter

A polarimeter for the neutron beam was mounted ~ 3 m downstream of the PPT, behind a second shielding wall, as illustrated in Fig. 4. Left-right asymmetries were measured for \bar{n} - p scattering from a thin (0.32 cm), narrow (~ 3 cm) plastic scintillator target, by detecting the recoil protons in the vicinity of $\theta_{\text{lab}} = 60^\circ$, where the \bar{n} - p analyzing power $\simeq -0.5$ [19]. A veto scintillator preceding the target ensured that only events induced by a neutral beam particle were recorded. The proton detectors each comprised wedge-shaped ΔE and 5-cm-thick E plastic scintillators, subtending 10° in the laboratory frame. The ΔE wedge stopped protons with energy significantly below free-scattering values before they reached the E detector. Particle identification was provided by the $(\Delta E + E)$ sum and the time-of-flight measured over the 80 cm distance between the target and E scintillators. The proton angle was determined, with an effective FWHM resolution $\sim 1^\circ$, from the thickness of wedge scintillator traversed, as deduced from the ratio $\Delta E / (\Delta E + E)$. The total measured proton energy (including that deposited in the target scintillator) was then

corrected, assuming free n - p scattering kinematics, for the deviation of the proton angle from 60° and the deviation from 183 MeV of the neutron bombarding energy (extracted from the target scintillator timing with respect to the cyclotron rf).

The above procedure yields the polarimeter energy spectra shown in Fig. 7, with free-scattering events collected into a well-defined peak near $E_p^{\text{tot}} = 40$ MeV. Background is suppressed at $E_p^{\text{tot}} \lesssim 30$ MeV by the ΔE - E coincidence requirement and at $E_p^{\text{tot}} \gtrsim 80$ MeV by eliminating protons that punch through the E detector. At intermediate energies, the background proton spectrum (from n -carbon reactions in the target scintillator) is spread out by the free-scattering kinematic correction, and exhibits a broad peak around 65 MeV. The gate used to integrate the free peak is shown in Fig. 7. Without any background subtraction, the events within this gate have an effective analyzing power $A_y^{\text{pol}} = -0.38$, calibrated against the free-scattering asymmetries measured simultaneously with the main detector setup (see Sec. III A 2). The event rate within this gate was $\sim 1/\text{s}$ for a total n beam flux of $2 \times 10^6/\text{s}$. The main use of the polarimeter in the data analysis was to monitor the vertical component of the beam polarization for dummy vs PPT runs. By mechanically translating the entire polarimeter assembly continuously (with a period ~ 60 s) across the beam, we also deduced information on the intensity and polarization profiles of the beam.

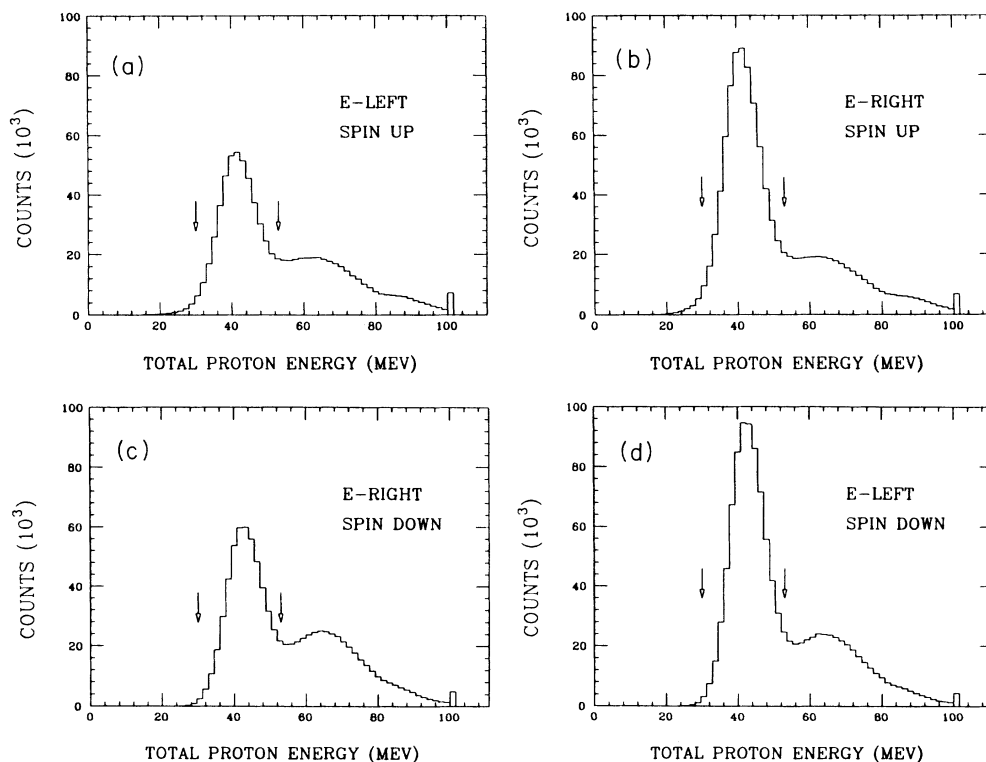


FIG. 7. Neutron beam polarimeter spectra plotted as a function of the total recoiling proton energy for n - p scattering in the polarimeter scintillator target. Spectra for the left detector with neutron beam spin up and down are in (a) and (d), respectively, while the corresponding right detector spectra are displayed in (b) and (c). Integration limits used for the broad free scattering peak near 40 MeV are indicated by the arrows.

E. Data acquisition and run procedures

1. Standard configuration

The electronics processing signals from the main detector arrays established the following event definition: the start scintillator (SL or SR in Fig. 3) and at least three of the four MWPC's on one (the "primary") arm had to fire in coincidence with at least one liquid scintillator cell on the other ("secondary") arm, and without accompanying signals from any of the in-beam veto scintillators (V1, V2, or FM in Fig. 3). By requiring only three MWPC's to fire, we were able to monitor the efficiency of each chamber online; the individual efficiencies for recording at least one hit for the protons of interest were always $\approx 99\%$. If fewer than three MWPC's on the secondary arm had signals, the event was classified as an n_{LP_R} or n_{RP_L} event (for right and left primary arms, respectively), otherwise as a p_{LP_R} event [i.e., the scarce $A(n, 2p)$ events were collected simultaneously]. Special care was taken to treat n_{LP_R} and n_{RP_L} events identically in the electronics and the acquisition software.

The hardware coincidence timing between the two arms was set, in principle, sufficiently loosely to include accidental coincidences in which the secondary arm signal occurred one beam burst (57 ns) later than that from the primary arm. In practice, however, the accidental time peak was partially cut off, or even missed entirely, for some neutron detector cells because of unexpectedly large delay differences between cables of nominally identical length, combined with various restrictions and nonlinearities in the electronic timing. The resulting uncertainty in the subtraction of accidental coincidences introduced a small systematic error in the $\Delta A(\theta)$ results (see Sec. VI B).

Events that satisfied the above definition were processed by two DEC LSI 11/73 front-end microprocessors, which selectively read out digitized timing and pulse height information for only those liquid scintillator cells in which there was a signal surpassing the hardware threshold. In order to limit the number of time- (TDC) and analog-to-digital converter (ADC) channels needed, neutron detector signals from a given arm were multiplexed together in groups of six. The multiplexing was organized so that cells feeding a common TDC or ADC channel were separated spatially by as great a distance as possible.

The microprocessors efficiently packed information from all relevant detectors for storage on magnetic tape and in buffers that were subsequently sorted by a Harris 6064 data acquisition computer. The $\bar{n}\text{-}\bar{p}$ events were interspersed among those arriving from independent data streams set up for the proton beam-line polarimeter, the neutron polarimeter, and the neutron flux monitor.

Electronic and computer dead times were monitored for each event stream by comparing the scaled event rates before and after vetoing by a busy signal. For events from the main detector system, the busy signal was enabled, and the processing of subsequent events blocked, as soon as that part of the event definition associated purely with *plastic* scintillators was satisfied. The busy

signal was reset either upon completion of the front-end processing for a good event, or after it had been determined that appropriate liquid scintillator or MWPC signals were not present. The overall dead time was kept near or below 10% for events from the main detector system [at typical computer input rates of 100–200 events/s or, correspondingly, $(4-10)\times 10^3$ bytes/s] and below 5% for the auxiliary event streams. There was an appreciable spin-dependence to the event rate, and hence to the dead time, for events induced on the PPT, arising from the $\bar{n}\text{-}\bar{p}$ scattering spin correlation C_{NN} , which is large and positive over the entire angle range covered. This spin-dependence does not introduce an appreciable error in the $\Delta A(\theta)$ measurements, because the dead time was the same for n_{LP_R} and n_{RP_L} events and was measured independently for each beam-target spin combination to an accuracy better than ± 0.005 .

The data acquisition software performed diagnostic checks on each incoming event to search for a wide variety of inconsistencies or anomalies indicative of hardware problems. For example, a significant increase in the rate of multiple hits in a given MWPC might signal shielding or electronic problems on that chamber; hits in a given neutron cell accompanied by persistently small ADC outputs might signal a DC offset shift in one of the summing amplifiers used in the multiplexing logic or an inadvertent interchange of cables during electronics checkout. The perceived anomalies were accumulated over ~ 5 -minute intervals, and the experimenters on shift were alerted whenever any of the error rates exceeded preset "worry levels." Analogous checks, performed at each PPT spin flip (i.e., every 10 minutes), compared various scaler ratios and sums to expected values, providing complementary sensitivities to hardware problems. These diagnostics were invaluable in optimizing the efficiency and the reliability of the production data acquisition runs.

The data were acquired in nominal 24-hour "cycles" (each producing $\sim 1.1 \times 10^6$ detected free $\bar{n}\text{-}\bar{p}$ scattering events) during the course of four separate production running periods in 1987–88. During each cycle, the primary proton beam spin was reversed at the ion source approximately twice per minute, and the PPT spin was flipped every ~ 10 min by rotating the holding field. In order to optimize the statistical precision in ΔA , we spent roughly twice as much time collecting data for the antiparallel orientations of the beam and target spins as for parallel orientations. Approximately every four hours, the sweep magnet polarity was reversed, to flip horizontal neutron beam polarization components and cancel possible associated systematic errors (see Sec. VI D). Also every four hours, but interleaved with the sweep magnet changes, the YES crystals were rotated by 180° about a vertical axis, to cancel spurious contributions to ΔA that might arise from spatial variations of the target polarization (see Sec. VI F). The PPT was repolarized twice per cycle, once for a period of ~ 3 h and the second time for ~ 1.5 h. After the longer repolarization, the proton spin direction was reversed with respect to the holding field using adiabatic fast passage (AFP). The longer repolarization time compensated for the small

reduction in polarization caused by the AFP technique, allowing us to maintain essentially equal target polarization magnitudes during the NRM and AFP halves of each cycle. About 3 hours of data with the dummy target were acquired in the middle of each cycle, between the NRM and AFP halves.

In all, we took 41 cycles of production \bar{n} - \bar{p} scattering data, obtaining 4.6×10^7 total free-scattering events. The numbers of these events acquired in NRM vs AFP modes were equal to within 2%, as was also the case for the two sweep magnet polarities and for the two orientations of the YES crystals.

2. Auxiliary runs

Roughly half the time during production runs was devoted to auxiliary measurements that provided in-beam detector calibrations and systematic error checks. These runs often used the secondary proton beam described in Sec. III A 4 and targets other than the PPT or dummy, but required only minor changes to the electronics and run procedures. For example, at the start of each production run, we matched the gains of all 192 liquid scintillator phototubes, via measurements of n - p (from a plastic scintillator target) and p - d (from a CD_2 target) elastic scattering. The gain matching was accomplished by automatic adjustment of the individual high voltage settings to yield the desired kinematic loci for these reactions for the proton energy deposition in the liquid scintillator as a function of proton angle (θ_p). We employed a similar approach to match software timing offsets for all liquid scintillator cells, via the locus of neutron flight time vs θ_p for n - p scattering.

Detector angles were calibrated with p - p and p - d elastic scattering, by requiring complete internal consistency of the information (i.e., event origin and scattering angles) deduced from MWPC ray tracing on the two detector arms, from the liquid scintillator cells fired by the charged particles, and from the known reaction kinematics. An accurate *absolute* determination (to $\lesssim \pm 0.1^\circ$) of the detector angles was facilitated by observation of a well-defined kinematic crossing for p - d scattering (see Fig. 8), wherein the scattered proton and recoil deuteron emerge at equal laboratory angles (51.22° for the bombarding energy used) on opposite arms. The accuracy of *relative* angle measurements with the left vs right detector arms is even better constrained ($\pm 0.02^\circ$).

The procedures followed during the standard \bar{n} - \bar{p} scattering cycles ensured that many potential types of systematic error could be revealed by comparing the data acquired during different halves of the cycles. However, we also acquired an additional 25 cycles of data in “non-standard” modes, to provide various additional systematic error tests. Instrumental beam asymmetries were probed in n - \bar{p} cycles utilizing a nominally unpolarized n beam prepared by “going through the motions” of flipping proton spin at the polarized ion source, but with power turned off to the rf transition units. We used \bar{n} - \bar{p} scattering from *depolarized* YES crystals, with the PPT holding field still being reversed periodically, to examine instrumental target asymmetries. Some cycles in the

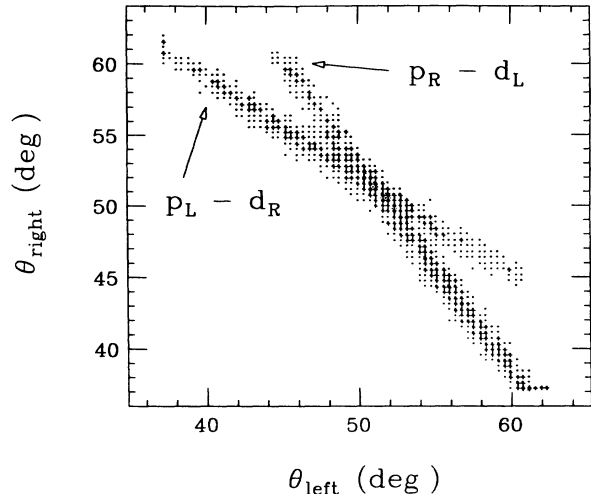


FIG. 8. Angular correlation between protons and deuterons observed in the CSB detector arrays following elastic scattering of a beam of secondary protons from a CD_2 target placed at the usual location of the PPT. The two loci correspond to detection of scattered protons to the left or right with the recoiling deuteron in the conjugate detector. The kinematic crossing at $\theta_L = \theta_R = 51.22^\circ$ provides an absolute calibration of the detector angles at the chosen beam energy.

latter mode were taken with the standard holding field strength (0.059 T) while others used a larger value (0.15 T) to magnify field-dependent spurious contributions to ΔA . Additional cycles utilized \bar{p} - \bar{p} scattering from the PPT (see Sec. III A 4), either to search for horizontal components in the *target* polarization, or to provide a general null test of the measurement procedures (for the scattering of truly indistinguishable particles, ΔA must vanish).

IV. DATA ANALYSIS

A. Goals

The goals of the analysis of the \bar{n} - \bar{p} data were as follows: clean identification of \bar{n} - \bar{p} *free-scattering* events (with a *spin-independent* efficiency); accurate determination of the scattering angle for these events (incorporating various important corrections to the raw measurements); reliable extraction of background-subtracted free-scattering yields as a function of angle, primary detector arm, and beam-target spin combination; and calculation from these yields of various polarization observables, including $\Delta A(\theta)$, for \bar{n} - \bar{p} scattering. Two independent analyses of the data, utilizing completely different software, have been carried out, one at IUCF and the other at the University of Wisconsin. In this section we describe the procedures followed in the IUCF analysis. Important differences in approach between the two analyses are summarized in Ref. [12]. The two analyses have yielded completely consistent results.

B. Identification of free n - p scattering events

The first step in the data analysis was the extraction of certain kinematic variables from the raw detector signals.

The variables were defined for a right-handed coordinate system with z axis along the (central) beam direction, y axis vertical, and origin taken at the center of the small CD_2 target used for angle calibration (see Sec. III E 2). From the recorded positions of the proton in the two MWPC pairs on the primary arm we determined directly the observed angles θ_p, ϕ_p and, by ray-tracing back to the vertical plane that bisects the target longitudinally, the event vertex coordinates $x_{\text{tgt}}, y_{\text{tgt}}$. The latter coordinates were then combined with those corresponding to the center of the cell fired on the secondary-arm liquid scintillator, in order to extract the neutron angles θ_n, ϕ_n and the opening angles $\theta_{\text{open}}, \phi_{\text{open}}$:

$$\phi_{\text{open}} = |\phi_n - \phi_p|, \quad (5)$$

$$\cos\theta_{\text{open}} = \cos\theta_n \cos\theta_p + \sin\theta_n \sin\theta_p \cos\phi_{\text{open}}, \quad (6)$$

where the azimuthal angles ϕ are defined so that they range from -20° to $+20^\circ$ (160° to 200°) for particles detected on the beam left (right) arms.

The extraction of the coordinate and angle information was unambiguous for the majority of events, where a single hit was recorded in each wire chamber as well as in the neutron detector. For $\sim 10\%$ of the events, multiple hits were recorded in one or two MWPC's, produced either by electronic noise or crosstalk in the MWPC readout cards, or by an accidental coincidence with a second particle. In these cases, a hierarchy of tests was performed (including, where available, proton position information from the liquid scintillator on the primary arm) to select the positions most likely corresponding to a single track. Essentially identical ΔA results were obtained whether or not we included these "arbitrated" events, so we have included them for the results reported here. The same is true for those "reconstructed" events ($\sim 3\%$ of the total) where missing information from one of the four MWPC's was inferred under the assumption that $x_{\text{tgt}}=0$ or $y_{\text{tgt}}=0$. For about 5% of the events, two n -detector cells fired. If the time separation between the two hits exceeded 2 ns, only the hit in the earlier cell was retained. For smaller time separations we analyzed only events in spatially adjacent cells, taking the neutron position at the center of the common cell border (which had presumably been crossed by a recoil proton).

The other important kinematic variables measured are the neutron flight time t_n and the proton energy loss ΔE in the start scintillator (SL or SR). Free-scattering events were selected via a set of software gates on the kinematic variables, as illustrated in Figs. 9 and 10. In order to assess the sensitivity of the results to the choice of gates, we often used both "loose" and "tight" windows on a given variable [see Fig. 9(b)–(e) for examples], drawn at intensity levels corresponding roughly to $\sim 1\%$ and $\sim 5\%$, respectively, of the maximum free-scattering yield (after dummy subtraction) for a given θ_p . Before checking the location of an event with respect to most of the kinematic windows, we applied various event-by-event software corrections, described in the following subsection, to the relevant variables. The corrected variables are labeled in Figs. 9 and 10 with a superscript "corr," but for simplicity we generally omit this superscript in the variable labels

in the ensuing text.

Most accidental n - p coincidences were subtracted early in the analysis of each event, utilizing the coarse "real" and "accidental" coincidence gates shown on t_n in Fig. 9(a). Also applied early in the event analysis was a "beam spot" cut, comprising the gate on $x_{\text{tgt}} vs \theta_p$ shown in Fig. 9(e) and analogous gates on $y_{\text{tgt}} vs \theta_p$ and $x_{\text{tgt}}, y_{\text{tgt}} vs \phi_p$. [At large θ_p the "loose" gate in Fig. 9(e) grows broader to accommodate the deterioration in traceback resolution associated with increased proton multiple scattering; the gate also becomes asymmetric (skewed toward opposite sides for $n_L p_R$ vs $n_R p_L$ events) because protons originating on the side of the target nearest the proton detector arm were often obscured by the thick edge of the target frame.] The beam spot cut largely eliminated background originating at sources significantly (\gtrsim a few cm) upstream or downstream of the main target. The remaining background, dominated by gasfree scattering, was most effectively reduced by the gates on $\phi_{\text{open}}, \Delta E vs \theta_p, t_n vs \theta_p$ [see Figs. 9(b)–(d)] and θ_{open} (Fig. 10). We did not include cuts on liquid scintillator information for the protons, since this was available over only part of the angle range.

In addition to the gates shown in Fig. 9, a coarse cut on the rf flight time t_{rf} was used to eliminate events initiated by neutrons with energy $\lesssim 150$ MeV. Two other relatively benign software cuts, on the proton solid angle ($\theta_p vs \phi_p \sin\theta_p$) and the neutron pulse height in the liquid scintillator (≥ 25 MeV equivalent for a proton at the front face of the cell, slightly above the hardware threshold discussed in Sec. III D), were used not so much to reduce background, but rather to ensure essentially equal detector acceptances and efficiencies for $n_L p_R$ and $n_R p_L$ events. The final sample used for accidental coincidence subtraction was defined by events that fell within a $t_n vs \theta_p$ window displaced from the one shown in Fig. 9(d) by the beam burst separation (57 ns), but that passed all other free-scattering cuts. This sample contained $\sim 1.6\%$ (0.6%) of the free-scattering yield when all the cuts were made "loose" ("tight").

The effects of the free-scattering cuts are illustrated in Fig. 10 by various θ_{open} spectra. In these plots, the free n - p scattering events initiated on the main target fall within the peak centered at the kinematically expected value ($\theta_{\text{open}} \simeq 87.2^\circ$). The upper curve in Fig. 10 shows the "raw" spectrum comprising all $n_L p_R$ and $n_R p_L$ events initiated on the PPT. Here the free-scattering peak sits atop a broad background that accounts for roughly 40% of the events in the region $80^\circ \leq \theta_{\text{open}} \leq 94^\circ$. This background is reduced to $\sim 8\%$, with very little loss of free scattering events, when the "loose" cuts described above are imposed (with the exception, of course, of the θ_{open} cut itself). As also shown in Fig. 10, the background can be further reduced to $\sim 2.5\%$, but only at the expense of $\sim 20\%$ losses in the free-scattering yield, by choosing "tight," rather than loose, cuts on $\phi_{\text{open}}, \Delta E vs \theta_p, t_n vs \theta_p$, and the beam spot. The loose- vs tight-cut analyses, to be considered extensively in Sec. V, provide quite different sensitivities to two potentially important sources of systematic error in the ΔA result: the incom-

plete subtraction of background and the removal of free-scattering events with a spin-dependent bias.

With either loose or tight cuts, most of the remaining background in Fig. 10 arises from quasifree scattering, and should be subtracted via dummy-target spectra analyzed with identical software and cuts. The dummy θ_{open} spectrum for tight cuts shown in Fig. 10 has been normalized relative to the other curves by the integrated neutron flux measured with the flux monitor, i.e., assuming that the target thickness and quasifree scattering cross sections are identical to those for the nonhydrogenic contents of the PPT. A crosscheck on this relative normalization is discussed in Sec. V A. Even with the proper normalization, one should *not* expect the dummy

spectrum to account for quite all of the events observed in the “wings” of the PPT θ_{open} spectrum. These wings may include contributions from *free* protons in YES, e.g., from free-scattering events that are “misplaced” when the neutron interacts in two liquid scintillator cells, but produces sufficient light to surpass threshold only in the *second* cell. Other possible mechanisms for populating the wings include *n* or *p* rescattering in the target or surrounding material, *n-p* bremsstrahlung reactions, and incomplete subtraction of accidental coincidences.

The most striking feature of the dummy spectrum in Fig. 10 is that it also displays an appreciable free-scattering peak. This arises from a very small hydrogen contamination, $\sim 1\%$ of the H thickness in the PPT, but

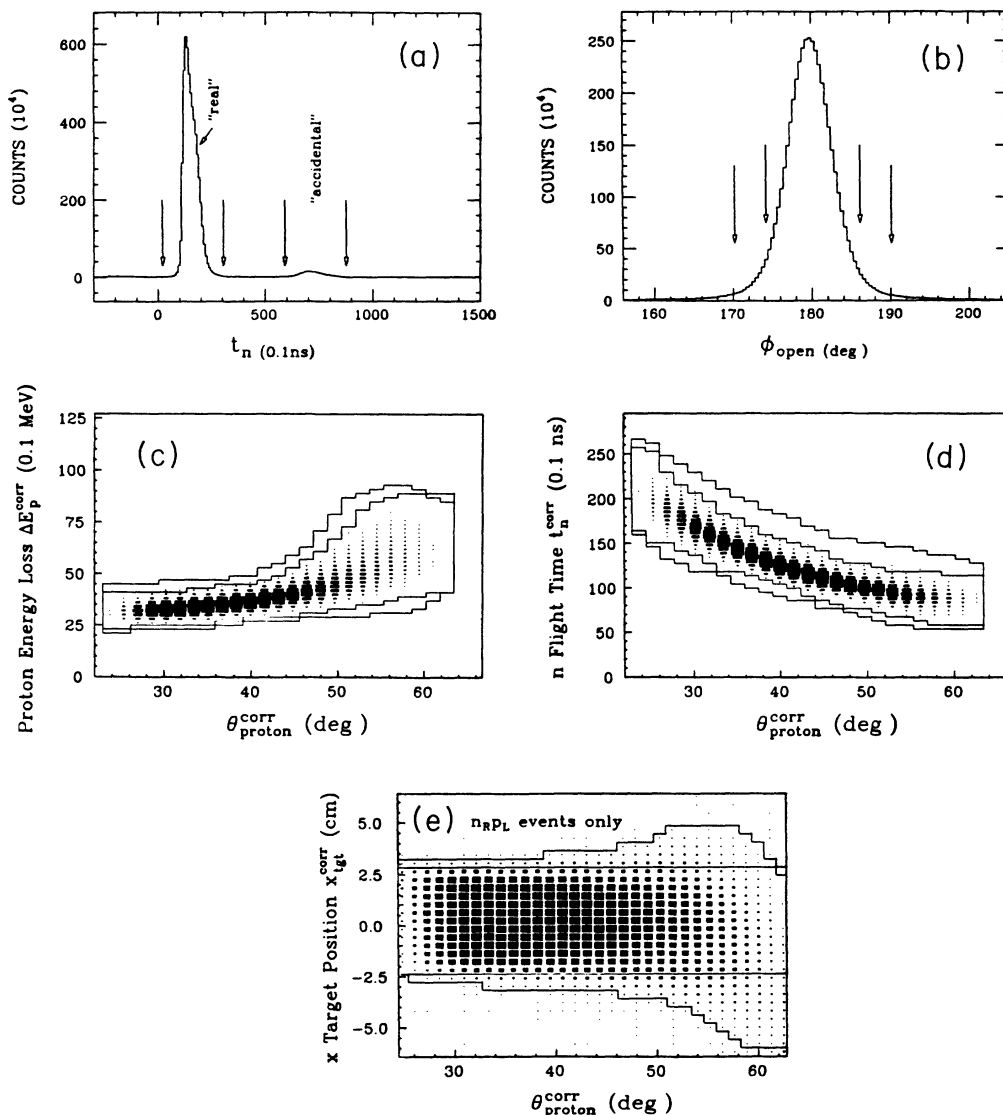


FIG. 9. Typical software cuts used to select free-scattering events, as described in the text. “Real” and “accidental” coincidence gates are indicated in the coarse neutron flight time spectrum of (a), and “loose” and “tight” gates on n - p coplanarity are shown in (b). “Loose” and “tight” two-dimensional windows on the proton energy loss (in the wedge scintillator), the neutron flight time (to the liquid scintillator), and the x coordinate of the deduced event vertex, all versus proton scattering angle, are displayed in (c), (d), (e), respectively. Variable names with a superscript “corr” indicate that the raw measured quantity has been subjected to software corrections described in Sec. IV C.

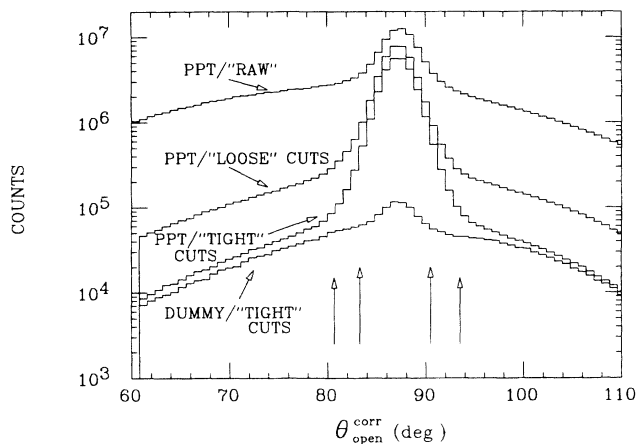


FIG. 10. Opening angle (θ_{open}) spectra for n - p coincidence events produced in the polarized proton target (PPT) and a nearly hydrogen-free “dummy” target. The PPT spectrum is shown both before (RAW) and after “loose” and “tight” software cuts have been applied. The equivalent “dummy” target spectrum is displayed for the tight cut conditions. The arrows indicate the two sorting gates—loose (outer) and tight (inner)—placed on θ_{open} as the final free-scattering condition.

is greatly enhanced by the tight free-scattering cuts. As is discussed in Sec. VIB, this H contamination of the dummy has little effect on $\Delta A(\theta)$, serving primarily to make the PPT polarization appear slightly larger ($\sim 1\%$) in magnitude than it really is.

C. Software corrections to the kinematic variables

A number of corrections were applied in the calculation of kinematic variables, to compensate for some effects of the PPT holding field, the energy and angular spread of the neutron beam, proton multiple scattering, the absence of H from the dummy target, etc. While these corrections are not essential for a qualitative understanding, they are often quite important in reducing the systematic errors and in removing certain correlations among observables that arise from instrumental sources, rather than from the kinematics of the scattering process itself. The corrections are described in some detail in Ref. [12]. Here we concentrate on features important to the later consideration of the results (Sec. V) and the systematic errors (Sec. VI). We include a brief description of Monte Carlo simulations on which some of the corrections are based.

1. Angle corrections

The accurate determination of scattering angle ($\theta_{\text{c.m.}}$) for the analyzed free-scattering events, with reasonably good resolution and, especially, without any spin-dependent bias, is critical for the extraction of $\Delta A(\theta)$. Our determination of $\theta_{\text{c.m.}}$ is based primarily on the measurement of θ_p , which has a granularity far better than its resolution, making the analysis insensitive to the precise choice of angle bins. On the other hand, θ_p must be corrected both for bending in the PPT holding field (this

is done event by event) and (on the average) for multiple scattering. The neutron angle, though measured with much poorer granularity, does not suffer from these effects, and thus is quite useful in helping to determine the θ_p corrections.

The most important correction to θ_p is that for bending in the PPT holding field. The bend angle is typically $\lesssim 0.3^\circ$. The correction is based on a detailed field map and ray-tracing calculations. For given values of the proton momentum (p_p) emerging from the YES target, of the event vertex coordinates ($x_{\text{tgt}}, y_{\text{tgt}}$), and of the angles θ_p and ϕ_p , these calculations [12] allow us to determine corrections $\delta\theta_p$, $\delta\phi_p$, δx_{tgt} to the associated measured quantities. (Note that δy_{tgt} is always very small, and has been neglected in the analysis.) The value used for p_p is deduced [12] from a combination of energy loss, flight time, and scattering angle information measured for the proton. In applying the field correction, we treat the field strength, as represented by the current I_{hold} in the superconducting holding field coils, as a scaling parameter. Its value was adjusted to optimize the correction, as monitored by the stability of the θ_{open} peak centroid vs field direction (expected because θ_n is unaffected by the field). The optimum value determined in this way was $I_{\text{hold}} = 9.94$ A, in excellent agreement (within 0.4%) with the coil current measured independently. From the θ_{open} stability obtained, we conclude that the software field correction is accurate, *on the average*, to $\sim \pm 0.01^\circ$.

Other small corrections made to the measured angles on an event-by-event basis account for the most probable deviation (always $< 1^\circ$) from the central beam ray of the incident neutron direction (inferred [12] from the n - p vertex location and incident neutron energy for the event), and for the weak kinematic variation of θ_{open} with θ_p and neutron bombarding energy. After application of all the event-by-event corrections, the angle variables are labeled θ_p^{corr} and $\theta_{\text{open}}^{\text{corr}}$.

Multiple scattering of the proton, since it is spin-independent, does not directly affect the measurement of ΔA . It can, however, lead to an appreciable systematic distortion of the angle scale in a graph of A vs θ , especially near the ends of the angle range. This may in turn have small indirect effects on ΔA (e.g., on its normalization, via errors introduced in beam- and target-polarization values deduced from phase-shift fits to the measured asymmetries). This systematic distortion is worst for $\theta_p^{\text{lab}} \gtrsim 50^\circ$ ($\theta_{\text{c.m.}} \lesssim 77^\circ$) because (see Sec. IV C 2 below) the probability of detecting a proton from a free-scattering event in the PPT falls off rapidly with increasing angle for the low-energy protons at such large angles. Thus, it is more likely for protons in this range to be multiply scattered into a given measured θ_p bin from smaller than from larger “true” angles. We have corrected for the resulting average shift between the measured and “true” values of θ_p at the end of the analysis, by rebinning the data with the aid of the neutron angle information. The rebinning makes use of Monte Carlo simulations (described below) to calculate the *mean* true emission angle ($\theta_{p_i}^{\text{true}}$) of free-scattering protons detected in coincidence with neutrons assigned to the i th liquid scin-

tillator cell. For each θ_p^{corr} bin analyzed, we determined the distribution of the detected events among neutron-detector cells, and we used this information to obtain a weighted-average (over i) true angle $\bar{\theta}_p^{\text{true}}$. The events were then redistributed in angle to yield a centroid value consistent with $\bar{\theta}_p^{\text{true}}$.

[The redistribution has been performed in two ways: (1) dividing the counts between *two* angle bins straddling $\bar{\theta}_p^{\text{true}}$, as needed to give the correct centroid; (2) using a Gaussian redistribution function with a (multiple-scattering) width inferred from the observed θ_{open} peak shape for the relevant values of θ_p^{corr} . The latter method should give the most reliable approximation to the true distribution of events with respect to $\theta_{\text{c.m.}}$, but it also introduces some unavoidable, and not always desirable, smoothing of statistical fluctuations among adjacent angle bins. We therefore use the 2-point rebinning in the angular distribution results presented in Sec. V, but the Gaussian rebinning for angle-averaged values.]

2. Monte Carlo simulations

Monte Carlo calculations were performed to simulate the fate of neutrons and protons generated in free n - p scattering events, induced by a beam with the observed energy spread and occurring at randomly selected points within the target volume. Although these simulations incorporated [12] extensive modeling of the neutron detector response, including even its possible dependence on scattered neutron spin orientation, this information was not used directly in the data analysis or systematic error evaluation. The primary use of the Monte Carlo results was in the correction for effects of the falloff in *proton* detection efficiency at large angles, and even here the simulations play only a minor role in determining ΔA . The simulated proton tracking included the effects of energy loss, straggling, and multiple scattering in the target and all materials traversed on the path to the detectors, as well as the bending of the proton trajectory in the PPT holding field.

The simulations allow us to understand the *observed* decrease in free-scattering yield for $\theta_p^{\text{lab}} \gtrsim 50^\circ$ (see Fig. 11). The proton efficiency falls off from unity at these angles for several reasons: as the proton energy from free n - p scattering decreases, events initiated within a progressively smaller fraction of the target thickness yield protons capable of penetrating all four MWPC's on the primary arm; in addition, these protons become increasingly more susceptible to removal from the geometric acceptance of the detectors by bending in the PPT holding field and by multiple scattering. (The latter losses are not fully compensated by protons that get multiply scattered from outside to inside the detector acceptance, because the coincident neutrons in those cases generally fall outside the acceptance.)

The Monte Carlo calculations were used to generate tables, as a function of the neutron-detector cell number i , of the probability of detecting the coincident protons (η_{p_i}), and of the true mean scattering angle ($\bar{\theta}_{p_i}^{\text{true}}$) of the protons actually detected. The latter values were used in the final angle binning, as described above. They differ

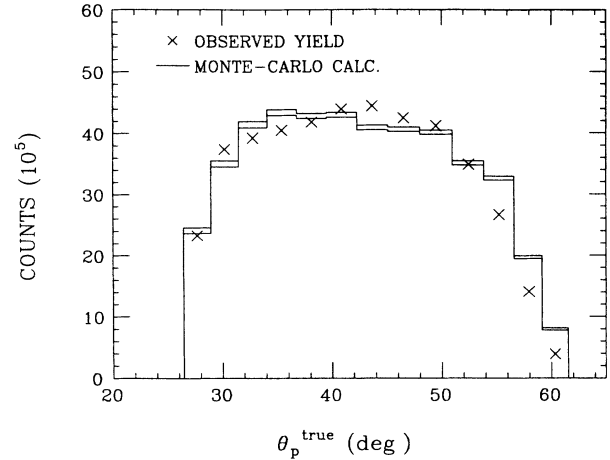


FIG. 11. Yield for free n - p scattering (summed over all spin states) as a function of the “true” proton recoil angle (see text). Each point corresponds to one column of the neutron detectors. The solid lines represent Monte Carlo calculations incorporating the known n - p scattering differential cross section and the simulated neutron- and proton-detector acceptances and efficiencies (but not including software cut efficiencies). The overall normalization of the calculated yields has been chosen to reproduce the average observed yield in the central angle region. Statistical uncertainties in the calculations are indicated by the upper and lower lines plotted for each bin. The calculations account adequately for the large-angle falloff, which results from a decreased proton-detection efficiency for events originating in the upstream portions of the PPT volume.

from the corresponding measured proton angles by as much as 3° , at the largest angles included in the analysis. The η_p values came into play only via their slight predicted *difference* for the dummy vs PPT targets, arising from the absence of hydrogen, and the consequent reduction in energy loss, in the dummy target. This efficiency difference affects the dummy subtraction normalization at large θ_p . The Monte Carlo tables were used in analyzing all events, but their influence is negligible for $30^\circ \leq \theta_p^{\text{lab}} \leq 50^\circ$.

3. Energy and flight time corrections

In order to minimize a systematic error in ΔA that arises from the variation of beam polarization with bombarding energy E_n^{inc} , it is important to determine E_n^{inc} for each event from its measured arrival time (t_{rf}) at the start scintillator (SL or SR in Fig. 3) with respect to the cyclotron rf signal. The measured value of t_{rf} was first corrected (yielding $t_{\text{rf}}^{\text{corr}}$) for the calculated flight time of the proton from the target to the start scintillator (~ 1 – 7 ns, depending on p_p) and for the propagation time ($\lesssim 1$ ns) of photons within that scintillator. The latter correction was based on the timing response of the scintillators measured as a function of position with radioactive sources, and on the position of impact of the proton deduced from the MWPC ray tracing. (After correction for the photon propagation time, the intrinsic timing resolution of the start scintillators was inferred to be better than 0.5 ns

FWHM.) The same corrections were applied also to the neutron flight time t_n , together with allowances for path length differences to different cells, to deduce the detected neutron velocity for each event.

The mapping of $t_{\text{rf}}^{\text{corr}}$ into \bar{E}_n^{inc} (the mean energy contributing to a given t_{rf} bin) was based on the energy spectrum model described in Sec. III A 3. In addition to facilitating analysis of the data in relatively narrow slices of bombarding energy, the determination of \bar{E}_n^{inc} allowed us to draw slightly tighter windows on several variables—most notably t_n , ΔE_p , and θ_{open} —after correcting them for the expected small kinematic variations with \bar{E}_n^{inc} .

The proton energy loss ΔE_p in the wedge-shaped start scintillator was corrected for spatial variations in the light collection efficiency, which were measured independently with a monoenergetic low-energy proton beam. In addition, to minimize any field dependence in the efficiency of the software cuts, we corrected ΔE_p for certain effects of the PPT holding field. The most important of these arose from the wedge shape: protons assigned to a given corrected (for field bending) angle bin θ_p^{corr} would have traversed systematically different thicknesses of scintillator for opposite field orientations. The actual thickness traversed for each event was therefore deduced from the ray tracing, and the measured ΔE_p corrected for the difference from the nominal thickness appropriate to θ_p^{corr} . After the latter correction was made, it was possible to observe a small residual effect attributable to a field-dependent gain shift ($\approx \pm 0.4\%$) in the SR scintillator phototube. This was corrected in the final sorting of the data.

Throughout the remainder of the paper, we deal exclusively with corrected values of the kinematic variables, but we omit explicit inclusion of the superscript “corr” in the symbols.

D. Extraction of polarization observables

The final results of the data replay, after subtraction of the dummy target data, are n - p free scattering yields measured as a function of θ_p^{ab} , \bar{E}_n^{inc} , and “spin state.” The latter variable takes on eight distinct values, separating $n_L p_R$ from $n_R p_L$ events, as well as the four beam-target spin combinations. The distributions of these yields, summed over the range $170 \leq \bar{E}_n^{\text{inc}} \leq 193$ MeV, are shown in Fig. 12. In addition, we determine the flux monitor yield vs \bar{E}_n^{inc} and beam-target spin combination to allow relative normalization of the n - p scattering yields. From the normalized yields for each θ_p^{ab} and \bar{E}_n^{inc} bin, we can determine eight independent quantities, which differ from one another in their symmetry properties under three operations: interchange of left and right, neutron spin reversal, and proton spin reversal. These eight observables, labeled T_{1-8} , are expressed in Table I (after dividing each by the unpolarized differential cross section) in terms of beam and target polarization components and n - p scattering analyzing powers (A_n, A_p) and spin-correlation coefficients (C_{ij}). It is useful for the subsequent discussion of systematic errors to include in Table I the possible small contributions to T_{1-8} associated with horizontal

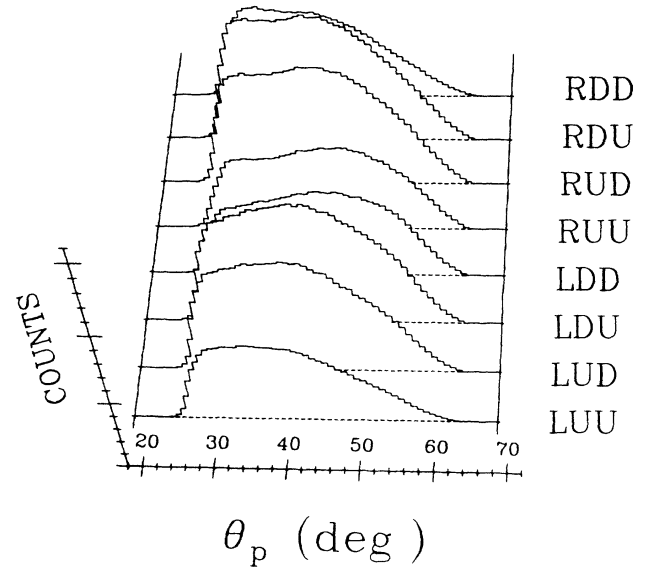


FIG. 12. Spectra representing the yield of free \bar{n} - \bar{p} scattering events (after dummy subtraction) versus proton scattering angle for the eight different combinations of proton detector arm (“Left” or “Right”) and \bar{n} beam and \bar{p} target spin projections (“Up” or “Down”). The labels on the right side of the figure specify, in order, the p arm, \bar{n} spin, and \bar{p} spin.

polarization components (labeled by subscripts L for longitudinal and S for sideways, as opposed to N for normal to the scattering plane) and with polarization magnitude differences (denoted by \bar{P}) between the “up” and “down” spin states. Under the conditions of the present experiment, we expect $T_{2,3,5,8}$ all to be very small over the entire angle range.

The goal of the experiment was the accurate determination (in the notation of Table I) of the asymmetries $P_N^{(b)} A_n(\theta)$ and $P_N^{(t)} A_p(\theta)$, which dominate the quantities T_6 and T_7 , respectively. Their extraction from the measured yields is straightforward if one neglects contaminating terms that are of second or higher order in the following small quantities: left-right efficiency differences, $\bar{P}_N^{(b)}, \bar{P}_N^{(t)}$, and the horizontal polarization components. In order to monitor the effect of such terms (see Sec. VID), we extracted ΔA via several formulas, which differed only in their sensitivities to the second-order contaminations; these methods always yielded results that agreed to within a few $\times 10^{-5}$.

The various formulas for ΔA can be subdivided into two classes of approach. In the first, we extract the beam (T_6) and target (T_7) asymmetries separately from the observed free-scattering yields (L_{++}, R_{+-} , etc., where the letter represents the proton detection arm and the first and second subscripts denote the neutron beam and proton target spin states, respectively) and flux monitor sums (I_{++} , etc.). The asymmetries are calculated in the usual way:

$$T_{6,7} = (r_{6,7} - 1) / (r_{6,7} + 1), \quad (7)$$

where the left-right ratios $r_{6,7}$ can be extracted from the yields via various expressions; e.g.,

TABLE I. The eight spin-dependent n - p scattering cross sections sampled with polarized beam, polarized target, and left (l)–right (r) symmetric detectors. The notation is explained in the text. The analyzing powers A_n and A_p , and the spin correlation parameters C_{ij} , and hence each of the quantities T_{1-8} , are functions of scattering angle.

| $l \leftrightarrow r$ | Symmetry under Beam spin reversal | Target spin reversal | Expression for the ratio of polarized to unpolarized cross section |
|-----------------------|---|-------------------------|--|
| + | + | + | $T_1 = 1 + \bar{P}_N^{(b)} \bar{P}_N^{(t)} C_{NN} + \bar{P}_S^{(b)} \bar{P}_S^{(t)} C_{SS} + \bar{P}_L^{(b)} \bar{P}_L^{(t)} C_{LL}$ |
| + | – | + | $T_2 = P_N^{(b)} \bar{P}_N^{(t)} C_{NN} + P_S^{(b)} \bar{P}_S^{(t)} C_{SS} + P_L^{(b)} \bar{P}_L^{(t)} C_{LL}$ |
| + | + | – | $T_3 = \bar{P}_N^{(b)} P_N^{(t)} C_{NN} + \bar{P}_S^{(b)} P_S^{(t)} C_{SS} + \bar{P}_L^{(b)} P_L^{(t)} C_{LL}$ |
| + | – | – | $T_4 = P_N^{(b)} P_N^{(t)} C_{NN} + P_S^{(b)} P_S^{(t)} C_{SS} + P_L^{(b)} P_L^{(t)} C_{LL}$ |
| – | + | + | $T_5 = \bar{P}_N^{(b)} A_n + \bar{P}_N^{(t)} A_p + \bar{P}_S^{(b)} \bar{P}_L^{(t)} C_{SL} + \bar{P}_L^{(b)} \bar{P}_S^{(t)} C_{LS}$ |
| – | – | + | $T_6 = P_N^{(b)} A_n + P_S^{(b)} \bar{P}_L^{(t)} C_{SL} + P_L^{(b)} \bar{P}_S^{(t)} C_{LS}$ |
| – | + | – | $T_7 = P_N^{(t)} A_p + \bar{P}_S^{(b)} P_L^{(t)} C_{SL} + \bar{P}_L^{(b)} P_S^{(t)} C_{LS}$ |
| – | – | – | $T_8 = P_S^{(b)} P_L^{(t)} C_{SL} + P_L^{(b)} P_S^{(t)} C_{LS}$ |

$$r_6 = \left\{ \frac{\left[\sum_{i=+,-} (L_{+i}/I_{+i}) \right] \left[\sum_j (R_{-j}/I_{-j}) \right]}{\left[\sum_k (L_{-k}/I_{-k}) \right] \left[\sum_l (R_{+l}/I_{+l}) \right]} \right\}^{1/2},$$

$$r_7 = \left\{ \frac{\left[\sum_{i=+,-} (L_{i+}/I_{i+}) \right] \left[\sum_j (R_{j-}/I_{j-}) \right]}{\left[\sum_k (L_{k-}/I_{k-}) \right] \left[\sum_l (R_{l+}/I_{l+}) \right]} \right\}^{1/2} \quad (8)$$

or, alternatively,

$$r_6 = \frac{\sum_{i=+,-} (L_{+i}/I_{+i} + R_{-i}/I_{-i})}{\sum_j (L_{-j}/I_{-j} + R_{+j}/I_{+j})},$$

$$r_7 = \frac{\sum_i (L_{i+}/I_{i+} + R_{i-}/I_{i-})}{\sum_j (L_{j-}/I_{j-} + R_{j+}/I_{j+})}. \quad (9)$$

$$X = \left(\frac{I_{++} I_{--}}{I_{+-} I_{-+}} \right)^{1/2} \left(\frac{L_{+-} L_{-+} R_{+-} R_{-+}}{L_{++} L_{--} R_{++} R_{--}} \right)^{1/4}$$

$$\times \left\{ \frac{(L_{+-}/R_{+-})^{1/2} - (R_{+-}/L_{+-})^{1/2} + (R_{-+}/L_{-+})^{1/2} - (L_{-+}/R_{-+})^{1/2}}{(L_{++}/R_{++})^{1/2} - (R_{++}/L_{++})^{1/2} + (R_{--}/L_{--})^{1/2} - (L_{--}/R_{--})^{1/2}} \right\}. \quad (11)$$

We then extract ΔA using

$$\Delta A(\theta) = 2A(\theta)[X(\theta) - \zeta]/[1 - \zeta X(\theta)], \quad (12)$$

where $\zeta \equiv (1 - \rho)/(1 + \rho)$ is angle independent, and

$$A(\theta) \equiv [A_n(\theta) + A_p(\theta)]/2$$

$$= [\rho^{1/2} T_6(\theta) + \rho^{-1/2} T_7(\theta)]/2P \quad (13)$$

can be evaluated from Eqs. (7) and (8).

It can be seen from either Eq. (10) or (12) that the major ambiguity in extracting $\Delta A(\theta)$ comes from our imprecise knowledge of the polarization ratio ρ (or the

In order to extract ΔA from T_6 and T_7 , we need to know the ratio of target-to-beam polarizations ($\rho = P_t/P_b$) and their geometric mean value $P = (P_b P_t)^{1/2}$:

$$\Delta A = \frac{1}{P} (\rho^{1/2} T_6 - \rho^{-1/2} T_7). \quad (10)$$

In evaluating the error in ΔA , we note that although the statistical uncertainties in T_6 and T_7 are very strongly correlated with one another, those in the sum ($T_6 + T_7$, determined from the $++$ and $--$ spin states) and the difference ($T_6 - T_7$, determined from $+-$ and $-+$) are essentially uncorrelated.

In the second basic approach to extracting ΔA , we deal directly with the latter uncorrelated quantities, deriving their ratio

$$X(\theta) \equiv [T_6(\theta) - T_7(\theta)]/[T_6(\theta) + T_7(\theta)]$$

from the measured yields, e.g., via

related quantity ζ). In particular, if we recall that $A_n(\theta) = A(\theta) + \Delta A(\theta)/2$, and $A_p(\theta) = A(\theta) - \Delta A(\theta)/2$, then Eq. (10) directly yields the sensitivity of the extracted ΔA to polarization errors:

$$\delta(\Delta A) = A(\theta) \frac{\delta\rho}{\rho} - \Delta A(\theta) \frac{\delta P}{P}. \quad (14)$$

Thus, the uncertainty (estimated to be $\pm 5\%$ for our measurements) in the absolute value of the mean polarization P gives rise simply to an overall *scale factor* uncertainty in the extracted values of $\Delta A(\theta)$. In contrast, *an error in the ratio ρ introduces a spurious contribution to ΔA that*

has the same variation with angle as the average analyzing power $A(\theta)$. Conversely, any *real* physical contribution to $\Delta A(\theta)$ that happens to be proportional to $A(\theta)$ gives merely an angle-independent contribution to $X(\theta)$ [see Eq. (12)], and cannot be distinguished from an error in ζ (or ρ). As a result (already noted in Sec. II), the best one can do, *given present technical limits on the accuracy of absolute polarization measurements*, is to deduce from the data a quantity

$$\langle \Delta A(\theta) \rangle = \Delta A_{\text{true}}(\theta) + cA(\theta), \quad (15)$$

where the constant c is given [24] by the unknown error $\delta\rho/\rho$.

In subsequent sections, we present our results for “ ΔA ” in two different ways, designed to provide meaningful comparisons with theoretical predictions of $\Delta A_{\text{true}}(\theta)$, even in the face of the ambiguity embodied in Eq. (15). First, we average the data over certain “magic” angle ranges for which $\langle A(\theta) \rangle$ vanishes, so that

$$\langle \langle \Delta A \rangle \rangle_{\text{magic}} = \langle \Delta A_{\text{true}}(\theta) \rangle_{\text{magic}}. \quad (16)$$

[As one shrinks the width of the “magic” range to zero, one can extract the value of ΔA_{true} at the single angle θ_0 where $A(\theta)$ crosses zero; this is essentially the procedure followed in Ref. [11].] Second, we compare experimental and theoretical angular distributions for analogous quantities “ $\Delta A(\theta)$.” For this purpose, we construct

$$\langle \Delta A_{\text{theory}}(\theta) \rangle = \Delta A_{\text{theory}}(\theta) + c_{\text{theory}}A(\theta), \quad (17)$$

and we use identical prescriptions (described further in Sec. VD) to “optimize” independently the experimental and theoretical values of c , thereby extracting directly comparable parts of $\Delta A_{\text{true}}(\theta)$.

In addition to $A_n(\theta)$, $A_p(\theta)$, and “ $\Delta A(\theta)$ ”, the \bar{n} - \bar{p} scattering spin correlation parameter $C_{NN}(\theta)$ can be extracted with high precision from the data obtained, via T_4 in Table I. The C_{NN} results are presented elsewhere [25]. This observable is, however, useful for the present analysis in helping to distinguish free- from quasifree-scattering background, and will be discussed in this context in Sec. VA. We have also extracted the quantities $T_{2,3,8}(\theta)$, all of which are expected to be very small, in order to provide crosschecks on our assumptions.

V. RESULTS

A. Dummy-to-PPT normalization

As explained in Sec. IV B, a significant background remains under the free-scattering peak in the θ_{open} spectrum (see Fig. 10) even after the imposition of all cuts. The dominant source of this background, namely, quasi-free (qf) scattering of neutrons from protons bound inside contaminant nuclei in the PPT, is characterized by polarization observables that differ substantially from the free-scattering values. Its accurate subtraction, via the data acquired with the dummy target, is thus critical for all of the results presented below. In normalizing the dummy data to that for the PPT, we must assume some ratio of the relevant (nonhydrogenic) target thicknesses,

effective qf scattering cross sections, and detector acceptances. We combine these factors below into a single ratio (t_D/t_{PPT}) of “effective” dummy-to-PPT thicknesses. The careful construction of the dummy target suggests $t_D/t_{\text{PPT}}=1.00$ with an estimated uncertainty of ± 0.04 , incorporating (see Sec. III C) possible differences in both composition and qf cross section between the two targets. Because the use of this thickness ratio leaves appreciable apparent background in the dummy-subtracted θ_{open} spectrum [see Fig. 13(a)], it is desirable to provide an independent in-beam crosscheck of its validity.

A useful crosscheck is obtained by extracting C_{NN} for the background on either side of the θ_{open} peak. The C_{NN} asymmetry (T_4 in Table I) distinguishes clearly between the two major contributors to the background: it vanishes for any reaction (including qf scattering) induced on the *bound* (unpolarized) nucleons in the target, while it is

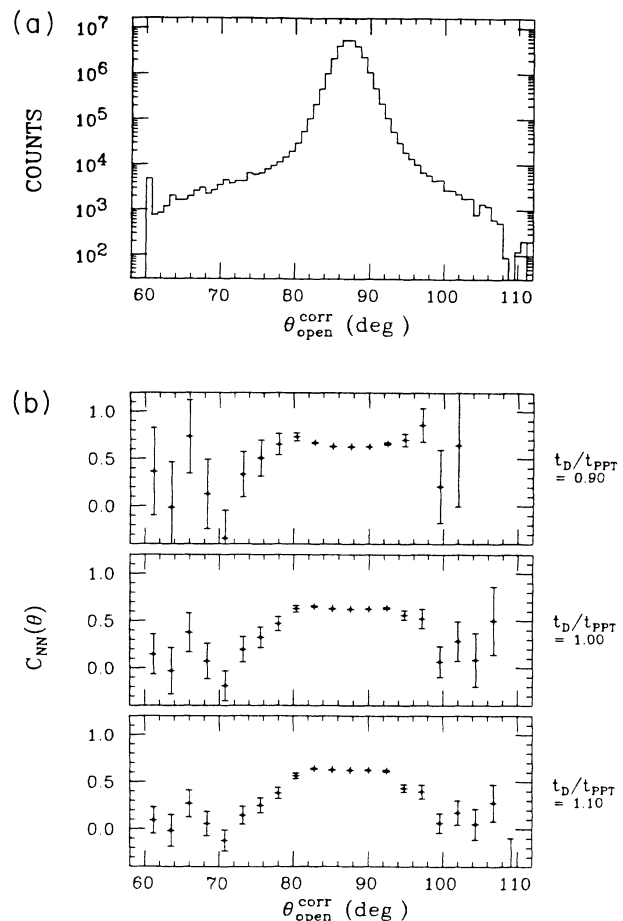


FIG. 13. Illustration of the sensitivity of the normal spin correlation C_{NN} to the relative thickness assumed for the “dummy” target vs PPT, shown for events that pass all the tight free-scattering cuts. The bottom panel shows C_{NN} as a function of opening angle for three different values of the assumed thickness ratio t_D/t_{PPT} . The values extracted for C_{NN} in the near “wings” of the free-scattering peak ($\theta_{\text{open}} \approx 77^\circ-82^\circ, 92^\circ-97^\circ$) are closest to the expected values (see text) when $t_D/t_{\text{PPT}}=1.00$. This value has been used for the ratio to generate the dummy-subtracted opening angle spectrum in the top panel.

large ($C_{NN} \approx 0.60$ – 0.65) and nearly angle independent (over the range of the measurement, see Ref. [25]) for true free-scattering events “misplaced” by neutron rescattering before or inside the liquid scintillator. If these are the *only* significant background contributions, then after the dummy subtraction C_{NN} in the “wings” of the θ_{open} peak should be <0.6 (>0.65) if the bound-nucleon events have been under- (over-) subtracted.

Evidence supporting this two-component background assumption comes from analysis of those events that *fail* one or more of the loose free-scattering kinematic cuts (on θ_{open} , ϕ_{open} , ΔE_p vs θ_p , and t_n vs θ_p). This sample of events is dominated ($\sim 93\%$) by reactions on bound nucleons. Nonetheless, after dummy subtraction with the *appropriate relative normalization*, the surviving fraction of these events has polarization observables [$A_n(\theta)$, $A_p(\theta)$, $C_{NN}(\theta)$] quite consistent with those for *free* \bar{n} - \bar{p} scattering from the PPT. This is illustrated in Fig. 14(b) for C_{NN} , which is particularly sensitive to the value of t_D/t_{PPT} assumed in the subtraction. For $t_D/t_{\text{PPT}} = 0.91 \pm 0.01$ [leading to the subtracted spectrum shown in Fig. 14(a)], $C_{NN} \approx 0.6$ over the entire range of θ_{open} .

The deviation from unity of the optimum thickness ratio deduced from Fig. 14 has been traced to a surplus of apparent qf scattering events from the bottom and beam right edges of the YES target, with respect to the dummy. This surplus can be explained quantitatively by ~ 1 mm vertical and horizontal relative misalignments of the two targets when the PPT was cold, causing greater beam illumination of the (hydrogen-free) Kel-F frame for the YES target. Since the frame edges have ~ 2.5 times the areal density of the YES crystals, a small misalignment can cause a sizable change in the effective target thickness for qf scattering.

A similar surplus of background events from the Kel-F is apparent for those PPT events that pass all the *loose* free-scattering cuts. These cuts (see Fig. 9) include a “beam-spot” gate identical to that imposed on the “non-free” events in Fig. 14. For events that satisfy the loose cuts, the C_{NN} analysis (not illustrated in a figure) yields an effective target thickness ratio $t_D/t_{\text{PPT}} = 0.92 \pm 0.05$ in order to give results consistent with free scattering in the “near wings” ($\theta_{\text{open}} \approx 77^\circ$ – 82° , 92° – 97°) of the θ_{open} peak. The uncertainty quoted here for t_D/t_{PPT} is larger than for the analysis of Fig. 14, despite improved statistical precision in C_{NN} , because the bound-nucleon events form a much smaller fraction of the sample that pass the loose cuts than of the sample that fail them, yielding reduced sensitivity to the dummy normalization. This uncertainty in dummy normalization causes a significant systematic error ($\approx \pm 4 \times 10^{-4}$) in the values of ΔA extracted from the loose-cut sample [26].

For the latter reason, we have chosen to base our primary ΔA results on those events that pass the *tight* free-scattering cuts, which include a considerably tighter beam spot cut [see Fig. 9(e)]. The tight cuts substantially reduce the overall bound-nucleon background (from $\sim 8\%$ to $\sim 2.5\%$), and hence the sensitivity of ΔA to the dummy normalization. Moreover, they appear to remove selectively most of the *excess* qf events from the Kel-F

frame. One thus obtains reasonable behavior of C_{NN} as a function of θ_{open} at the *expected* thickness ratio ($t_D/t_{\text{PPT}} = 1.00$), as illustrated in Fig. 13. The slight upward curvature seen in the θ_{open} peak region in Fig. 13(b) for $t_D/t_{\text{PPT}} = 1.00$ is consistent with expectations: the outer edges of the peak have larger relative contributions from events at $\theta_p^{\text{lab}} \gtrsim 50^\circ$ ($\theta_{\text{c.m.}} \lesssim 77^\circ$), where the θ_{open} resolution deteriorates (due to increased proton multiple scattering) and C_{NN} increases slightly (to 0.65 – 0.70) in magnitude [25]. This curvature becomes excessive when we use $t_D/t_{\text{PPT}} < 0.94$ and becomes too small (or negative) for $t_D/t_{\text{PPT}} > 1.06$.

The tight cuts also largely eliminate “misplaced” free-scattering events from the far wings of the θ_{open} spectrum ($\gtrsim 15^\circ$ displacement from the peak center): an event in

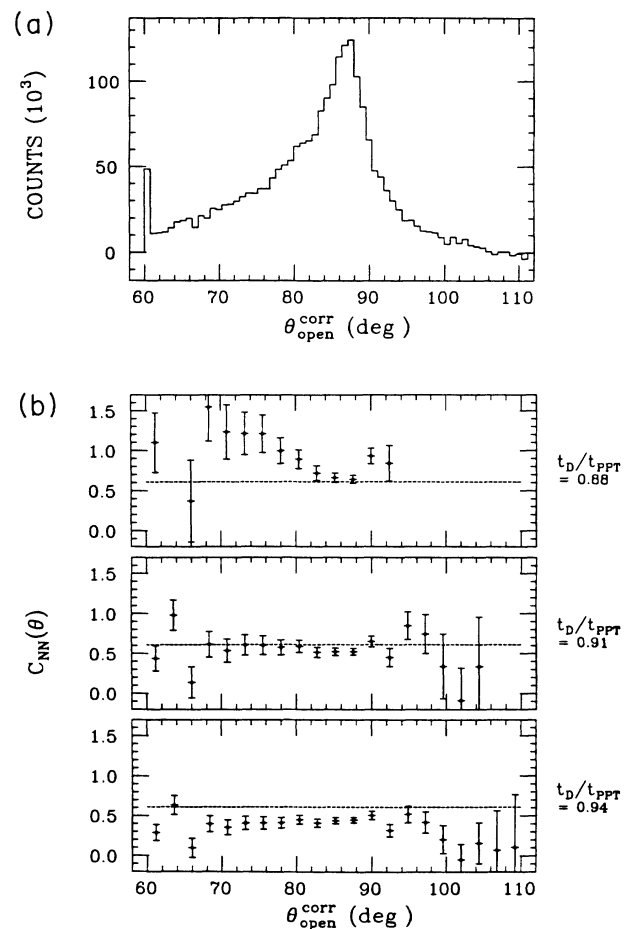


FIG. 14. Similar to Fig. 13, but for the sample of n - p events that *fail* one or more of the “loose” free scattering cuts. This sample is dominated by quasifree scattering, so that most ($\sim 93\%$) of the events are removed by the dummy subtraction. The values of C_{NN} extracted for the remaining events are very sensitive to t_D/t_{PPT} . A ratio of 0.91 most closely reproduces free-scattering values for C_{NN} (≈ 0.60 , indicated by the dashed lines) and has been used for the dummy subtraction in generating the θ_{open} spectrum in the top panel. Further analysis of these events revealed a relative misalignment of the dummy target and the cold PPT, producing a surplus of quasifree events from the PPT target frame.

which θ_n or θ_p is mismeasured by more than 15° is very likely to fail at least one other tight cut (besides θ_{open}), e.g., t_n vs θ_p . The yield that remains in these far wings (at a level $\lesssim 0.1\%$ of the peak height with the “optimal” dummy subtraction) is characterized by $C_{NN} \simeq 0$ (see Fig. 13), and may reflect a remnant of the qf events from the Kel-F frame. To allow for this possibility, we increase the effective dummy-target-thickness uncertainty from $\pm 4\%$ (suggested by the target construction) to $\pm 6\%$.

In summary, the C_{NN} analysis suggests that our initial expectation, $t_D/t_{\text{PPT}}=1.00$, is valid for the events that pass tight cuts, although with the uncertainty slightly enlarged (to $\pm 6\%$) to account for possible remaining effects of the apparent misalignment of the dummy and cold YES targets. To investigate whether the tight cuts remove free-scattering events with any undesirable spin-dependent bias, it remains useful to compare the final results with those deduced for loose cuts. For the latter sample, the above analysis suggests that we use $t_D/t_{\text{PPT}}=0.92$ to compensate for the target misalignment. For both tight and loose cuts, we also incorporate the slight difference expected from Monte Carlo calculations (see Sec. IV C 2) in the angular dependence of the proton detection efficiency between the two targets (which are unequal in proton energy loss). The calculated ratio of dummy-to-PPT proton efficiencies begins to deviate appreciably from unity for $\theta_p^{\text{lab}} > 50^\circ$ (reaching 1.06 for the last analyzed angle bin). However, at these angles the bound-nucleon background is relatively low, so that the net effect on the analysis is minor.

B. Beam and target asymmetries and polarizations

With the appropriate dummy normalization now determined, we obtain the final background-subtracted free-scattering yields, from which we extract the desired asymmetries $P_b A_n(\theta)$ and $P_t A_p(\theta)$ as a function of the deduced neutron bombarding energy \bar{E}_n^{inc} . The resulting asymmetries are plotted vs $\theta_{\text{c.m.}}$ for several \bar{E}_n^{inc} bins in Fig. 15. For each energy slice it is clear that the two asymmetries differ, to first order, simply by a normalization factor, presumably equal to $\rho \equiv P_t/P_b$. Because of the limited accuracy with which we can determine this polarization ratio by independent means [see Eq. (14)], our aim is to extract the subtle *shape differences* between $P_b A_n(\theta)$ and $P_t A_p(\theta)$.

It is also clear from Fig. 15 that both the shape of the analyzing power (e.g., the zero-crossing angle θ_0) and the normalization ratio ρ vary with bombarding energy. As explained further below, the *correlation* between these two variations makes it extremely important to analyze the data in relatively narrow \bar{E}_n^{inc} bins. Because our finite rf time resolution places a practical lower limit on the width of the energy bins we can consider, it is important to understand the energy dependence of both $A(\theta)$ and P_t/P_b quantitatively. We extract both pieces of information, and “ $\Delta A(\theta, \bar{E}_n^{\text{inc}})$ ” as well, from the measured asymmetries.

One could imagine extracting ρ (for a given energy slice) by taking the average over angles of the ratio $P_t A_p/P_b A_n$ formed by the measured asymmetries for

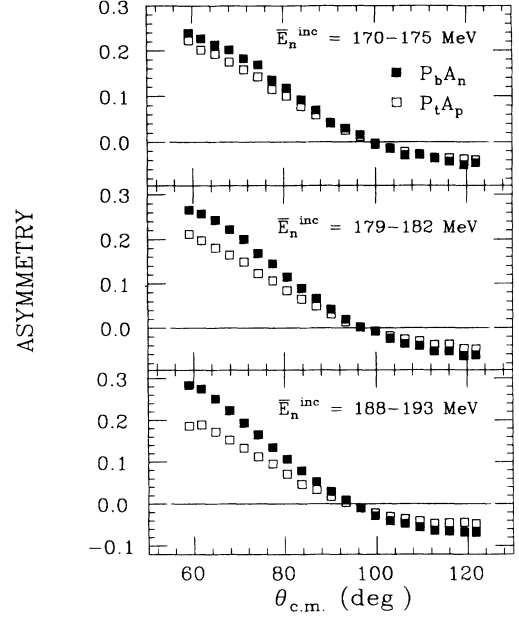


FIG. 15. Extracted beam ($P_b A_n$) and target ($P_t A_p$) analyzing power asymmetries for free \bar{n} - \bar{p} scattering as a function of the c.m. angle for three energy “slices” of the incident neutron beam. The statistical uncertainties are smaller than or equal to the size of the plotted points. One notes that the relative normalization (and at a more subtle level, the shape) of the beam and target asymmetries varies from slice to slice, requiring the analysis in narrow energy slices described in the text.

each angle bin. However, this procedure assumes that, when averaged over angle, A_n and A_p are equal, i.e., that $\langle \Delta A \rangle = 0$. There are a number of more sophisticated alternative procedures, which are based on less stringent assumptions about $\Delta A(\theta)$. One possibility is to fit the measured asymmetries with the analyzing power curve predicted (at the appropriate bombarding energy) by phase-shift solutions, multiplied by an adjustable polarization value and allowed to shift by a small adjustable angle offset. This procedure allows us to extract fitted values of P_b and P_t , as well as of the associated angle offsets $\delta\theta_b$ and $\delta\theta_t$, separately as functions of \bar{E}_n^{inc} . By allowing $\delta\theta_b$ to differ from $\delta\theta_t$, we allow for “ $\Delta A(\theta) \neq 0$ ”; specifically, we deduce ρ under the assumption that $\Delta A(\theta)$ is well approximated in shape by the angular derivative of $A(\theta)$. We have applied this procedure using Arndt SM89 phase shifts [19], and obtained fits of excellent quality [27] at all the energies analyzed.

The results we obtain by the above procedure for P_b and P_t and for the average zero-crossing angle (θ_0^{lab}) are shown as a function of bombarding energy in Fig. 16. Predicted values of θ_0 obtained from phase shifts and potential models are also shown in Fig. 16(b). Note that the extracted values of P_t are, as expected, essentially independent of \bar{E}_n^{inc} , while the deduced zero-crossing angle exhibits nearly the predicted slope. [The calculated *absolute* zero-crossing angle is quite sensitive to remaining phase-shift ambiguities; for example, the systematic offset $\sim 0.4^\circ$ lab of the data from the SM89 calculations seen in Fig. 16(b) becomes much smaller in magnitude and

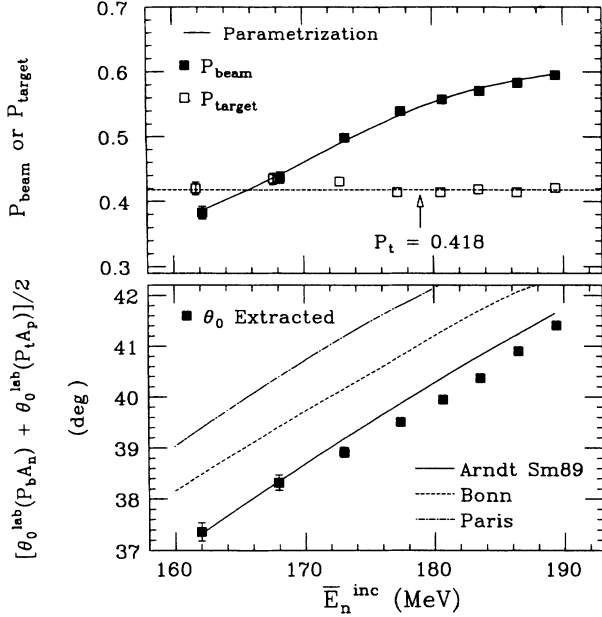


FIG. 16. Deduced beam (P_b) and target (P_t) polarizations (top panel) and average analyzing power zero-crossing angle (bottom panel) as a function of neutron bombarding energy \bar{E}_n^{inc} . The plotted points have been extracted by fitting the measured asymmetries within neutron beam energy “slices.” The error bars (smaller than the plotting symbols where not shown) reflect statistical fitting uncertainties. The curve through the P_b data is a fit with the empirical function of Eq. (18). The zero-crossing angle data in the lower panel are compared with the predictions of various NN potential models and a recent phase shift result.

changes sign when one uses Arndt’s SP88 or FA91 solutions [19] instead.] These observations support the assumptions underlying the analysis: neither the energy spectrum model (see Sec. III A 3) used to infer \bar{E}_n^{inc} from t_{rf} , nor the energy dependence of $A(\theta)$ predicted by the phase shifts [19], can be far from the truth.

In contrast to P_t , the deduced beam polarization varies rather strongly with \bar{E}_n^{inc} [28]. Some such dependence is expected [22] for the ${}^2\text{H}(\bar{p}, \bar{n})2p$ production reaction, arising primarily from the decreasing dominance of the 1S_0 state in the pp final-state interaction as the excitation energy within this system increases. This effect is reinforced by the decrease (predicted by phase shift calculations [19]) in the magnitude of the relevant p - n (quasifree) polarization transfer coefficient as the incident proton energy is degraded upon traversal of the LD_2 target. However, under the simplifying reaction model assumptions of Ref. [22], these effects account for only $\lesssim \frac{1}{3}$ of the variation observed in Fig. 16(a). For our subsequent analysis, we parametrize the observed dependence by the purely empirical function

$$P_b(E_n) = P_{b_{\min}} + \frac{P_{b_{\max}} - P_{b_{\min}}}{\{1 + \exp[(E_0 - E_n)/a_p]\}}, \quad (18)$$

represented by the solid curve in Fig. 16(a). Here, the adjustable parameters $P_{b_{\min}}$, $P_{b_{\max}}$, E_0 , and a_p have been op-

timized to fit the experimental P_b values when Eq. (18) is folded with our inferred E_n spectrum [see Fig. 5(c)], in order to average over the chosen \bar{E}_n^{inc} bins.

Independent results analogous to those presented in Fig. 16 can be extracted, albeit with poorer statistical precision, from the systematic error cycles in which the beam or target was kept *unpolarized*. Not surprisingly (since P_b and P_t were not perfectly stable in time), the absolute polarization values deduced for these test cycles differ by a few % from those for the standard \bar{n} - \bar{p} cycles. However, all of the results for the energy dependence of P_b and for the analyzing power zero-crossing angles are in excellent agreement. For example, if we sum the data over the six highest energy slices included in Fig. 16, the zero-crossing angle ($\theta_{0_p}^{\text{lab}}$) shifts (with respect to SM89 phase-shift calculations) obtained from the standard cycles are $\delta\theta_{0_b} = -0.419^\circ \pm 0.026^\circ$ and $\delta\theta_{0_t} = -0.198^\circ \pm 0.035^\circ$, where the errors are purely statistical. The corresponding values (with the same fitting functions) from the \bar{n} - p and n - \bar{p} test cycles, respectively, are $\delta\theta_{0_b} = -0.347^\circ \pm 0.114^\circ$ and $\delta\theta_{0_t} = -0.235^\circ \pm 0.086^\circ$. These results confirm that there is no appreciable contamination from spin correlation effects in the asymmetries measured with the beam and target simultaneously polarized.

The observed variation of P_b with \bar{E}_n^{inc} has significant consequences for our ΔA analysis. Because the beam asymmetry is weighted by P_b , within any bombarding energy bin of nonzero width $A_n(\theta)$ is measured at a somewhat higher effective mean energy than is $A_p(\theta)$. This energy difference necessitates a correction (described in Sec. VIF) to our ΔA results that is essentially proportional to the mean-squared width of the energy distribution contributing to each analyzed bin. Even for the relatively narrow bins considered in Fig. 16, this correction—included in the results presented below—is the largest one we must apply to the extracted ΔA values.

C. $\langle \Delta A \rangle_{\text{magic}}$

As discussed in Sec. IV D, our imprecise knowledge of the polarization ratio $\rho = P_t/P_b$ introduces an ambiguity proportional to the average analyzing power $A(\theta)$ in our extracted values of “ $\Delta A(\theta)$.” The clearest way to eliminate this ambiguity is to combine the ΔA results over “magic” angle ranges for which $A(\theta)$ averages to zero, and thus $\langle \Delta A \rangle_{\text{magic}} = \langle \Delta A_{\text{true}} \rangle_{\text{magic}}$. Since we in fact measured $A(\theta)$ to high precision in our experiment, we can determine appropriate ranges from the data themselves. One such range for which we report results below is $30.8^\circ \leq \theta_p^{\text{lab}} < 47.6^\circ$, corresponding to $82.2^\circ < \theta_{\text{c.m.}} \leq 116.1^\circ$. The average values of $A(\theta)$ over this range, extracted for the same energy slices as in Fig. 16, are shown as a function of \bar{E}_n^{inc} in Fig. 17, where the energy-dependence of $A(\theta)$ is again evident. For the energy range $170 \text{ MeV} \leq \bar{E}_n^{\text{inc}} \leq 193 \text{ MeV}$, encompassing the six highest bins in Fig. 17, the net (error-weighted) average value of A is $\langle A \rangle_{\text{magic}} = +(1.01 \pm 0.45) \times 10^{-3}$. We present ΔA results below only for this energy range, neglecting the two lower energy bins since they add little

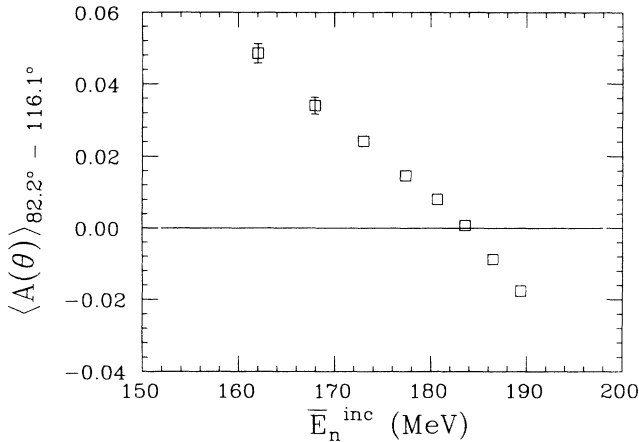


FIG. 17. The average value of the measured analyzing power ($[A_n(\theta) + A_p(\theta)]/2$) over the c.m. angle range 82.2° – 116.1° , as a function of neutron bombarding energy. The six highest energy bins were used in the extraction of the final $\langle \Delta A \rangle_{\text{magic}}$ result. While $\langle A(\theta) \rangle$ averages nearly to zero over this range, its energy dependence exhibited here contributes to the systematic error in the $\langle \Delta A \rangle$ result.

to the statistical precision of the ΔA result, while appreciably increasing the systematic error. The mean bombarding energy within this range is 182.2 MeV; the effective mean energy of the A_n measurement is several hundred keV higher, as a result of the energy dependence of P_b .

The results for $\langle \Delta A \rangle_{\text{magic}}$, both before and after the corrections (see Sec. VI F) for the variation of P_b within each energy slice, are shown in Fig. 18. Also shown are the final results for the entire energy range, obtained in

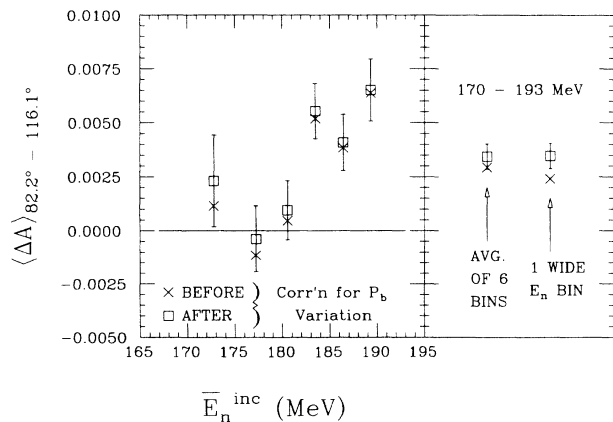


FIG. 18. Results for $\langle \Delta A(\theta) \rangle$ averaged over the “magic” angle range from 82.2° to 116.1° presented for different analysis procedures. In the left panel $\langle \Delta A \rangle_{\text{magic}}$ is plotted versus average neutron energy for six bins covering the range 170–193 MeV. The mean of these six results is compared in the right-hand panel to the value extracted from yields *summed* over one wide energy bin from 170 to 193 MeV. In both panels the results are presented before (\times ’s) and after (\square) a correction has been applied for the variation of P_b with energy within the neutron energy bin considered. The error bars represent only statistical uncertainties.

two different ways: (1) averaging the individual results for the six energy slices, with a weighting given by the fraction of the total analyzed yield falling within each slice; (2) analyzing the yields summed over a *single* wide energy bin from 170 to 193 MeV. The former method is preferred because the narrow energy bins require a substantially smaller average correction for the P_b variation than does the one wide bin. However, it is significant that *after* the corrections, the two approaches yield nearly identical results: $(+34.3 \pm 5.9) \times 10^{-4}$ for method (1) vs $(+34.6 \pm 5.9) \times 10^{-4}$ for method (2), where the errors quoted are purely statistical. (Two further small corrections for other systematic errors will be applied to the former value in Sec. VI to arrive at the central, final result of our experiment).

The value quoted above has been averaged over the four independent production runs taken. The corresponding values for the individual runs, given in Table II, are quite consistent within statistics: they yield a χ^2 per degree of freedom of 0.91 about their mean value.

Although it is expected theoretically (see Sec. VII A) that $\langle \Delta A \rangle$ should increase significantly with increasing bombarding energy within our range, the apparent dependence suggested by Fig. 18 cannot be taken too seriously. The experimental results appear systematically smaller for energy bins falling below the t_{rf} peak than above it. Unfortunately, just such a difference could be produced by an instrumental effect that we cannot rule out, namely, a very small systematic t_{rf} shift (≈ 1 ps) with spin state, leading to a spurious spin-dependence of the yields within *individual* \bar{E}_n^{inc} bins. Such a small timing error would, however, have negligible effects on the *energy-averaged* values presented on the right-hand side of Fig. 18.

The magic angle range we have chosen is not unique. It can, for example, be subdivided into two smaller magic ranges: an “inner” range (e.g., $88.4^\circ \leq \theta_{\text{c.m.}} \leq 106.3^\circ$) which includes the analyzing power zero crossing ($\theta_0 \approx 96^\circ$) and a disjoint “outer” range [$(82.2^\circ - 88.4^\circ) + (106.3^\circ - 116.1^\circ)$] with sections to either side of θ_0 . The results obtained for these ranges, each averaged over the six energy bins, are also included in Table II. The difference between them,

$$\langle \Delta A \rangle_{\text{outer}} - \langle \Delta A \rangle_{\text{inner}} = -(18.8 \pm 11.8) \times 10^{-4}$$

(again quoting only the statistical error for now), reveals a negative *curvature* of $\Delta A_{\text{true}}(\theta)$ in the vicinity of θ_0 , a characteristic that can be compared to theoretical predictions. We cannot extract meaningful information about the *slope* $[d(\Delta A)/d\theta]_{\theta_0}$ since we measure ΔA only to within a constant times $A(\theta)$ [see Eq. (15)], and $(dA/d\theta)_{\theta_0}$ is large. In principle, we could continue to subdivide the data into yet smaller “magic” angle ranges to obtain some information about yet higher derivatives of $\Delta A_{\text{true}}(\theta)$, but with progressively decreasing statistical precision. Rather, we turn our attention now to more “model dependent” means for comparing the full experimental and theoretical angular distributions.

TABLE II. Experimental results for ΔA averaged over “magic” angle ranges and over six bombarding energy bins covering the range $170 \leq \bar{E}_n^{\text{inc}} \leq 193$ MeV. They include, in each case, the correction for the variation of the beam polarization with energy within each bin; they do not yet include other small systematic error corrections described in Sec. VI. The errors quoted here are purely statistical. Because of the Gaussian rebinning prescription used to correct for multiple-scattering-induced angle shifts (see Sec. IV C 1), the statistical errors for $\langle \Delta A \rangle_{\text{inner}}$ and $\langle \Delta A \rangle_{\text{outer}}$ are not completely uncorrelated.

| Production run no. | $\langle \Delta A \rangle_{\text{inner}} \times 10^4$ ($88.4 \leq \theta_{\text{c.m.}} \leq 106.3^\circ$) | $\langle \Delta A \rangle_{\text{outer}} \times 10^4$ ($82.2 \leq \theta_{\text{c.m.}} \leq 88.4^\circ$) + ($106.3 \leq \theta_{\text{c.m.}} \leq 116.1^\circ$) | $\langle \Delta A \rangle_{\text{full}} \times 10^4$ [$82.2 \leq \theta_{\text{c.m.}} \leq 116.1^\circ$] |
|--------------------|--|---|---|
| 1 | 25.2 ± 22.9 | 2.5 ± 24.7 | 14.6 ± 16.8 |
| 2 | 38.2 ± 18.3 | 23.4 ± 19.7 | 31.2 ± 13.4 |
| 3 | 40.4 ± 14.1 | 21.6 ± 15.1 | 31.4 ± 10.4 |
| 4 | 55.0 ± 13.7 | 34.9 ± 14.6 | 45.4 ± 10.0 |
| Mean | 43.2 ± 8.1 | 24.4 ± 8.6 | 34.3 ± 5.9 |

D. Angular dependence of “ $\Delta A(\theta)$ ”

Our approach to comparing the measured and predicted angular dependences of $\Delta A(\theta)$ is to subject any theoretical calculation to precisely the same sort of ambiguity that arises unavoidably in the experimental results from possible errors in the beam and target polarization measurements. This is accomplished by constructing the quantity “ $\Delta A_{\text{theory}}(\theta)$ ” in Eq. (17), in analogy with Eq. (15). It is then critical that we follow *identical* procedures to optimize the constant c that appears in Eq. (15) and the corresponding quantity c_{theory} in Eq. (17). In this way we can extract directly comparable components of $\Delta A_{\text{true}}(\theta)$ from the experiment and the theory. The precise choice of criterion for optimizing c and c_{theory} is *not* critical: if we change the prescription we may slightly alter the appearance of both the resulting experimental and theoretical “ $\Delta A(\theta)$ ” curves, but we do not appreciably alter the comparison between them, e.g., as quantified by a χ^2 value (see Sec. VII B).

To extract the results presented in Fig. 19 we have chosen, in particular, to adjust c to *minimize the variance* ($\langle (\Delta A)^2 \rangle - \langle \Delta A \rangle^2$) of the “ ΔA ” data set over the c.m. angle range $68^\circ - 121^\circ$. (This range excludes the largest θ_p^{ab} bin included in Fig. 19, where ΔA is subject to the most serious systematic errors.) Our reasoning behind this choice of criterion is that, in the vicinity of the analyzing power zero-crossing angle θ_0 , the $A(\theta)$ ambiguity [Eq. (15)] is manifested primarily as a *slope* ambiguity in “ $\Delta A(\theta)$ ”; by minimizing the variance of “ $\Delta A(\theta)$,” we make its angular dependence as “flat” as possible, effectively imposing on the data a vanishing average slope over the fitting range. While this choice of slope is arbitrary, it happens (see Sec. VII B) to be very nearly equal to that predicted for our bombarding energy by various theoretical calculations.

We do not, of course, necessarily deduce the correct values of P_t/P_b or $\Delta A_{\text{true}}(\theta)$ by this technique. Rather, the minimum variance (mv) condition can be shown to select out that component of ΔA_{true} [obtainable by adding $cA(\theta)$] that is *uncorrelated* with $A(\theta)$, in the following sense:

$$(\langle \Delta A(\theta) \cdot A(\theta) \rangle)_{\text{mv}} = \langle \Delta A(\theta) \rangle_{\text{mv}} \langle A(\theta) \rangle, \quad (19)$$

where the averages are evaluated over the angular fitting range. The most significant features exhibited by the resulting data plotted in Fig. 19 are the clearly nonzero values of “ $\Delta A(\theta)$ ” over an extended range of angles and its appreciable downward curvature; these features persist *regardless* of the prescription used to extract “ ΔA .”

[For a meaningful comparison with theory, one should strictly minimize the variance of “ $\Delta A(\theta)$ ” only *after* possible angle-dependent systematic error corrections have been applied to the data. We have carefully evaluated such corrections as a function of angle for the yields *summed* over energy slices (see Sec. VI), but not for each individual slice. Consequently, the results presented in Fig. 19 are based on these summed yields and not (as for $\langle \Delta A \rangle_{\text{magic}}$) on an average of “ ΔA ” results for the narrower energy bins.]

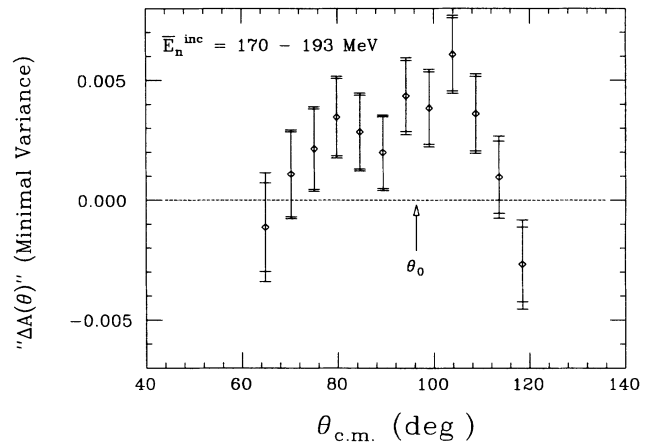


FIG. 19. Values of the CSB observable “ ΔA ” as a function of c.m. scattering angle, extracted by the “minimal variance” prescription described in the text. The data presented are extracted from the yields summed over the full 170–193-MeV neutron energy range. The extensions to the statistical error bars reflect the addition in quadrature of the systematic error calculated as a function of angle. The position of the zero crossing (θ_0) of the average n - p analyzing power is indicated by the arrow. The data provide clear evidence for charge-symmetry-breaking effects in “ $\Delta A(\theta)$.”

VI. SYSTEMATIC ERRORS

A. General considerations

In this experiment we have measured the CSB *difference* in shape between \bar{n} - \bar{p} scattering analyzing power asymmetries associated with the beam and with the target spin. Any instrumental problem that alters the angular dependence of one, *but not both*, of the measured asymmetries, or that affects the two asymmetries differently as a function of angle, can cause systematic errors in the deduced values of ΔA . Here we discuss such errors arising at various stages of the measurements and analysis, tabulating our quantitative error estimates in Tables III (for $\langle \Delta A \rangle_{\text{magic}}$) and IV [for “ $\Delta A(\theta)$ ”]. In Table IV, we omit the $cA(\theta)$ ambiguity [Eq. (15)] associated with errors in P_t/P_b , since this is already taken into account by comparing analogously deduced components “ $\Delta A(\theta)$ ” for theory and experiment.

The methods used to estimate each systematic error are described in Ref. [12] in more detail than here. Wherever possible, the error estimates are based on analysis of the \bar{n} - \bar{p} data themselves, with supporting evidence, where appropriate, from Monte-Carlo simulations and auxiliary measurements. We have attempted to identify independent sources of error, and to estimate a (conservative) “rms” value for each, in order that the various

contributions can be added in quadrature to deduce an overall systematic error for the experiment.

B. Background subtraction

Two types of background events are subtracted from the sample that survives all of the tight free-scattering cuts: the quasifree (qf) scattering background ($\sim 2.5\%$), measured independently with the dummy target; and accidental coincidences ($\sim 0.6\%$), monitored via events for which the detected neutron arrived one beam burst (57 ns) later than expected. The statistical uncertainties in these two background rates have already been incorporated into the ΔA statistical errors. There are, however, additional systematic uncertainties arising from imperfect subtraction in each case, because the background events have different effective values of ΔA than does free scattering. For example, the qf events have $P_t A_p^{\text{qf}} = 0$ since the *bound* target protons are unpolarized. If the corresponding neutron analyzing power $A_n^{\text{qf}}(\theta)$ were zero at all angles, then residual qf contributions to the analyzed yield would *not* introduce an appreciable systematic error. In fact, $A_n^{\text{qf}}(\theta)$, as measured with the dummy target, deviates from zero by as much as 0.1, as shown in Fig. 20.

The largest of the systematic background subtraction uncertainties is due to our imperfect knowledge of the

TABLE III. Systematic corrections and error estimates for $\langle \Delta A \rangle_{\text{full}}$ in units of 10^{-4} .

| Source of error | Correction applied | | Error estimate |
|--|--------------------|-------|----------------|
| 1. Background subtraction: | | | |
| (a) Dummy/PPT normalization ($\pm 6\%$) | 0.0 | \pm | 1.2 |
| (b) Dummy/PPT P_{beam} difference ($\pm 2\%$) | 0.0 | \pm | 0.4 |
| (c) Hydrogen contamination in dummy target | 0.0 | \pm | <0.1 |
| (d) Incomplete accidental coincidence subtraction | +0.4 | \pm | 0.7 |
| 2. Biased removal of free-scattering events: | | | |
| (a) Accidental coincidence with second random neutron | -1.6 | \pm | 1.6 |
| (b) Spin dependence of n -detector response | 0.0 | \pm | 0.5 |
| (c) Software cut dependence (e.g., multiple reactions in target) | 0.0 | \pm | 2.0 |
| 3. Incomplete “isolation” of $P_b A_n$ and $P_t A_p$: | | | |
| (a) Contamination of $T_{6,7}$ by other T_i | 0.0 | \pm | 0.5 |
| (b) In-plane spin correlations | 0.0 | \pm | 0.5 |
| 4. Instrumental beam and target asymmetries: | | | |
| (a) Spin-correlated beam motion | 0.0 | \pm | 0.3 |
| (b) Proton bending and neutron detector gain shifts associated with the PPT holding field | 0.0 | \pm | 0.7 |
| (c) “10-minute demons” | 0.0 | \pm | 0.3 |
| 5. Variations in P_t/P_b : | | | |
| (a) Physical correlation with E_n^{inc} | +5.0 | \pm | 2.0 |
| (b) Errors in E_n dependence correlated with $\langle A(\theta) \rangle_{\text{magic}}$ variations | 0.0 | \pm | 1.0 |
| (c) “Accidental” correlations with other parameter changes | 0.0 | \pm | 1.0 |
| (d) Effective angle dependence (spatial correlations) | 0.0 | \pm | 0.2 |
| 6. ΔA normalization uncertainties: | | | |
| (a) Absolute uncertainty in $P = (P_b \cdot P_t)^{1/2}$ ($\pm 5\%$) | 0.0 | \pm | 1.5 |
| (b) Error in relative flux normalization ($\pm 1\%$ per spin state) | 0.0 | \pm | 0.3 |
| Net correction | +3.8 | | |
| Net error | | \pm | 4.3 |

TABLE IV. Systematic corrections and error estimates and final experimental results for " $\Delta A(\theta)$," in units of 10^{-4} .

| | | | | | | | | | | | | |
|--|--|-----------------|-----------------|-----------------|-----------------|-----------------|-----------------|-----------------|-----------------|-----------------|-----------------|-----------------|
| Proton lab angle bin (deg) | 28.4– | 30.8– | 33.2– | 35.6– | 38.0– | 40.4– | 42.8– | 45.2– | 47.6– | 50.0– | 52.4– | 54.8– |
| Centroid c.m. angle (deg) | 30.8 | 33.2 | 35.6 | 38.0 | 40.4 | 42.8 | 45.2 | 47.6 | 50.0 | 52.4 | 54.8 | 58.0 |
| Dummy/PPT | 118.5 | 113.6 | 108.7 | 103.9 | 99.0 | 94.2 | 89.4 | 84.6 | 79.8 | 75.1 | 70.3 | 64.9 |
| thickness \times efficiency ratio assumed | 1.00 ± 0.05 | 1.00 ± 0.05 | 1.00 ± 0.05 | 1.00 ± 0.05 | 1.00 ± 0.05 | 1.00 ± 0.05 | 1.00 ± 0.05 | 1.00 ± 0.05 | 1.00 ± 0.05 | 1.01 ± 0.05 | 1.03 ± 0.05 | 1.06 ± 0.06 |
| Source of error | Correction applied \pm estimated error | | | | | | | | | | | |
| 1. Background subtraction | | | | | | | | | | | | |
| (a) Dummy/PPT normalization | 0.0 ± 1.8 | 0.0 ± 1.6 | 0.0 ± 1.6 | 0.0 ± 1.8 | 0.0 ± 1.2 | 0.0 ± 1.1 | 0.0 ± 1.1 | 0.0 ± 1.4 | 0.0 ± 1.8 | 0.0 ± 1.7 | 0.0 ± 1.7 | 0.0 ± 1.9 |
| (b) Dummy/PPT $P_b A_n^{gf}$ difference | 0.0 ± 0.6 | 0.0 ± 0.5 | 0.0 ± 0.5 | 0.0 ± 0.6 | 0.0 ± 0.4 | 0.0 ± 0.4 | 0.0 ± 0.4 | 0.0 ± 0.5 | 0.0 ± 0.6 | 0.0 ± 0.6 | 0.0 ± 0.6 | 0.0 ± 0.6 |
| (c) H contaminant in dummy target | 0.0 ± 0.1 | 0.0 ± 0.1 | 0.0 ± 0.1 | 0.0 ± 0.1 | 0.0 ± 0.1 | 0.0 ± 0.1 | 0.0 ± 0.1 | 0.0 ± 0.1 | 0.0 ± 0.1 | 0.0 ± 0.1 | 0.0 ± 0.1 | 0.0 ± 0.1 |
| (d) Incomplete accidental subtraction | +2.4 ± 1.2 | +2.4 ± 1.2 | +1.2 ± 1.2 | 0.0 ± 1.0 | 0.0 ± 0.9 | 0.0 ± 0.9 | 0.0 ± 0.9 | 0.0 ± 0.9 |
| 2. Biased removal of free-scattering events | | | | | | | | | | | | |
| (a) Accidental coincidence with 2nd n | -1.8 ± 1.8 | -1.8 ± 1.8 | -1.7 ± 1.7 | -1.6 ± 1.6 | -1.6 ± 1.6 | -1.5 ± 1.5 | -1.4 ± 1.4 | -1.3 ± 1.3 | -1.2 ± 1.2 | -1.0 ± 1.0 | -0.8 ± 0.8 | -0.7 ± 0.7 |
| (b) Spin dependence of n detector | 0.0 ± 1.5 | 0.0 ± 1.0 | 0.0 ± 0.5 | 0.0 ± 1.0 | 0.0 ± 1.5 |
| (c) Software cut dependence | 0.0 ± 9.0 | 0.0 ± 7.2 | 0.0 ± 4.6 | 0.0 ± 2.0 |
| 3. Incomplete "isolation" of $P_b A_n$ and $P_t A_p$ | | | | | | | | | | | | |
| (a) Contamination by other T_i | 0.0 ± 0.5 | 0.0 ± 0.5 | 0.0 ± 0.5 | 0.0 ± 0.5 | 0.0 ± 0.5 | 0.0 ± 0.5 | 0.0 ± 0.5 | 0.0 ± 0.5 | 0.0 ± 0.5 | 0.0 ± 0.5 | 0.0 ± 0.5 | 0.0 ± 0.5 |
| (b) In-plane spin correlations | 0.0 ± 0.5 | 0.0 ± 0.5 | 0.0 ± 0.5 | 0.0 ± 0.5 | 0.0 ± 0.5 | 0.0 ± 0.5 | 0.0 ± 0.5 | 0.0 ± 0.5 | 0.0 ± 0.5 | 0.0 ± 0.5 | 0.0 ± 0.4 | 0.0 ± 0.2 |
| 4. Instrumental beam and target asymmetries | | | | | | | | | | | | |
| (a) Spin-correlated beam motion | 0.0 ± 0.4 | 0.0 ± 0.3 | 0.0 ± 0.2 | 0.0 ± 0.2 |
| (b) PPT holding field effects | 0.0 ± 1.9 | 0.0 ± 1.3 | 0.0 ± 0.8 | 0.0 ± 0.8 | 0.0 ± 0.8 | 0.0 ± 0.7 | 0.0 ± 0.7 | 0.0 ± 0.8 | 0.0 ± 0.8 | 0.0 ± 0.8 | 0.0 ± 1.5 | 0.0 ± 4.6 |
| (c) "10-minute demons" | 0.0 ± 1.0 | 0.0 ± 1.0 | 0.0 ± 1.0 | 0.0 ± 1.0 | 0.0 ± 1.0 | 0.0 ± 1.0 | 0.0 ± 1.0 | 0.0 ± 1.0 | 0.0 ± 1.0 | 0.0 ± 1.0 | 0.0 ± 1.0 | 0.0 ± 1.0 |
| 5. Variations in P_t/P_b | | | | | | | | | | | | |
| (a) Variation with E_n^{inc} | +6.1 ± 2.3 | +7.2 ± 2.0 | +8.3 ± 2.1 | +9.4 ± 2.4 | +10.6 ± 2.7 | +11.7 ± 2.9 | +12.8 ± 3.2 | +14.0 ± 3.5 | +15.1 ± 3.8 | +13.4 ± 3.4 | +8.9 ± 3.2 | +3.6 ± 11.3 |

differences in $P_b A_n^{\text{qf}}$ between the two targets should be greatly magnified when we use the dummy data to subtract 93% of this sample. In fact, we find $\langle \Delta A \rangle_{\text{magic}}^{\text{fail}} = -0.013 \pm 0.019$ for the surviving residue. The (statistically insignificant) deviation of this result from the value (+0.003) we report for free scattering in this paper suggests a corresponding error of $-(0.31 \pm 0.37) \times 10^{-4}$ in $\langle \Delta A \rangle_{\text{magic}}$ evaluated for events that pass tight free-scattering cuts (where only 2.5% of the sample is subtracted). This inferred error is clearly consistent with that estimated above from the neutron beam polarimeter result, and both are statistically consistent with zero. We have thus made no correction for dummy vs PPT qf asymmetry differences in Tables III and IV, but have included uncertainties equivalent to those expected for a beam polarization ratio of 1.00 ± 0.02 .

Another potential problem with the qf subtraction arises from the presence of a small H contaminant in the dummy target (see Fig. 10). Our subtraction thus inadvertently removes a small contribution due to free scattering from unpolarized protons. The main effect of this subtraction is to make the PPT polarization appear larger than its true value by $\sim 1\%$. As long as this effective change of P_i is independent of angle, there is no resulting systematic error in $\langle \Delta A \rangle_{\text{magic}}$ or in “ $\Delta A(\theta)$,” whose extraction procedures have been designed specifically to circumvent our inadequate knowledge of the true polarizations. An angle-dependence can arise only at $\theta_p^{\text{lab}} \gtrsim 50^\circ$ (where we can no longer uniformly detect protons originating throughout the entire target thickness), if the depth distribution of the H in the dummy differs from that in YES. We have, for example, no clear way of distinguishing whether the contaminant H was spread uniformly throughout the volume (as for YES) or only on the surfaces of the dummy target. We therefore present final “ $\Delta A(\theta)$ ” results appropriate to the average of these two possibilities, via the corrections and errors 1(c) for the largest θ_p^{lab} bins in Table IV. These are based on comparing the standard results (which assume a uniform H contamination) with those obtained in an alternative analysis, where we subtracted the free-scattering yield from the dummy data by means of auxiliary measurements made with CH_2 sheets added to the upstream and downstream faces of the dummy target. [The latter subtraction was also used in extracting $A_n^{\text{qf}}(\theta)$ from the dummy data for Fig. 20.]

The subtraction of accidental coincidences is imperfect because our electronic timing inadvertently excluded some fraction of the “next-beam-burst” accidentals for a number of neutron-detector cells (see Sec. III E). The corresponding corrections and errors 1(d) in Tables III and IV are based [12] on estimates of the fraction of accidentals missed ($\sim 40\%$), combined with the *measured* values of ΔA for the accidental coincidences we do subtract.

C. Biased removal of free-scattering events

There are several possible mechanisms by which valid free-scattering events may be removed from our final

sample at a rate that changes with the beam and/or target spin orientation. One such mechanism results from the ambiguity in deciphering events for which two or more non-adjacent neutron-detector cells fire at nearly the same time. In particular, the algorithm used in the IUCF data analysis discards such events when the time difference between the two fires is less than 2 ns, and bases the neutron angle information on the *earlier* hit in other cases. As a result we lose or misidentify (and then discard with later cuts) $\sim 0.1\%$ of the valid free-scattering events, corresponding to cases where a second, uncorrelated neutron produced in the same beam burst fires a second cell on the same arm, anywhere from ~ 10 ns earlier to 2 ns later than the free-scattering neutron. The loss rate is thus tied to the singles rate of fast neutrons on the secondary arm, which has an appreciable nonzero effective value of ΔA (sizable A_n , small A_p).

The systematic correction and error [item 2(a) in Tables III and IV] due to these accidental coincidences with a second, random neutron has been estimated from the measured ΔA for two somewhat different samples of random neutrons (which do not normally cause event rejection): those that arrive more than 2 ns *later* than a valid free-scattering neutron and those that fire (at any time during the hardware coincidence acceptance) an unexpected liquid scintillator cell on the *primary* (proton) arm. There is very good agreement between the corrections determined from these two samples, each with an uncertainty of roughly half the size of the correction itself. Nonetheless, we have chosen to quote uncertainties equal in size to the average deduced corrections, because neither analyzed sample focuses precisely on the *fast* random neutrons that actually corrupt the analysis. The correction is angle dependent (see Table IV) because of the kinematic variation in the speed of the *free-scattered* neutron, and hence in the fraction of all neutrons from the same beam burst that might precede it to the liquid scintillator.

There are, of course, also free-scattering events in accidental coincidence with a second *charged* particle. However, these do *not* introduce a false asymmetry because the analysis algorithm discards such events *symmetrically* for extra wire chamber tracks on *either* the primary (p) or secondary (n) arm.

Spurious contributions to ΔA may also be introduced by the removal of events with software cuts, whenever there are spin-dependent mechanisms for populating the “wings” of the peak (or the kinematic locus) in the associated spectrum. For example, the “wings” remaining on the θ_{open} peak after dummy subtraction (see Fig. 13) comprise in part valid free-scattering events in which the neutron has been scattered twice (first from a carbon nucleus) within the liquid scintillator, without generating enough light to surpass the threshold in the original cell. Our tight cut on θ_{open} might then preferentially remove neutrons which have been scattered toward the left rather than the right (or vice versa) in their first interaction in the liquid. The survival rate of such misplaced events thus depends on \bar{n} -carbon analyzing powers and on the polarization of the free-scattered neutrons, which has different sensitivities to the beam and target spins. The

attendant systematic error [item 2(b) in Tables III and IV] has been estimated by investigating the dependence of the extracted $\langle \Delta A \rangle_{\text{magic}}$ and “ $\Delta A(\theta)$ ” results on the θ_{open} gate used (including some with quite asymmetric edges). We have observed *no* statistically significant changes in ΔA in this analysis. Our quoted errors thus represent only the statistical precision of the sensitivity determination in various angle regions, combined with estimates of the actual gate asymmetry introduced by the finite neutron cell size. The uncertainty grows considerably at the extreme angles (see Table IV), where the physical edges of the active neutron-detector volume effectively impose strongly asymmetric θ_{open} cuts.

More generally, we expect that free-scattering events which are preceded or followed by a second nuclear interaction of the neutron or proton, in either the target itself or surrounding material, will populate the “wings” of free-scattering distributions in several kinematic variables (in a correlated manner). We have investigated the influence of such multiple reaction processes, together with possible spin-dependent biases in the event sorting, by comparing the ΔA results obtained for six different sets of kinematic windows: all tight, all loose, and all tight except for one loose cut (on the beam spot, t_n vs θ_p , ΔE_p vs θ_p , or θ_{open}). In analyzing the data with all cuts loose, we assumed a dummy to PPT thickness ratio $t_D/t_{\text{PPT}}=0.92$ (to compensate for extra quasifree background events from the PPT target frame, see Sec. V A), while for all other combinations we used $t_D/t_{\text{PPT}}=1.00$. The errors 2(c) in Tables III and IV are estimated [12] from the rms deviations among these results, after allowance for statistical fluctuations expected because the different sets of cuts discard different numbers of free-scattering and background events. As one example of these comparisons, the $\langle \Delta A \rangle_{\text{magic}}$ results for all cuts tight and all cuts loose differ by 0.6×10^{-4} .

It is especially noteworthy that the $\langle \Delta A \rangle_{\text{magic}}$ results from the independent IUCF and University of Wisconsin data analyses differ by only 1.2×10^{-4} , well within the quoted uncertainty for dependence on the details of the software cuts, and also well within the expected statistical fluctuations associated with differences in event selection between the two analyses.

D. Extraction of $P_b A_n$ and $P_t A_p$

Even if we have successfully isolated the free-scattering events, there are possible errors in extracting the analyzing power asymmetries cleanly from the yields vs spin state. First, the desired quantities $T_{6,7}$ in Table I can have small contamination from other T_i to which the yields measured with simultaneously polarized beam and target are sensitive. For example, one can in fact extract only the *ratios* $T_{6,7}/T_1$, and T_1 differs from unity by small spin correlation terms (see Table I). Additional contamination may be introduced by deviations from perfect left-right symmetry in the detection setup—i.e., by efficiency differences for $n_L p_R$ vs $n_R p_L$ events—which have the effect of mixing each T_i with $T_{i\pm 4}$. The resulting contaminating terms in ΔA are all of second or higher order in small quantities: left-right efficiency

differences, up-down polarization differences, and horizontal polarization components. The errors [3(a) in Tables III and IV] introduced in ΔA are estimated to be $\lesssim 0.5 \times 10^{-4}$ via numerical simulations incorporating the values actually extracted from the data analysis for the other T_i and for the $n_L p_R/n_R p_L$ efficiency ratio. The values for ΔA extracted using several different formulas (see Sec. IV D) agree with one another to better than this estimated error, despite different sensitivities to the possible contaminating terms. [The final results presented here are based on Eqs. (11)–(13).]

An independent problem arises from those in-plane spin correlation (C_{LS}, C_{SL}) asymmetries that can contribute directly to $T_{6,7}$ (see Table I), i.e., which affect the measured yields in ways that are experimentally indistinguishable from those of $P_b A_n(\theta)$ or $P_t A_p(\theta)$. The problem is potentially serious because $\vec{n}\text{-}\vec{p}$ scattering phase-shift calculations [19] show that C_{LS} and C_{SL} are large in magnitude (up to ~ 0.5) for the bombarding energy and angular range of our experiment (in contrast to the situation at 477 MeV, see Ref. [11]). The corresponding asymmetries have been kept small by the procedures followed (see Secs. III A 2 and III B) to cancel horizontal components in the beam and target polarizations. In particular, we estimate [12] that the relevant components of \mathbf{P}_b have each been reduced to $\lesssim 0.01$ in magnitude by averaging data acquired with opposite polarities of the sweep/precession magnet through which the \vec{n} beam passed.

For the target polarization, our field measurements (see Sec. III B) suggest that horizontal components have been kept $\lesssim 0.002$ in magnitude. At this level of precision, it is important to keep in mind the distinction between *horizontal* and *in-plane* components, since the average scattering plane defined by the detectors may well deviate slightly from the horizontal (e.g., via an inadvertent systematic efficiency difference between cells above and below the centers of the neutron detectors). A tilt angle ϕ would introduce an effective sideways target component $P_S^{(t)} = P_N^{(t)} \sin\phi \simeq 0.4 \sin\phi$. From the free-scattering yields themselves, we find $|\langle \phi \rangle| \lesssim 0.2^\circ$ in each angular region covered, to allow for which we increase our upper limit on $P_S^{(t)}$ to ± 0.003 . (This same effect also contributes to $P_S^{(b)}$, but is small compared to the upper limits on beam polarization components discussed in the preceding paragraph.)

We now add in quadrature our estimated limits on the four individual in-plane spin correlation terms that appear in T_6 and T_7 , to arrive at our error estimate of 0.5×10^{-4} for $\langle \Delta A \rangle_{\text{magic}}$ [item 3(b) in Table III]. This estimate allows for $|C_{LS}| = |C_{SL}| = 0.5$; it is reduced for the largest θ_p^{lab} bins in Table IV in proportion to the angle dependence of C_{LS} expected from phase shift calculations.

Our scattering measurements provide strong supporting evidence for the small magnitude of these errors [12]. For example, over the angular range where $|C_{LS}|$ should be large, our $\vec{n}\text{-}\vec{p}$ data yield results statistically consistent with zero (see Fig. 21) for the quantity $T_8(\theta)$, which contains only in-plane spin correlation contributions (see

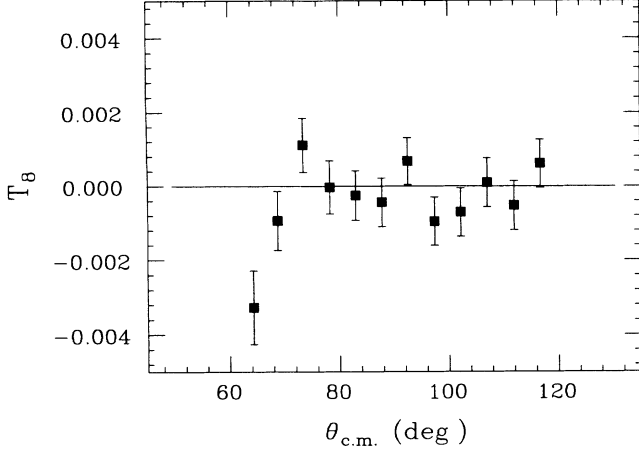


FIG. 21. The quantity “ T_8 ” (see Table I) measured for $\bar{n}\text{-}\bar{p}$ scattering as a function of c.m. angle. In the absence of systematic errors, nonzero values of T_8 arise solely from in-plane beam-target spin correlations. The corresponding spin-correlation coefficients are expected [19] to be largest within the c.m. angle range from 80° to 120° , where the measurements are statistically consistent with zero.

Table I). Indeed, $T_8(\theta)$ was consistent with zero even for auxiliary $\bar{p}\text{-}\bar{p}$ measurements with a *sideways-polarized* secondary proton beam, despite the large values of $P_S^{(b)}$ ($\simeq 0.6$) and C_{SL} (up to ~ 0.4 in magnitude) applicable in that case. From these $\bar{p}\text{-}\bar{p}$ data we extract the direct value $P_L^{(t)} = 0.0011 \pm 0.0050$.

As a further check, we can compare the results obtained from complementary *halves* of our $\bar{n}\text{-}\bar{p}$ data set. For example, the *difference* in $\langle \Delta A \rangle_{\text{magic}}$ results between the runs with positive and negative sweep magnet polarity (for which, individually, $\bar{P}_L^{(b)} \simeq +0.1$ or -0.1) is consistent with zero:

$$\langle \Delta A \rangle_{\text{magic}}^{+\text{sweep}} - \langle \Delta A \rangle_{\text{magic}}^{-\text{sweep}} = -(11.1 \pm 11.8) \times 10^{-4},$$

where the error is purely statistical. Thus, even with an artificially large in-plane neutron polarization, there is no measurable spin-correlation effect. Similarly, we can artificially “tilt” the scattering plane, and thereby introduce a sizable $P_S^{(t)}$, by analyzing only data from the upper half of the right-arm and lower half of the left-arm detectors (counterclockwise, or CCW, tilted plane, for which $P_S^{(t)} \simeq -0.05$), or vice versa (CW tilt, $P_S^{(t)} \simeq +0.05$). The difference in results for these two cases is again consistent with zero:

$$\langle \Delta A \rangle_{\text{magic}}^{\text{CCW tilt}} - \langle \Delta A \rangle_{\text{magic}}^{\text{CW tilt}} = +(10.0 \pm 12.4) \times 10^{-4}.$$

E. Instrumental beam and target asymmetries

Spurious contributions to $P_b A_n$ or $P_t A_p$ may arise from a number of instrumental sources. The most significant instrumental beam asymmetry is associated with a small expected (and observed) shift in the horizontal neutron beam intensity profile correlated with the primary proton beam spin orientation. This effect manifests the analyzing power ($A_{\text{prod}} \simeq 0.12$) of the production re-

action, which does not have a major influence because the vertical incident-proton-beam spin direction is generally contained within the vertical reaction plane. However, for neutrons directed toward the left or right edges of the PPT, the production reaction plane deviates slightly from the vertical, so that the proton beam acquires a small polarization component normal to the plane. The consequent spin-dependent slope of the neutron intensity distribution produces an observed (i.e., inferred from ray-tracing of the detected protons) centroid shift at the PPT of 0.041 ± 0.007 mm between the spin-up and spin-down \bar{n} beams. This result is consistent in both magnitude and direction with the expectation based on A_{prod} . Since the scattering angle is determined for each event from the proton ray tracing, independent of the event vertex location, the beam centroid shift does not introduce an angle error. It affects the detected yields [see item 4(a) in Tables III and IV] only via a small, spin-dependent change in the left-to-right solid angle ratio.

Instrumental *target* asymmetries can arise from flipping spin by reversal of the PPT holding field [item 4(b) in Tables III and IV], via either the bending of detected protons or induced gain (hence, efficiency) shifts in the neutron detector phototubes. In both cases, these asymmetries have been minimized by keeping the holding field strength low (0.059 T) and by averaging equal amounts of data acquired with the target spin parallel (NRM mode) and antiparallel (AFP mode) to the field. In addition, the proton bend angle ($< 0.5^\circ$ over the entire angle range covered) was corrected in software to an average accuracy of $\pm 0.01^\circ$, as monitored via the stability of the θ_{open} peak centroid with respect to field direction. Gain shifts were reduced by magnetic shielding of the phototubes, combined with compensation coils installed on the detector arms to offset residual effects of the (unclamped) holding field (see Sec. III D 1).

Even with these precautions, a substantial field-dependent difference remained between the results obtained separately for the NRM and AFP modes:

$$\langle \Delta A \rangle_{\text{magic}}^{\text{NRM}} - \langle \Delta A \rangle_{\text{magic}}^{\text{AFP}} = +(55.1 \pm 11.8) \times 10^{-4}.$$

The factor by which this difference is suppressed when the NRM and AFP yields are summed has been estimated to be > 80 , by observing the change in final $\langle \Delta A \rangle$ values when the software angle correction for the bending of the protons was purposely miscalibrated (introducing artificial NRM-AFP differences much larger than that above). We thus divided the observed NRM-AFP differences by 80 to deduce the overall field-dependent systematic errors in Tables III and IV. No more than about 0.4×10^{-4} of the estimated error 4(b) for each angle bin can be attributed specifically to gain shifts, judging from the pulse heights recorded in the liquid scintillator for free-scattering protons as a function of the PPT field orientation.

Because the target spin-flip period (20 min) was relatively long, $P_t A_p$ is also susceptible to spurious contributions caused by short-term drifts in beam or detector properties, or electronics, that happened to occur for only one PPT spin orientation and to affect left and right scattering differently. We refer to such drifts as “10-

minute demons” [item 4(c) in Tables III and IV]. In order to avoid such problems we monitored, throughout the data replay, the consistency from run to run in the left/right yield ratios for the four beam-target spin combinations and for five different angle bins. We omitted from the final analysis two (out of ~ 1300) \bar{n} - \bar{p} runs for which more than one of these 20 ratios changed by greater than three statistical standard deviations from the values in neighboring runs. For all of the runs retained in the final data sample, the fluctuations observed in these yield ratios were completely consistent with counting statistics. For any of the five angle bins, our statistical analysis of the ratios should have revealed even a *single* anomalous 10-min period during the experiment, if it had been characterized by an instrumental left/right efficiency change as large as $\pm 5\%$. (The threshold for detecting such variations would be even smaller, per occurrence, if there were *more* than one anomalous period.) The quoted errors 4(c) have been based on this statistical analysis.

F. Variations in P_t/P_b

In extracting ΔA from the measured asymmetries $P_b A_n(\theta)$ and $P_t A_p(\theta)$, we have assumed that the polarization ratio $\rho \equiv P_t/P_b$ is a *constant*, independent of angle. Any mechanism that causes ρ effectively to vary with angle will then introduce a systematic error in the results. For this purpose, it is sufficient if ρ and the shape of the analyzing power angular distribution undergo correlated changes as a function of some third parameter, such as beam energy.

1. Effects of the finite beam energy spread

The most serious of these ρ - $A(\theta)$ correlations, associated with the variation of P_b over the finite neutron beam energy spread, was discussed in the context of Fig. 16. Although the effect of this correlation was reduced by extracting $\langle \Delta A \rangle_{\text{magic}}$ for a number of relatively narrow beam energy bins, the remaining width (~ 3 – 4 MeV) of the bins necessitated appreciable corrections to the results obtained. The false asymmetry for which we correct is given to first order by

$$\Delta A_{\text{false}}(\theta, \bar{E}_n^{\text{inc}}) = \left[\frac{\partial A_n(\theta, E_n)}{\partial E_n} \right]_{E_n = \bar{E}_n^{\text{inc}}} \left[\frac{\langle P_b E_n \rangle}{\langle P_b \rangle} - \bar{E}_n^{\text{inc}} \right], \quad (20)$$

where the angular brackets denote averaging over the actual energy distribution contributing to the analyzed bin, and $\bar{E}_n^{\text{inc}} \equiv \langle E_n \rangle$. The second term in square brackets in Eq. (20) represents the effective energy difference between the $A_n(\theta)$ and $A_p(\theta)$ measurements. The corrections applied have been based on the data themselves to the greatest extent possible. Thus, the distribution of neutron energies contributing to each analyzed slice was taken from the model that we *fit* to our observed t_{rf} spectra (see Fig. 5 and Sec. III A 3). The energy dependences of both P_b and $A_n(\theta)$ were deduced from fits to the measured $P_b A_n$ asymmetries (see Fig. 16 and Sec. V B), with $P_b(E_n)$ represented by the empirical function of Eq. (18).

The corrections determined via Eq. (20) are shown for $\langle \Delta A \rangle_{\text{magic}}$ in Fig. 18. They vary from $+1.4 \times 10^{-4}$ for the highest energy slice considered to $+11.6 \times 10^{-4}$ for the lowest. This rapid change in the correction is due in part to the increasing slope of $P_b(E_n)$ and in part to an increase in $\delta E_n / \delta t_{\text{rf}}$ (hence, in the width of the contributing energy distribution) as \bar{E}_n^{inc} decreases. The correction to the $\langle \Delta A \rangle_{\text{magic}}$ result *averaged* over energy bins is $+5.0 \times 10^{-4}$. This is to be compared with a correction of $+10.7 \times 10^{-4}$ calculated for the case where we analyzed the very same data for one *wide* (170–193 MeV) energy bin, instead of six narrow bins (see the right-hand side of Fig. 18). Despite the larger correction needed in the one-bin approach, we have used it (for reasons discussed in Sec. V D) to extract “ $\Delta A(\theta)$,” with the resulting corrections shown in item 5(a), Table IV.

The uncertainty in the size of these corrections for the energy dependence of P_b contributes significantly to our overall systematic error. The dominant uncertainty stems from ambiguities in the neutron energy spectrum model (Sec. III A 3), specifically, the model dependence of the variances (σ_E^2) deduced for the energy distributions contributing to each analyzed bin. For the narrow energy bins especially, σ_E^2 is strongly influenced by the rf time resolution inferred from the fits to the t_{rf} spectra. This time resolution is, in turn, strongly correlated with another adjusted parameter, namely, the decay constant of the assumed exponential falloff in the ${}^2\text{H}(p, n)$ cross section with increasing excitation energy (E_{2p}^*) of the recoiling $2p$ system. The optimal fits were obtained with very reasonable parameter values: 6.6 MeV for the decay constant, in excellent agreement with the value (6.7 MeV) expected for our conditions from the ${}^2\text{H}(p, n)$ reaction calculations of Bugg and Wilkin [22], and 0.64 ns FWHM for the t_{rf} resolution, averaged over all the data. However, we were able to maintain adequate fits to the spectra by varying the decay constant or other important assumptions of the model (e.g., adding a flat-topped portion to the E_{2p}^* dependence), and adjusting the t_{rf} resolution parameter by up to $\pm 20\%$ to compensate. The resulting uncertainty introduced in Eq. (20) is $\pm 35\%$ of the correction for $\langle \Delta A \rangle_{\text{magic}}$, where the preferred analysis has been carried out for the narrow energy slices. It is reduced in relative (but not absolute) size to $\pm 20\%$ of the correction for “ $\Delta A(\theta)$,” because σ_E^2 for the single wide energy bin is influenced relatively less by the uncertain rf time resolution.

The remaining contribution to the errors 5(a) in Tables III and IV, summed in quadrature with the energy spectrum uncertainty discussed above, is associated with the energy derivatives of $A_n(\theta)$ and of P_b . Errors in these two derivatives are strongly anticorrelated with one another, because we extract both from fits to the same $P_b A_n(\theta)$ asymmetries as a function of \bar{E}_n^{inc} (see Fig. 16). Furthermore, the net error in the product of the two derivatives is constrained [12] to $\pm 15\%$ of the correction by the excellent agreement obtained (see Fig. 18) between the corrected $\langle \Delta A \rangle_{\text{magic}}$ results for one wide versus six narrow energy slices. We have also analyzed “ $\Delta A(\theta)$ ” in both narrow and wide slices, and [despite ambiguities in

minimizing the variance of “ $\Delta A(\theta)$ ” within each narrow slice, see Sec. VD] the results agree within the expected net systematic errors for all but the extreme angle bins. For the latter bins we have therefore replaced the normal error estimate in Table IV ($\pm 25\%$ of the wide-slice correction) by half the observed difference between these two alternative analyses.

For the analysis in narrow energy slices, another effect of the ρ - $A(\theta)$ correlation is connected with the observation (see Fig. 17) that there is no single angle range that is “magic” (i.e., for which $\langle A(\theta) \rangle$ vanishes) for *all* of the slices; this gives rise to error 5(b) in Table III. Strictly, when we average $\langle \Delta A \rangle$ results over energy slices, we obtain:

$$\langle \Delta A \rangle_{\text{magic}} = \frac{\sum_i Y_i [\langle \Delta A_i \rangle_{\text{magic}} + (\delta\rho_i/\rho_i) \langle A_i \rangle_{\text{magic}}]}{\sum_i Y_i}, \quad (21)$$

where Y_i represents the total free-scattering yield, integrated over the magic angle range, included in the i th energy bin [29]. We have allowed in Eq. (21) for the systematic error arising [via Eq. (14)] from an error ($\delta\rho_i$) in ρ_i for each energy bin. The individual analyzing power averages $\langle A_i \rangle_{\text{magic}}$ vary systematically with energy, as shown in Fig. 17, in such a way that their average over the full energy range vanishes (this was the criterion for choosing the “magic” angle range). Thus, random errors in the ρ_i tend to cancel in the summation in Eq. (21). However, an overall systematic error in $\langle \Delta A \rangle_{\text{magic}}$ can arise if we overestimate or underestimate the *slope* of P_b (and hence of ρ) with respect to beam energy, since then the $\delta\rho_i$ will be *correlated* with the $\langle A_i \rangle_{\text{magic}}$ values. In estimating this error we allow for a $\pm 20\%$ uncertainty in $d\rho/dE_n$. This is twice as large as the widest variation we have observed by using different prescriptions for extracting $\rho(E_n)$ from the measured asymmetries and different analytical functions to fit the $P_b(E_n)$ values. There is no corresponding error in Table IV because the problem vanishes for any single energy bin for which $\langle A \rangle_{\text{magic}} = 0$, as was used in the “ $\Delta A(\theta)$ ” analysis.

2. Other sources of polarization variation

The correlation between ρ and $A(\theta)$ discussed above is inherent in the *physics* of the production reaction and of n - p scattering, and was unavoidable in our experiment. There may also, however, be “accidental” correlations that occur, for example, if P_b and/or P_t change with time during the experiment, and so does another parameter (proton energy out of the cyclotron, LD₂ target thickness, etc.) that affects the measured angular distributions. If one were simply to sum the yields over all times, then one would average such different conditions with different weighting in $P_b A_n$ and $P_t A_p$. As an illustration, suppose that half the data were acquired with certain values of P_b , P_t and the centroid neutron beam energy \bar{E}_n^{inc} , while the other half had \bar{E}_n^{inc} 1 MeV higher, P_b increased by a factor of 1.10, and P_t reduced by a factor of 0.95. (Changes

of this order were actually observed during the experiment.) Summing the yields over these two halves would then introduce an effective energy difference of 37 keV between the A_n and A_p measurements and a consequent $\langle \Delta A \rangle_{\text{magic}}$ error $\sim 1 \times 10^{-4}$. In principle, a more correct procedure is to determine P_t/P_b and to extract ΔA independently from many small time segments, and then to average the ΔA results. In practice, the need for sufficient statistical precision to perform a meaningful optimization [e.g., by “ $\Delta A(\theta)$ ” variance minimization] of P_t/P_b for each time interval limits the number of segments into which the full data set can be usefully decomposed.

We have extracted $\langle \Delta A \rangle_{\text{magic}}$ and “ $\Delta A(\theta)$ ” independently for each of the four production runs, and then averaged the results to arrive at the final values we report here. Although the individual results are statistically consistent with one another (see Table II), their averages differ slightly (typically by $\sim 1 \times 10^{-4}$, consistent with the above example) from the corresponding results obtained from the yields summed over all production runs. In Tables III and IV [item 5(c)], we have taken these differences to be indicative of possible remaining systematic errors from “accidental correlations” *within* each production run. (In fact, there were more substantial systematic changes in P_b from one production run to another than there were for P_b or P_t *during* any one of the production runs.)

Finally, an effective variation of ρ with angle may result from *spatial* variations of P_b and/or P_t . The problem arises because the yields at large proton angles comprise nonuniform contributions from different parts of the target volume: protons with sufficient energy to penetrate all four wire chambers are relatively unlikely to have been generated in free n - p scattering events occurring near the upstream face of the YES target or near the Kel-F target frame edge closest to the proton detection arm. The distribution of detected n - p pairs as a function of event origin within the target volume has been calculated for each proton angle bin in our Monte Carlo simulations. For example, effectively only the downstream half of the target thickness contributes to our observed yields for $\theta_p^{\text{lab}} \simeq 56^\circ$. To deduce limits on the effective angle dependence of ρ , we have combined [12] these Monte Carlo results with measured limits (from the \bar{n} - \bar{p} data themselves) on the x_{tgt} dependence of $P_t A_p / P_b A_n$, and with estimated limits on the z_{tgt} dependence of P_t across the 0.6 cm YES thickness. The resulting systematic errors in ΔA [item 5(d) in Tables III and IV] are then of the form $A(\theta)[\rho(\theta) - \bar{\rho}]/\bar{\rho}$, where $\rho(\theta)$ represents an angular variation at our estimated limit about an average polarization ratio $\bar{\rho}$.

The error estimates 5(d) allow, in particular, for a quadratic variation $\rho(x_{\text{tgt}})$ characterized by a 10% change from the center of the target to the edges of the region included within our beam spot cut. The $P_b A_n$ and $P_t A_p$ values extracted as a function of x_{tgt} from the \bar{n} - \bar{p} data for $25^\circ \leq \theta_p^{\text{lab}} \leq 40^\circ$ (where the ray-tracing resolution is best) indicate that the actual ρ variation is smaller than this level with 95% confidence. The same data place a

limit of 2% (from one target edge to the other) on any *linear* variation in ρ . The resulting errors are small because the angle dependence of the simulated x_{tgt} yield profile is weak.

The sensitivity to any change of ρ with z_{tgt} is much greater. In estimating limits on the z_{tgt} dependence of P_t , we have noted that any appreciable *linear* variation (e.g., as might arise from spatial variations in crystal impurities) would produce a difference between the ΔA results obtained with 0° vs 180° orientation of the crystals. However, no such difference is observed; e.g.,

$$\langle \Delta A \rangle_{\text{magic}}^{0^\circ} - \langle \Delta A \rangle_{\text{magic}}^{180^\circ} = +(5.8 \pm 11.8) \times 10^{-4}.$$

On the other hand, the 0° – 180° comparison would be unaffected, while ρ could acquire an appreciable angle dependence, if P_t varied with z_{tgt} *symmetrically* about the target center. Examples of conceivable mechanisms for such a dependence are surface depolarization in the YES crystals or a quadratic variation of Yb doping concentration that might have developed during the slow crystal growing process. The resulting P_t variations would still be severely limited in extent by the spin-diffusion process [20] that leads to sharing of the polarization among protons near to and far from Yb doping sites. Our error estimates 5(d) allow, in particular, for P_t to be 2% larger or smaller near the target faces than at the target center. The corresponding error contributions are nearly equal in value to the independent errors considered earlier [item 1(c), Sec. VI B] to account for possible hydrogen contamination of the dummy target surfaces: such a contamination would introduce (via dummy subtraction) an *effective* symmetric z_{tgt} dependence of P_t (also of amplitude $\simeq 2\%$ if half of the hydrogen observed in the dummy target were concentrated on the surfaces). The largest θ_p^{lab} bin included in Table IV has been chosen to straddle 56° specifically to keep errors 1(c) and 5(d) small; the error caused by a symmetric variation $P_t(z_{\text{tgt}})$ would vanish if exactly half of the target thickness contributed (uniformly) to the observed yields.

G. ΔA normalization uncertainties

Finally, there are measurement uncertainties that affect only the overall normalization of the ΔA results obtained. We have included these in Table III among the errors in the absolute value of $\langle \Delta A \rangle_{\text{magic}}$, but not in Table IV, since the angular dependence of “ $\Delta A(\theta)$ ” is unaffected.

As seen from Eq. (14), the most important normalization error arises from the uncertainty δP in the mean polarization $P \equiv (P_b P_t)^{1/2}$. The absolute values used for the polarizations depend upon phase shift calculations [19] of the n - p scattering analyzing powers, which have been used in fitting the measured asymmetries. The normalization of the phase shift calculations is best constrained by earlier medium-energy (≥ 220 MeV) n - \bar{p} measurements, utilizing either a polarized proton beam to initiate quasifree scattering on deuterium [30] or a polarized proton target [31]. The two independent absolute polarization calibration techniques used in these experiments, each with a claimed accuracy of $\sim \pm 3\%$, gave consistent

results: the value of P we extract from our asymmetry fits changed by $< 2\%$ with the recent inclusion of the results of Ref. [31] in the Arndt [19] database. In order to allow for small systematic errors in the phase-shift extrapolation down to the vicinity of 183 MeV, we assign a scale uncertainty of $\pm 4\%$ to the phase-shift calculation of $A(\theta)$. In addition, we can alter P by up to 3% of its value by changing the angle range over which the fits are made. Thus, we estimate an overall error of $\pm 5\%$ in the values used for P , and hence in $\langle \Delta A \rangle_{\text{magic}}$ [item 6(a), Table III]. Independent NMR measurements we made of the PPT polarization three times per cycle were consistent with, but less reproducible ($\sim \pm 10\%$) than, the values deduced from the scattering asymmetries.

An independent normalization uncertainty can result [24] from errors in the relative (for different beam-target spin combinations) neutron flux and dead-time determinations [see Eqs. (11) and (12)]. Our neutron flux measurements, made with an in-beam scintillator, generally agreed within $\pm 0.5\%$ with the relative primary proton fluxes determined by charge integration in a Faraday cup. Similarly, live-time determinations made by independent techniques (scalers gated by the electronic busy signal versus the analyzed fraction of optical pulser events) also agreed to within $\pm 0.5\%$ and scaled with the beam intensity in the expected way. In item 6(b), Table III, we have allowed for a $\pm 1\%$ uncertainty per spin state in the dead-time corrected neutron flux, which then causes a $\pm 1\%$ uncertainty in the extracted ΔA values.

H. Summary

We have summed in quadrature a large number of independent contributions to obtain the net systematic error in our measurements. As seen in Tables III and IV, there are typically several contributions of comparable magnitude. One would thus have to reduce sensitivities to a number of effects simultaneously in order to improve appreciably upon the present systematic error bars.

The net systematic error we quote for $\langle \Delta A \rangle_{\text{magic}}$ is $\pm 4.3 \times 10^{-4}$. A number of the most important contributions in Table III—namely, items 1(a), 1(b), 2(a), 5(a), and 5(d)—tend to yield strongly correlated effects at different angles within the magic range. Thus, the systematic error in the *difference* $\langle \Delta A \rangle_{\text{outer}} - \langle \Delta A \rangle_{\text{inner}}$, introduced in Sec. V C to provide sensitivity to the curvature of $\Delta A(\theta)$, is considerably smaller than $\sqrt{2}$ times the result of Table III. Taking these correlations into account, and applying the normalization uncertainties 6(a) and 6(b) only to the measured *difference*, we estimate the net systematic error in $(\langle \Delta A \rangle_{\text{outer}} - \langle \Delta A \rangle_{\text{inner}})$ to be $\pm 4.9 \times 10^{-4}$. Similarly, there are correlations between different angle bins in the errors quoted in Table IV, but these are considerably smaller than the *statistical* uncertainties for each individual bin.

VII. COMPARISON TO THEORY

A. $\langle \Delta A \rangle_{\text{magic}}$

Our final results for average values of ΔA over magic angle ranges, incorporating the corrections and systemat-

ic errors described in Sec. VI are

$$\langle \Delta A \rangle_{82.2^\circ-116.1^\circ} = (33.1 \pm 5.9 \pm 4.3) \times 10^{-4}, \quad (22)$$

$$\langle \Delta A \rangle_{\text{outer}} - \langle \Delta A \rangle_{\text{inner}} = -(17.8 \pm 11.8 \pm 4.9) \times 10^{-4}, \quad (23)$$

where in both cases the first error specified is statistical and the second is systematic. These results are compared with theoretical predictions, averaged over precisely the same angle ranges as the data, in Figs. 22 and 23 and in Table V. In Fig. 22, we also compare predictions with the earlier TRIUMF result [11] for $\Delta A(\theta_0=71^\circ)$ in 477 MeV n - p scattering.

Theoretical calculations of CSB in n - p scattering have been reported by a number of groups [13–18]. Although it is presumed that the strong-interaction violations arise fundamentally at the quark level, most practical calculations are based on meson-exchange models of the NN interaction. The various calculations agree that, for the energy range of the present experiment, nonzero values of ΔA arise mainly from three exchange mechanisms: the purely electromagnetic (γ -exchange) spin-orbit interaction between the neutron magnetic moment and the proton current; the effect of the n - p mass difference on isovector meson (π, ρ) exchange; and isospin mixing of the ρ^0 and ω^0 mesons [32]. Each of these effects gives rise to an n - p potential (e.g., see Ref. [16]) that depends in a non-symmetric way on the neutron and proton spins.

Since the CSB potential terms are all rather weak, predictions for $\Delta A(\theta)$ can be obtained in the distorted-wave Born approximation. The usual approach is to calculate the CSB “mixing parameters” γ_J (Ref. [13]), which couple the 1J_J and 3J_J waves, using distorted waves generat-

ed with conventional NN potentials. In the calculations shown in Fig. 22, γ_J values predicted [15] with the Bonn NN potential have been combined with isospin-conserving phase shifts (the SM89 set of Ref. [19]) to generate $\Delta A(\theta)$. Analogous calculations, with distortions generated [16] by the Paris and Reid soft-core potentials, are included in Table V. In all these cases, we have re-scaled the ρ - ω mixing contributions to reflect the most recent value [4] of the mixing matrix element determined from $e^+e^- \rightarrow \pi^+\pi^-$ excitation functions [3]; Refs. [15] and [16] had used an older, smaller value for this matrix element.

Several conclusions can be drawn from the comparison of theory and experiment in Fig. 22. The most striking is that the present $\langle \Delta A \rangle$ result is clearly incompatible with the assumption that the strong interaction exactly preserves charge symmetry. If we combine statistical and systematic errors in quadrature, our result differs by 3.4 standard deviations from the prediction based on γ exchange alone. This conclusion is little affected by theoretical ambiguities: as seen in Table V, distortion uncertainties cause only about $\pm 1 \times 10^{-4}$ spread in calculated $\langle \Delta A_\gamma \rangle$ values.

Furthermore, our result provides substantial evidence (at about the 2 standard deviation level) for CSB effects beyond those due to the n - p mass difference. Again (see Table V), this observation persists regardless of distorting potential, although the theoretical uncertainty ($\sim \pm 3 \times 10^{-4}$ in $\langle \Delta A_{\gamma+\pi+\rho} \rangle$) is now significant. The remaining violation observed at 183 MeV appears to be well accounted for by ρ - ω mixing. This substantial sensitivity to the ρ - ω mixing contribution at 183 MeV is to be contrasted with the situation at 477 MeV (see Fig. 22), where the predicted $\Delta A_{\rho\omega}(\theta)$ happens to cross zero very near the single angle at which the measurement was performed [11]. Measurements at 477 MeV over a broader angle range would not have improved this sensitivity much: the calculations suggest that at that energy $\Delta A_{\rho\omega}(\theta)$ strongly resembles $A(\theta)$ in shape, and thus falls

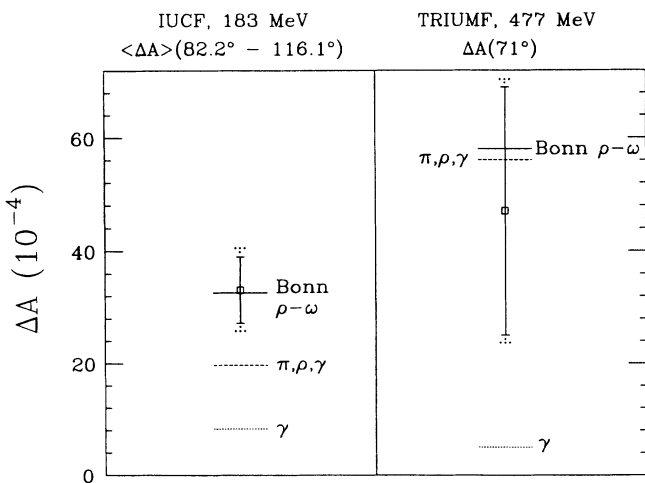


FIG. 22. Measured and calculated values of the charge-symmetry-breaking observable ΔA for n - p scattering at $E_n=183$ MeV (present result) and $E_n=477$ MeV [11]. The solid error bars are purely statistical, while the dotted extensions indicate the effect of adding systematic errors in quadrature. The solid and broken horizontal lines represent theoretical predictions based [15] on the Bonn NN potential for various contributing diagrams, as described in the text.

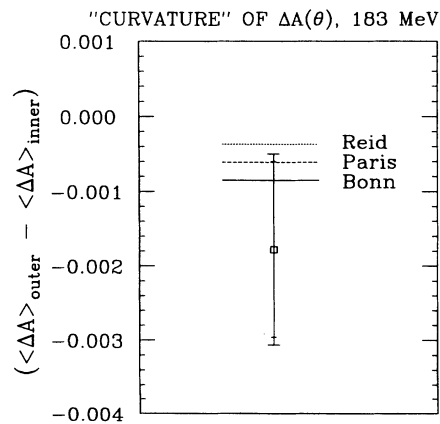


FIG. 23. Comparison of measured and predicted “curvatures” of $\Delta A(\theta)$, as defined by the difference between the average values of $\Delta A(\theta)$ over “outer” and “inner” “magic” angle ranges. The solid and broken horizontal lines represent calculations based on three different NN distorting potentials.

TABLE V. Theoretical predictions^a for ΔA at 183 MeV averaged over the “magic” angle range $82.2^\circ \leq \theta_{c.m.} \leq 116.1^\circ$.

| Distorting potential | Theoretical input | | Ref. | Predictions ($\times 10^4$) | | | | |
|----------------------|-------------------------|---------------------------|------|-------------------------------------|----------------------------------|-----------------------------------|---|------------------------------|
| | $\frac{g_\rho^2}{4\pi}$ | $\frac{g_\omega^2}{4\pi}$ | | $\langle \Delta A_\gamma \rangle^b$ | $\langle \Delta A_\pi \rangle^c$ | $\langle \Delta A_\rho \rangle^d$ | $\langle \Delta A_{\rho\omega} \rangle^e$ | $\langle \Delta A \rangle^f$ |
| Bonn | 0.77 ^g | 23 ^g | [15] | 8.3 | 9.8 | 1.6 | 12.9 | 32.6 |
| Paris | 0.55 ^h | 8.1 ^h | [16] | 9.4 | 11.8 | 1.6 | 8.0 | 30.8 |
| Reid soft-core | 0.55 ^h | 8.1 ^h | [16] | 7.4 | 8.6 | 1.0 | 5.0 | 22.0 |

^aThe predictions are based on phase-shift calculations incorporating the SM89 isospin-conserving phases of Ref. [19] and the isospin-mixing parameters calculated in the references indicated.

^bThe contribution from the electromagnetic spin-orbit interaction.

^cThe contribution from the one-pion exchange potential term arising from the n - p mass difference.

^dThe contribution from the single ρ -exchange potential term arising from the n - p mass difference.

^eThe contribution from ρ^0 - ω^0 mixing, rescaled from the original calculation to conform with the current best value (-4520 MeV² from Ref. [4]) for the mixing matrix element $2m_\rho \langle \rho^0 | H | \omega^0 \rangle$.

^fThe sum of the four contributions shown, to be compared with the final experimental result $(33.1 \pm 5.9 \pm 4.3) \times 10^{-4}$.

^gThe ρNN and ωNN coupling constants for the Bonn potential are evaluated at the meson poles.

^hThe ρNN and ωNN coupling constants derived from forward dispersion relation analyses of NN and πN scattering data are referred to the zero momentum transfer limit.

victim to the inherent experimental ambiguity of Eq. (15).

Both the present results and that of Ref. [11] agree very well with the full meson-exchange calculations. The success of the Bonn potential calculation, including ρ - ω mixing, at 183 MeV is particularly interesting. The magnitude of $\Delta A_{\rho\omega}$ depends on the ρNN and ωNN coupling constants assumed. The independent exchanges of ρ and ω play an important role in determining the short- and intermediate-range parts of the Bonn potential. The coupling constants obtained from fits of the Bonn potential to isospin-conserving NN scattering phase shifts are rather large: e.g., the values used in the CSB calculations of Ref. [15] are $g_\rho^2/4\pi=0.77$, $g_\omega^2/4\pi=23$. These can be compared to the smaller values ($g_\rho^2/4\pi=0.55$, $g_\omega^2/4\pi=8.1$) deduced from forward dispersion relation analyses of NN and πN scattering data [33], and to the considerably smaller ratio ($g_\omega^2/g_\rho^2=9$) predicted [34] on the basis of flavor SU(3) symmetry. Such comparisons suggest that the large Bonn potential coupling constants, especially for ωNN , may be viewed as effective values, simulating effects of heavier meson exchange, quark interchange, and/or relativistic effects omitted from the model [35]. If this were the case, however, one might expect Bonn potential calculations to overestimate $\Delta A_{\rho\omega}$, which has a sensitivity different from that of any conventional NN observable: it arises [16] from a spin-orbit potential specifically attributable to the exchange of *isospin-mixed vector mesons*. For example, it is difficult for NN interaction models based upon quark interchange to simulate $\Delta A_{\rho\omega}$, unless vector mesons are explicitly included in the sea-quark distribution of the nucleons [36]. The present ΔA results thus provide a significant internal consistency check for the Bonn potential. Figure 22 suggests that it passes this test at the present level of sensitivity.

On the other hand, the experimental error and the theoretical uncertainties associated with distortions are still sufficiently large that one can also obtain good agreement with our results by utilizing the smaller ρ and ω

coupling constants obtained from dispersion analyses. These have been used, for example, in conjunction with the Reid and Paris potentials to obtain the corresponding calculated $\langle \Delta A \rangle$ values in Table V. The Paris potential calculation, in particular, yields nearly the same total $\langle \Delta A \rangle$ as the Bonn calculation, despite the smaller coupling constants and consequently smaller value of $\langle \Delta A_{\rho\omega} \rangle$.

Another interesting question regarding the evaluation of the ρ - ω mixing contribution concerns the meson-mixing matrix element itself [37]. It is the *on-shell* value of this amplitude that is determined well by $e^+e^- \rightarrow \pi^+\pi^-$ measurements [3], whereas the vector mesons exchanged between interacting nucleons can be far off-shell. Goldman *et al.* [37] have recently cast doubt on the standard assumption that the mixing amplitude does not change significantly off-shell. In particular, within a simple quark model constructed to estimate the off-shell extrapolation, they find a *negligible* ρ - ω mixing contribution to CSB in $\bar{n}\bar{p}$ scattering. If this treatment holds up, then our measurement suggests that there are other, as yet neglected, significant contributions to the charge-symmetry-breaking nuclear force. Certainly, there are contributions of known origin that have been neglected in most calculations to date, most notably those associated with 2π or $\pi\gamma$ exchange. The former contributions have recently been demonstrated [38] quantitatively to be negligible at a bombarding energy of 183 MeV. A comparable treatment of $\pi\gamma$ -exchange contributions is an important goal for theoretical evaluations of CSB.

In principle, the curvature of $\Delta A(\theta)$, as measured by $(\langle \Delta A \rangle_{\text{outer}} - \langle \Delta A \rangle_{\text{inner}})$, can help to sort out the relative contributions from different exchange mechanisms. For example (see Fig. 2), $\Delta A_\pi(\theta)$ and $\Delta A_{\rho\omega}(\theta)$ have opposite curvature in the vicinity of θ_0 . In practice, however, the statistical uncertainty in the measured curvature is too large to distinguish among different predictions. Thus, we see in Fig. 23 that $\langle \Delta A \rangle_{\text{outer}} - \langle \Delta A \rangle_{\text{inner}}$ is reason-

ably reproduced by any of the three calculations (with Bonn, Paris, or Reid distorting potentials), despite appreciable differences among them in the relative importance of ΔA_π vs $\Delta A_{\rho\omega}$.

All of the calculations described above have been carried out at a single bombarding energy E_n . Since our experiment in fact averages the result over a relatively broad range of E_n , it is worth noting that, theoretically, a significant energy dependence of ΔA is expected near $E_n = 183$ MeV, even if the isospin-mixing parameters γ_J are independent of E_n . $\Delta A(\theta)$ results from the interference of a charge-symmetry-violating amplitude with a charge-symmetry-conserving amplitude ($b(\theta)$ in the notation of Ref. [39]). At $\theta_{c.m.} \simeq 90^\circ$, the imaginary part of the latter is known [19] to cross zero near 140 MeV. As a result, $\langle \Delta A \rangle_{82.2^\circ-116.1^\circ}$ is expected to increase in magnitude by a factor $\simeq 1.6$ between 170 and 193 MeV. Since the expected variation is nearly linear over this range, the comparison of our energy-averaged experimental result with calculations at the mean energy should be valid.

B. " $\Delta A(\theta)$ "

The experimental results for " $\Delta A(\theta)$ " shown in Fig. 19 were obtained by adjusting the constant c of Eq. (15) to minimize the variance of " $\Delta A(\theta)$ " (see Sec. VD). This procedure selects out a particular component of $\Delta A_{\text{true}}(\theta)$ [obtainable by adding a constant times $A(\theta)$] that is "uncorrelated" with $A(\theta)$, in the sense of Eq. (19). To make a meaningful comparison with theory, one must extract the analogous component of any predicted $\Delta A(\theta)$. This is done by adding a constant (c_{theory}) times $A(\theta)$ (calculated with Arndt [19] phase shifts) to $\Delta A_{\text{theory}}(\theta)$, and then adjusting c_{theory} to minimize the variance of the resulting " $\Delta A_{\text{theory}}(\theta)$ " over the same angle range as used for the measurement. The resulting modifications to the predicted curves are illustrated in Fig. 24 for calculations utilizing the Bonn (Ref. [15]) and Reid (Ref. [16]) NN potentials. The optimum value of c_{theory} is different for the two cases, but is very small for both, so that the modified predictions deviate only slightly from the true theoretical curves. It is clear from Fig. 24 that the differences between the two predictions in the mean value of ΔA near $\theta_{c.m.} \simeq 90^\circ$, and in the curvature in this vicinity, survive the variance minimization procedure.

The theoretical and experimental results for " $\Delta A(\theta)$ " are compared in Fig. 25. The Bonn potential calculation provides excellent agreement with the measurements, characterized by a total χ^2 value of 13.5 (based on statistical errors only) for 11 degrees of freedom. The agreement obtained with the Paris potential (not shown in Fig. 25) is comparable: $\chi^2 = 15.2$. That obtained with the Reid potential [16] is somewhat inferior quantitatively ($\chi^2 = 18.2$), but still provides a relatively successful qualitative explanation of the observed angular dependence.

If a prescription other than the variance minimization were applied to remove the $\delta\rho/\rho$ ambiguity of Eq. (14) from the data, and to modify the calculations analogously, both the measurements and predictions in Fig. 25 would change slightly [via a small "tilt" about $\Delta A(\theta_0)$].

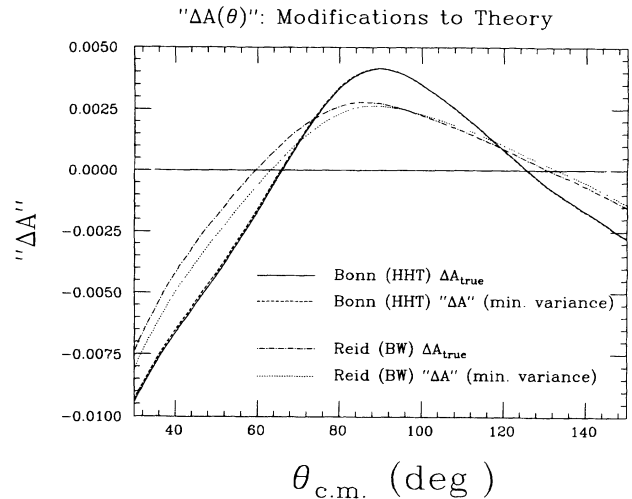


FIG. 24. Calculations illustrating the very small modifications of predicted $\Delta A(\theta)$ curves that are introduced by applying the "minimal variance" prescription for optimizing c_{theory} in Eq. (17). Calculations based on the Bonn [15] and Reid [16] NN distorting potentials are shown. In the former case, the modified curve is practically indistinguishable from the predicted $\Delta A_{\text{true}}(\theta)$.

However, the comparison between experiment and theory would be essentially unaffected. For example, one could obtain " $\Delta A(\theta)$ " by minimizing the rms value of " ΔA " over some angle range, rather than its variance; for the range 68° – 121° , application of this alternative prescription yields $\chi^2 = 13.2$ and 18.5, respectively, for the comparisons to Bonn and Reid potential calculations, indicating qualities of fit essentially identical to those seen in Fig. 25.

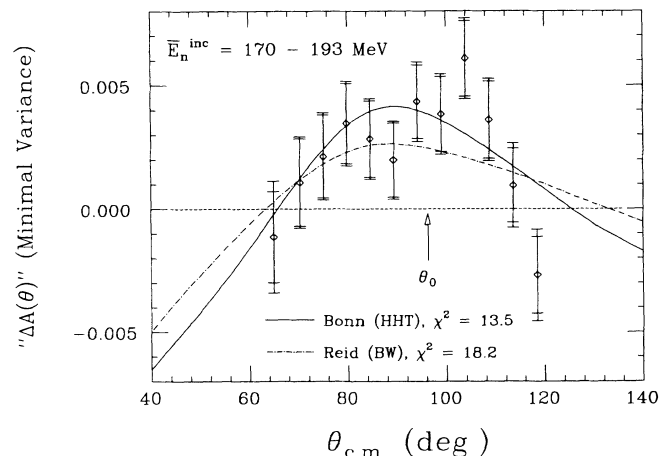


FIG. 25. Comparison of the measured " ΔA " angular distribution from Fig. 19 with calculations based on Refs. [15] and [16], which employ different distorting potentials and quite different ρNN and ωNN coupling constants. Both the experimental results and the theoretical curves have been subjected to the " ΔA " variance minimization procedure described in the text. The total χ^2 values specified for each curve include the effects of statistical errors only.

C. Other manifestations of CSB

Meson-exchange calculations consistent with those compared above to the present measurements have also had considerable recent success in accounting for other apparent manifestations of CSB nuclear forces [2]. In particular, the ρ^0 - ω^0 mixing contribution has been shown to be critical as well for reproducing the nn - pp scattering length difference [4], the ${}^3\text{H}$ - ${}^3\text{He}$ binding energy difference [4], and the binding energy (Nolen-Schiffer [6]) anomaly for heavier mirror-nucleus pairs [40]. In each of these cases the ρ - ω mixing contribution accounts for at least half of the inferred CSB difference (after subtraction of calculated electromagnetic contributions). The class III (Ref. [8]) *spin-orbit* CSB potential (of the form $[\tau_3(1)+\tau_3(2)](\sigma_1+\sigma_2)\cdot\mathbf{L}$), also due to the isospin mixing of vector mesons, provides a natural explanation for much of the A dependence observed in the Nolen-Schiffer anomaly [6,40]. The latter effect thus provides a sensitivity to ρ and ω exchange complementary to that of the present ΔA measurement, which samples instead class IV spin-orbit potentials [of the form of Eq. (1)].

The implication of these recent successes is significant: meson-exchange models appear capable of incorporating naturally and quantitatively the observed charge symmetry violations in the NN force. Although the sources of the violation (the n - p mass difference, ρ - ω mixing) are ultimately attributable to the properties and interactions of quarks, there is no need, at the present levels of experimental sensitivity, for the calculations to invoke *explicit* reference to quark degrees of freedom or to such related phenomena as “rescaling” of the nucleon size in the nuclear medium [2].

VIII. CONCLUSIONS

We have described in detail an experimental search for class IV charge-symmetry-breaking NN interactions in the scattering of 183-MeV polarized neutrons by polarized protons. We have measured the difference $\Delta A(\theta)$ between the analyzing powers associated with the neutron (A_n) and proton (A_p) spins. The average value of ΔA over the angle range $82.2^\circ \leq \theta_{\text{c.m.}} \leq 116.1^\circ$ (chosen because the average value of $A_n + A_p$ vanishes for this range) has been determined unambiguously and with high precision:

$$\langle \Delta A \rangle_{82.2^\circ-116.1^\circ} = (33.1 \pm 5.9 \pm 4.3) \times 10^{-4},$$

where the first quoted error is statistical and the second is systematic. This result is consistent with, but much more precise than, a recent measurement [11] for n - p scattering at 477 MeV. With the statistical and systematic errors added in quadrature, the new measurement differs by 3.4 standard deviations from the expected result for electromagnetic interactions alone. Since the electromagnetic contributions to ΔA are small and well understood, this result represents the most clearcut evidence to date of CSB strong nuclear interactions.

Both the mean value measured for ΔA and its angular dependence (which can be extracted only to within a constant times the average of A_n and A_p) are in excellent

agreement with calculations based on meson-exchange models of the CSB interactions. Within these calculations, the major short-range contributions arise from the effect of the n - p mass difference on one pion exchange and from the isospin mixing of exchanged ρ^0 and ω^0 mesons. These two contributions are of comparable magnitude, but differ significantly in their angular dependence; both must be included to explain the measurements fully. While each of these effects can be attributed at the quark level primarily to the u - d mass difference, the \bar{n} - \bar{p} scattering calculations do not themselves require *explicit* reference to quark degrees of freedom to account for the CSB NN interactions probed by the present experiment. This appears true as well for other observed manifestations of nuclear CSB: a consistent meson-exchange interpretation is now emerging [2] for the nn vs pp scattering length difference and mirror-nucleus binding energy differences, in addition to ΔA for \bar{n} - \bar{p} scattering.

The present results help to advance the investigation of charge symmetry in nuclear physics to a new stage: violations in the strong interaction have now been convincingly observed, and further efforts should concentrate on refining the quantitative interpretation. Progress here requires improvements to both theory and experiment. For the particular case of ΔA in n - p scattering, the meson-exchange theory can be improved, for example, by quantitative evaluation of additional contributions (e.g., from $\pi\gamma$ exchange) that have been neglected to date, and by further investigation of the off-shell extrapolation [37] of the ρ - ω mixing matrix element. Future experiments should aim at a more precise delineation of the energy and angle dependence of ΔA . It is of particular interest to enhance the sensitivity of experiments to the ρ - ω mixing contribution. Theoretical calculations suggest that a significant enhancement can be gained by appropriate choice of the bombarding energy: $\Delta A_{\rho\omega}$ in the vicinity of the zero-crossing angle of the average analyzing power (where the interpretation of measurements is least ambiguous) appears to be optimized [9] near 230 MeV, where it attains a magnitude roughly twice as large as at 183 MeV. It also appears feasible to increase the statistical precision of a ΔA measurement by a factor ~ 2 , e.g., with the use of a polarized proton target with higher polarization and a larger free/bound proton ratio than the one used in the present experiment.

The payoff for such improvements to theory and experiment would be more definitive tests of the quantitative role of ρ - ω mixing in charge symmetry violation, of the self-consistency of the large ρNN and ωNN coupling constants characteristic of the Bonn NN potential, and of the ability of QCD-inspired models (e.g., see Ref. [41]) of the NN interaction to account for ΔA *without* explicit inclusion of vector mesons in the sea-quark distribution [36]. These are important issues which the present results have only begun to explore.

ACKNOWLEDGMENTS

The authors are grateful to the members of the IUCF technical staff, particularly D. Friesel, D. DuPlantis, and

K. Solberg. Many others, including S. Bowyer, T. Bowyer, B. Hichwa, C. Glover, W. K. Pitts, S. Schultz, P. Schwandt, and G. Xu, made important contributions to the experiment. We also thank A. G. Williams, A. W.

Thomas, and J. Svenne for providing detailed theoretical results. This work was supported in part by the National Science Foundation under Grants No. PHY-8717764, No. PHY-8714406, and No. PHY-8611395.

-
- [1] P. Langacker and D. A. Sparrow, *Phys. Rev. C* **25**, 1194 (1982).
- [2] G. A. Miller, B. M. K. Nefkens, and I. Slaus, *Phys. Rep.* **194**, 1 (1990).
- [3] L. M. Barkov *et al.*, *Nucl. Phys.* **B256**, 365 (1985).
- [4] S. A. Coon and R. C. Barrett, *Phys. Rev. C* **36**, 2189 (1987).
- [5] T. E. O. Ericson and G. A. Miller, *Phys. Lett.* **132B**, 32 (1983).
- [6] J. A. Nolen, Jr. and J. P. Schiffer, *Annu. Rev. Nucl. Sci.* **19**, 471 (1969).
- [7] B. Gabioud *et al.*, *Nucl. Phys.* **A420**, 496 (1984); O. Schori *et al.*, *Phys. Rev. C* **35**, 2252 (1987); I. Slaus *et al.*, *Phys. Rev. Lett.* **48**, 993 (1982).
- [8] E. M. Henley and G. A. Miller, in *Mesons in Nuclei*, edited by M. Rho and D. H. Wilkinson (North-Holland, Amsterdam, 1979), Vol. 1, p. 405.
- [9] L. D. Knutson *et al.*, *Nucl. Phys.* **A508**, 185c (1990); W. W. Jacobs *et al.*, in *Proceedings of the Workshop on Spin and Symmetries*, edited by W. D. Ramsay and W. T. H. van Oers (TRIUMF Internal Report No. TRI-89-5, 1989, unpublished), p. 163.
- [10] L. D. Knutson *et al.*, *Phys. Rev. Lett.* **66**, 1410 (1991).
- [11] R. Abegg *et al.*, *Phys. Rev. Lett.* **56**, 2571 (1986); *Phys. Rev. D* **39**, 2464 (1989).
- [12] S. E. Vigdor *et al.*, Indiana University Cyclotron Facility internal report, 1992 (unpublished).
- [13] A. Gersten, *Phys. Rev. C* **18**, 2252 (1978); **24**, 2174 (1981).
- [14] A. G. Williams, A. W. Thomas, and G. A. Miller, *Phys. Rev. C* **36**, 1956 (1987).
- [15] B. Holzenkamp, K. Holinde, and A. W. Thomas, *Phys. Lett. B* **195**, 121 (1987). The calculations in this work are based on a momentum-space version of the Bonn one-boson-exchange potential (OBEP) taken from K. Holinde, *Phys. Rep.* **68**, 121 (1981). The use of coupling constants and form factor parameters from more recent versions of the Bonn potential, as, for example, in Ref. [17], does not appreciably alter the calculated isospin-mixing parameters γ_J , which are used as input to the phase-shift calculations displayed in the present paper. However, it is shown in Ref. [16] that if one uses instead the *coordinate-space* Bonn potential (OBEP), one significantly *overestimates* the CSB effects.
- [16] M. Beyer and A. G. Williams, *Phys. Rev. C* **38**, 779 (1988).
- [17] M. J. Iqbal and J. A. Niskanen, *Phys. Rev. C* **38**, 2259 (1988).
- [18] L. Ge and J. P. Svenne, *Phys. Rev. C* **33**, 417 (1986); **C 34**, 756(E) (1986).
- [19] Phase shift calculations have been performed using the program SAID, see R. A. Arndt, J. S. Hyslop III, and L. D. Roper, *Phys. Rev. D* **35**, 128 (1987). The phase-shift solution SM89 in SAID has been used, except where explicitly noted otherwise in the text.
- [20] W. H. Potter and H. J. Stapleton, *Phys. Rev. B* **5**, 1729 (1972).
- [21] A. Abragam, *Principles of Nuclear Magnetism* (Oxford University Press, New York, 1983).
- [22] D. V. Bugg and C. Wilkin, *Nucl. Phys.* **A467**, 575 (1987).
- [23] J. Sowinski and L. D. Knutson, *Phys. Rev. B* **37**, 9208 (1988).
- [24] It should be noted that there is no *additional* ambiguity in “ ΔA ” arising from flux normalization and dead-time errors. As is clear from Eq. (11), these affect only the overall normalization of $X(\theta)$ and are thus (just as for errors in ρ) incapable of *introducing* an angle dependence in X if there is not already one caused by CSB. In this sense, our estimated combined flux measurement and dead-time uncertainty ($\pm 1\%$ per spin state) serves mainly to increase slightly the effective range of values possible for the constant c in Eq. (15). In addition, it causes an extra (independent of $\delta P/P$) scale-factor uncertainty of $\pm 1\%$ in the extracted values of “ ΔA .”
- [25] J. Sowinski *et al.*, *Phys. Lett. B* **199**, 341 (1987); *Proceedings of the Seventh International Symposium on Polarization Phenomena in Nuclear Physics, Paris, 1990*, edited by A. Boudard and Y. Terrien (Les Editions de Physique, Les Ulis, 1990), p. 395.
- [26] Included in this systematic error is some allowance for the imperfect compensation of the localized surplus quasifree events afforded by an overall increase in the effective PPT thickness assumed. For example, this approach ignores a small variation of the mean (vertical) ${}^2\text{H}(p, n)$ production reaction angle, and hence of P_b , with y_{tgt} . For $\bar{n}\text{-}\bar{p}$ scattering over the angle range $25^\circ \leq \theta_p^{\text{ab}} \leq 40^\circ$, we have verified that this effect is indeed small by performing the loose-cut analysis also via the more correct procedure—namely, utilizing $t_D/t_{\text{PPT}} = 1.00$ with a greatly reduced beam spot cut. When the cut selects only the central $\sim 75\%$ of the target area, the target frame is completely eliminated and so, consequently, is the effect of the dummy-PPT misalignment.
- [27] For the purpose of fitting the asymmetries, we use the Gaussian angle rebinning procedure described in Sec. IV C 1 to correct for systematic angle errors introduced by multiple scattering. This gives slightly different results than 2-point rebinning.
- [28] Quantitatively quite similar variations of neutron-beam polarization with neutron energy from the ${}^2\text{H}(\bar{p}, \bar{n})$ production reaction have also been observed at lower bombarding energies, see M. A. Pickar *et al.*, *Phys. Rev. C* **42**, 20 (1990).
- [29] There is a very small difference (0.1×10^{-4}) in $\langle \Delta A \rangle_{\text{magic}}$ results obtained with Eq. (21) and by a similar energy-slice average, but with the weighting factors determined by the $\langle \Delta A_i \rangle$ measurement uncertainties (rather than Y_i) within each bin. The Y_i weighting is independent of the beam polarization variation with bombarding energy, and therefore is more likely to lead to a complete cancellation of possible instrumental errors in the *energy dependence* of $\langle \Delta A \rangle$, of the type discussed in Sec. V C.
- [30] A. S. Clough *et al.*, *Phys. Rev. C* **21**, 988 (1980); D. Cheng *et al.*, *Phys. Rev.* **163**, 1470 (1967).
- [31] D. Bandyopadhyay *et al.*, *Phys. Rev. C* **40**, 2684 (1989).
- [32] An analogous mixing of η^0 and π^0 mesons can contribute

to class III CSB potentials, but *single* pseudoscalar meson exchange does not yield the appropriate spin structure to cause isospin-mixing in the n - p system.

- [33] W. Grein, Nucl. Phys. **B131**, 255 (1977); W. Grein and P. Kroll, *ibid.* **A338**, 332 (1980). Part, but not all, of the apparent discrepancy between the coupling constants obtained from dispersion analyses and from Bonn potential fits arises because the former values refer to the zero momentum transfer limit, while the latter are relevant at the meson poles; see R. Machleidt, Adv. Nucl. Phys. **19**, 189 (1989).
- [34] G. E. Brown and A. D. Jackson, *The Nucleon-Nucleon Interaction* (North-Holland, Amsterdam, 1976).
- [35] F. Gross, J. W. Van Orden, and K. Holinde, Phys. Rev. C **41**, 1909 (1990).
- [36] A. W. Thomas, Prog. Part. Nucl. Phys. **20**, 21 (1988); and Proceedings of the Workshop on Spin and Symmetries, edited by W. D. Ramsay and W. T. H. van Oers (TRI-UMF internal report No. TRI-89-5, 1989, unpublished), p. 266.
- [37] T. Goldman, J. A. Henderson, and A. W. Thomas, Few-Body Systems (to be published).
- [38] J. A. Niskanen, Phys. Rev. C **45**, 2648 (1992).
- [39] J. Bystricky, F. Lehar, and P. Winternitz, J. Phys. (Paris) **45**, 207 (1984).
- [40] P. G. Blunden and M. J. Iqbal, Phys. Lett. B **198**, 14 (1987); T. Suzuki, H. Sagawa, and A. Arima, Nucl. Phys. **A536**, 141 (1992).
- [41] K. Brauer, E. M. Henley, and G. A. Miller, Phys. Rev. C **34**, 1779 (1986); M. R. Encinosa, Jr., Ph.D. Thesis, Florida State University, 1987, unpublished.